University of Pardubice
Jan Perner Transport Faculty
Transport Means and Diagnostics Department

ESTIMATION OF STATES AND PARAMETERS FROM DYNAMIC RESPONSE OF WHEELSET

Altan Onat M.Sc.

Dissertation Thesis

2017

Programme of study:
P3710 - Technique and Technology in Transport and Communications

Branch of study:
3706V005 - Transport Means and Infrastructure

Supervisor: doc. Ing. Michael Lata, Ph.D.

Specialist supervisor: Ing. Petr Voltr, Ph.D.

Dissertation came into being at department:

Department of Transport Means and Diagnostics

I hereby confirm that:

I have written this dissertation thesis independently. All the reference, literature and information used in this work are quoted in the list of references.

I hereby acknowledge that all the rights and duties resulting from Act No. 121/2000 Coll., the Copyright Act, apply to my written work, especially that the University of Pardubice has the right to make a license agreement of use of this written work as a school work pursuant to § 60 section 1 of the Copyright act. On the condition that the written work shall be used by me or a license shall be provided to another subject for the use hereof, the University of Pardubice shall have the right to require from me a relevant contribution to reimburse the costs incurred for the making of such work including all relevant costs and total overal expenditure and expenses incurred.

I agree with making the work accessible in the University Library.
Dated in Pardubice on January 12, 2017.

Altan Onat

Acknowledgements *Foremost, I would like to express my sincere gratitude to my supervisor doc. Ing. Michael Lata, PhD. for letting me carry out research in this specific area, for providing me motivation, and for all kinds of help.*

Besides my supervisor, I would like to thank my specialist supervisor Ing. Petr Voltr, PhD. for his insightful comments, patience to answer my endless questions and quick responses to my e-mails.

I am very much obliged to the Laboratory of Computational Mechanics, Bryansk State Technical University, Russia for providing a 6 month academic license of Universal Mechanism software and UM Loco module for PhD students.

I would like to thank prof. Ing. Jaroslav Novák, CSc. for his help and effort during electrical measurements from asynchronous motor of the tram wheel test stand.

I would also like to thank my family for the support they provided me through my entire life and in particular.

I owe also thanks to my friends in Pardubice for their help and friendship during these years.

I must acknowledge my girlfriend Zuzana Holubová for her support and assistance.

Altan Onat

Annotation

In this dissertation, the use of model based filtering techniques for wheelsets of railway vehicles is presented. Especially, this dissertation provides the application of a parameter estimation scheme by using dynamic response of a conventional wheelset, a vehicle and a tram wheel on a test stand with a novel methodology. In the context, firstly, an introduction is reported. Afterwards, a review of the related literature in the thematic area is demonstrated along with the current state of the doctoral dissertation. Third section includes the objectives of the dissertation where the aim of the dissertation clearly emphasized. The following section describes the methods and models in details which are used in this work. Throughout the succeeding sections contributions of the dissertation for related literature, a conclusion for dissertation, bibliography, and the publications of the PhD student are given, respectively.

Keywords

wheel-rail contact, wheelset dynamics, model based filtering, railway vehicle dynamics, Kalman filter, unscented Kalman filter

Název Práce

Odhad Stavů a Parametrů z Dynamické Odezvy Dvojkolí

Souhrn

V této disertační práci je představeno využití metod filtrace založených na modelu pro dvojkolí kolejových vozidel. Tato práce zejména prezentuje aplikaci inovativní metody odhadu paramterů na základě dynamické odezvy obvyklého dvojkolí, celého vozidla a tramvajového kola na zkušebním stavu. V této souvislosti je nejprve dán úvod. Navazuje přehled literatury k tomuto tématu. Třetí kapitola objasňuje účel práce a jasně vytýká cíle disertačný práce. Následující kapitola podrobně popisuje metody a modely, které jsou použity v této práci. Další kapitoly postupně představují přínosy provedených rozborů, shrnutí disertační práce, seznam literatury a seznam publikací doktoranda.

Kličová Slova

kontakt kolo-kolejnice, dynamika dvojkolí, filtrování založené na modelu, dynamika kolejových vozidel, Kálmánův filtr, unscentovaný Kálmánův filtr

Table of Contents

List of Figures

List of Tables

List of Abbrevations and Symbols

List of Abbreviations

min	Minimum
BEM	Boundary Element Methods
DAQ	Data Acquisition
DFJP	Jan Perner Transport Faculty
DOF	Degrees of Freedom
e.g.	in Latin *exempli gratia* (in English For Example)
EKF	Extended Kalman Filter
EN	European Standards
ERRI	European Rail Research Institute
FEM	Finite Element Methods
i.e.	in Latin *id est* (in English In Other Words)
MBS	Multi Body Simulation
ORE	Office for Research and Experiments
PMSM	Permanent Magnet Synchronous Motor
RMSE	Root Mean Squared Error
TOR	Top of Rail
UIC	International Union of Railways
UKF	Unscented Kalman Filter
UM	Universal Mechanism MBS Software
UPCE	University of Pardubice
UT	Unscented Transformation
V/f	Volts per Hertz
VÚKV	Výzkumný Ústav Kolejových Vozidel–Rail Vehicle Research Institute
w.r.t.	With Respect To

List of Symbols

δ	$[m]$	Indentation of the Bodies in the Theory of Hertz
δ_0	$[m]$	Virtual Interpenetration value in Virtual Penetration Method

δ_p	$[rad]$	Contact Angle $p = L(left), R(right)$
$\mathbf{E}_e$	$[-]$	Elliptical Integral of the Second Kind
$\mathbf{K}_e$	$[-]$	Elliptical Integral of the First Kind
$\mathbf{V}_{\mathbf{par,uns}}$	$[m/s]$	Velocity of a Particle in Unstressted State
∇	$[-]$	Gradient Operator
ξ_s	$[1/m]$	Spin Creepage
ξ_x	$[-]$	Relative Longitudinal Creepage
ξ_y	$[-]$	Relative Lateral Creepage
a	$[m]$	Contact Patch Semi-Axis Length
b	$[m]$	Contact Patch Semi-Axis Width
e	$[-]$	Eccentricity of the Contact Ellipse
E_{12}	$[Pa]$	Combined Young's Modulus for Bodies
p	$[Pa]$	Pressure Distribution in the Contact Area
p_x	$[Pa]$	Traction in the longitudinal direction in the Contact
p_y	$[Pa]$	Traction in the lateral direction in the Contact
p_{z_0}	$[Pa]$	Maximum Normal Pressure in the Contact Area
p_z	$[Pa]$	Normal Stress in the Contact Area
V_r	$[m/s]$	Translational Velocity of Roller
V_{wr}	$[m/s]$	Velocity of Wheel on Rail (or Roller)
V_w	$[m/s]$	Translational Velocity of the Wheelset (or tram wheel)
α	$[-]$	Constant Determining Distribution of Sigma Points around Mean
$\bar{\kappa}$	$[1/m]$	New Curvatures due to Quasi–Elastic Search
$\bar{a}$	$[m]$	x Coordinate of the Leading Edge
$\bar{s}$	$[m]$	New Contact Location due to Quasi–Elastic Search
β	$[-]$	Prior Knowledge about the distribution of the random variable $\mathbf{x}$
β	$[rad]$	Angular Perturbation from Nominal Angular Velocity of Wheelset
$\boldsymbol{\chi}$	$[-]$	Vector of Sigma Points in Unscented Transformation
$\boldsymbol{\Upsilon}$	$[-]$	Vector of Propagated Sigma Points in Unscented Transformation
Δ_i	$[m]$	Lateral Displacement of Contact Point $i = L, R$
δ_p	$[-]$	A Ratio Used in Polach's Creep Force Model

ϵ	$[-]$	Gradient of Tangential Stress in Adhesion Area
ϵ_{reg}	$[-]$	Regularization Parameter in Quasi–Elastic Search
ϵ_{sat}	$[-]$	Creep Force Reduction Coefficient
ϵ_{sp}	$[-]$	The Gradient of Tangential Stress in case of Spin
ϵ_s	$[-]$	Tolerance in Semi–Analytical Method
γ_f	$[-]$	A Constant Used in Unscented Transformation $\gamma_f = \sqrt{L+\lambda}$
κ	$[-]$	Secondary Scaling Parameter in Unscented Transformation
κ_p	$[1/m]$	Curvature of the Respective Profile
λ	$[-]$	Scaling Parameters in Unscented Transformation
λ_h	$[rad]$	Angle Related with the Contact Shape in Hertz Theory
$\mathbf{V_{par}}$	$[m/s]$	Velocity of a Particle in Deformed State
$\bar{\mathbf{x}}$	$[-]$	Mean of the Random Variable x
$\dot{\mathbf{u}}$	$[-]$	Velocity Vector of Vertical Track Irregularities
$\mathbf{B}$	$[-]$	Damping Matrix of Complete Vehicle Model
$\mathbf{E}[arg]$	$[-]$	Mean of the Random Variable arg
$\mathbf{F}_k$	$[-]$	System (or State) Matrix at Time k
$\mathbf{F}_s$	$[N]$	Total Suspension Force Acting on Wheelset
$\mathbf{G}_k$	$[-]$	Input Matrix at Time k
$\mathbf{H}$	$[kgm^2.\frac{rad}{s}]$	Angular Momentum of the Wheelset
$\mathbf{H}_k$	$[-]$	Output Matrix at Time k
$\mathbf{I}$	$[-]$	Identity Matrix
$\mathbf{i}_{p_c}$	$[-]$	Longitudinal Unit Vector on the Contact Axes $p = L, R$
$\mathbf{i}_p$	$[-]$	Longitudinal Unit Vector $p = eq, int, w$
$\mathbf{j}_{p_c}$	$[-]$	Lateral Unit Vector on the Contact Axes $p = L, R$
$\mathbf{j}_p$	$[-]$	Lateral Unit Vector $p = eq, int, w$
$\mathbf{K}$	$[-]$	Stiffness Matrix of Complete Vehicle Model
$\mathbf{K}_k$	$[-]$	Kalman Gain Matrix
$\mathbf{k}_{p_c}$	$[-]$	Vertical Unit Vector on the Contact Axes $p = L, R$
$\mathbf{k}_p$	$[-]$	Vertical Unit Vector $p = eq, int, w$
$\mathbf{M}$	$[-]$	Mass Matrix of Complete Vehicle Model

$\mathbf{M}_s$	$[Nm]$	Total Suspension Moment Acting on Wheelset
$\mathbf{p}*$	$[Pa]$	Transformed Variable for Tangential Stress
$\mathbf{P}_k^+$	$[-]$	Covariance of the Estimation Error x_k^+
$\mathbf{P}_k^-$	$[-]$	Covariance of the Estimation Error x_k^-
$\mathbf{q}_k$	$[-]$	Additive Gaussian White Noise for the System States at Time k
$\mathbf{r}$	$[m]$	Position Vector of the Wheelset
$\mathbf{R}_{i_j}$	$[m]$	Position Vector of the Contact Point $i = L, R$ $j = x, y, z$
$\mathbf{r}_k$	$[-]$	Additive Gaussian White Noise for the Measurements at Time k
$\mathbf{T}_b$	$[-]$	Damping Matrix for Velocity of Vertical Track Irregularity
$\mathbf{T}_k$	$[-]$	Stiffness Matrix for Vertical Track Irregularity
$\mathbf{u}$	$[-]$	Vector of Vertical Track Irregularities
$\mathbf{u}_k$	$[-]$	Input to the System at Time k
$\mathbf{v_s}$	$[m/s]$	Slip Vector of the Bodies
$\mathbf{x}$	$[-]$	State Vector
$\mathbf{x}_k$	$[-]$	State of the System at Discrete Time k
$\mathbf{x}_k^+$	$[-]$	Posteriori State Estimate
$\mathbf{x}_k^-$	$[-]$	Priori State Estimate
$\mathbf{y}_k$	$[-]$	Measurements of the System at Discrete Time k
μ	$[-]$	Friction Coefficient
μ_0	$[-]$	Maximum Friction Coefficient
μ_∞	$[-]$	Limit Friction Coefficient at Infinite Slip
Ω	$[rad/s]$	Nominal Angular Velocity of the Wheelset
ω_r	$[rad/s]$	Angular Velocity of the Roller
ω_{syn}	$[rad/s]$	Synchronous Speed of the Asynchronous Motor
ω_{w_p}	$[rad/s]$	Angular Velocity of the Wheelset $p = eq, int, w$
ϕ	$[rad]$	Roll Angle of the Wheelset
ϕ_0	$[rad]$	Initial Roll Angle of the Wheelset
ψ	$[rad]$	Yaw Displacement of the Wheelset
ψ_h	$[rad]$	Angular Difference Between Coordinate Systems (Hertz Theory)
σ_z	$[Pa]$	Normal Pressure in the Contact

A	$[-]$	Ratio of Limit Friction Coefficient to Maximum Friction Coefficient
a_1	$[m]$	Longitudinal Semi–Spacing of Secondary Suspension
a_2	$[m]$	Longitudinal Semi–Spacing of Primary Suspension
B	$[s/m]$	Coefficient of Exponential Friction Decrease
b_1	$[Ns/m]$	Damping Coefficient of Secondary Vertical Suspension
b_2	$[Ns/m]$	Damping Coefficient of Primary Vertical Suspension
b_x	$[Ns/m]$	Lateral primary damping coefficient
b_y	$[Ns/m]$	Lateral primary damping coefficient
C	$[N/m^3]$	Tangential Contact Stiffness
c_1	$[m]$	Lateral Semi–Spacing of Secondary Suspension
c_2	$[m]$	Lateral Semi–Spacing of Primary Suspension
c_{ij}	$[-]$	Kalker coefficients
c_{jj}	$[-]$	Combined Kalker Coefficient
C_s	$[N/m^3]$	Tangential Contact Stiffness for Spin
$d(y,z)$	$[m]$	Distance Between Profiles on the z–axis as a function y
$exp(arg)$	$[-]$	Exponential of the argument e^{arg}
f	$[-]$	Coefficient of Adhesion
$F_{i_{NL}}$	$[N]$	Creep Force Components in Heuristic Model $i = x, y$
F_i	$[N]$	Creep Force at the Contact Point $i = L, R$
F_n	$[N]$	Total Normal Load
F_{Res}	$[N]$	Resultant Creep Force
F_{y_C}	$[N]$	Resulting Lateral Creep Force in case of Spin
F_{y_S}	$[N]$	Increase in Lateral Creep Force due to Spin
G	$[Pa]$	Modulus of Rigidity
I_{w_p}	$[kgm^2]$	Moments of Inertia of the Wheelset $p = x, y, z$
$J_{r_{total}}$	$[kgm^2]$	Total Moment of Inertia of Roller of the Test Stand
$J_{w_{total}}$	$[kgm^2]$	Total Moment of Inertia of Wheel of the Test Stand
J_{x1}	$[kgm^2]$	Moment of Inertia of Coach Around x–axis
J_{x2}	$[kgm^2]$	Moment of Inertia of Bogie Around x–axis
J_{y1}	$[kgm^2]$	Moment of Inertia of Coach Around y–axis

k_1	$[N/m]$	Stiffness of Secondary Vertical Spring
k_2	$[N/m]$	Stiffness of Primary Vertical Spring
k_A	$[-]$	Reduction Factor in the Adhesion Area
K_M	$[-]$	An Auxiliary Variable Used in Polach's Creep Force Model
k_S	$[-]$	Reduction Factor in the Slip Area
k_x	$[N/m]$	Longitudinal primary spring stiffness
k_y	$[N/m]$	Lateral primary spring stiffness
L	$[-]$	Dimension of the Random Variables in Unscented Transformation
L_ϕ	$[m^3/N]$	Flexibility Parameter for Spin
L_x	$[m^3/N]$	Flexibility Parameter in x Direction
L_y	$[m^3/N]$	Flexibility Parameter in y Direction
m_1	$[kg]$	Mass of the Coach
m_2	$[kg]$	Mass of the Bogie
M_i	$[Nm]$	Creep Moment at the Contact Point $i = L, R$
m_m	$[kg]$	Laterally Constrained Suspended Mass of Superstructure
m_w	$[kg]$	Mass of the Wheelset
$M_{z_{NL}}$	$[Nm]$	Creep Moment According to the Heuristic Model $i = x, y$
N_i	$[N]$	Normal Force at the Contact Point $i = L, R$
p_0	$[Pa]$	Maximum Tangential Stress at Contact
r_0	$[m]$	Nominal Rolling Radius of the Wheelset
$R_2^{'}$	$[\Omega]$	Reflected Resistance of the Rotor Side
r_i	$[m]$	Rolling Radius $i = L, R$
r_p	$[m]$	Rolling Radius of the Respective Wheel $p = L, R$
r_{r_x}	$[m]$	Longitudinal Rolling Radius of the Roller on Test Stand
R_{Th}	$[\Omega]$	Per Phase Thevenin Resistance on the Stator Side
r_{w_x}	$[m]$	Longitudinal Rolling Radius of the Wheel on Test Stand
r_w	$[m]$	Rolling Radius of the Wheel
s	$[-]$	Total Relative Slip
s	$[m]$	Half of the Tape Line Distance
s_C	$[-]$	Resulting Relative Slip in case of Spin

S_k	$[-]$	Square Root of the Covariance Matrix P_k at Discrete Time k
s_m	$[-]$	Slip of the Asynchronous Motor
s_x	$[-]$	Relative Slip in x–axis
s_{y_C}	$[-]$	Corrected Lateral Relative Slip in case of Spin
s_y	$[-]$	Relative Slip in y–axis
T	$[N]$	Tangential Force Occured between Wheel and Roller
T_A	$[Nm]$	Torque Exerted on Roller by Asynchronous Motor
T_P	$[Nm]$	Torque Exerted on Wheel by PMSM
$Tr(X)$	$[-]$	Trace of the Square Matrix X
V	$[m/s]$	Longitudinal Velocity of the Vehicle
V_{Th}	$[V]$	Per Phase Thevenin Voltage on the Stator Side
V_w	$[m/s]$	Longitudinal Velocity of the Wheelset
w	$[m/s]$	Slip Velocity
W_i	$[-]$	Weights used in Unscented Transformation
W_w	$[N]$	Weight of the Wheelset
$X \mid Y$	$[-]$	The Probability of Event X, Given That Y Has Already Occurred
x_0^+	$[-]$	Initial State Estimate
X_2'	$[\Omega]$	Reflected Reactance of the Rotor Side
x_{eq}	$[m]$	Longitudinal Axis of Equilibrium Coordinate System
x_{int}	$[m]$	Longitudinal Axis of Intermediate Coordinate System
x_{pc}	$[m]$	Longitudinal Axis of Contact Coordinate System $p = L, R$
X_{Th}	$[\Omega]$	Per Phase Thevenin Reactance on the Stator Side
x_w	$[m]$	Longitudinal Axis of Wheelset Coordinate System
$y*$	$[m]$	Transformed Variable for y–axis
y_{eq}	$[m]$	Lateral Axis of Equilibrium Coordinate System
y_{int}	$[m]$	Lateral Axis of Intermediate Coordinate System
y_{irr_i}	$[m]$	Lateral Irregularity for Right and Left Rails $i = R, L$
y_{irr}	$[m]$	Lateral Aligment Irregularity
y_{pc}	$[m]$	Lateral Axis of Contact Coordinate System $p = L, R$
y_p	$[m]$	Lateral Axis of the Respective Profile in Cartesian Coordinates

y_w	$[m]$	Lateral Axis of Wheelset Coordinate System
z_{eq}	$[m]$	Vertical Axis of Equilibrium Coordinate System
z_{int}	$[m]$	Vertical Axis of Intermediate Coordinate System
z_{pc}	$[m]$	Vertical Axis of Contact Coordinate System $p = L, R$
z_p	$[m]$	Verticle Axis of the Respective Profile in Cartesian Coordinates
z_w	$[m]$	Vertical Axis of Wheelset Coordinate System

Introduction

Since 19^{th} century, the theoretical and practical research in railway vehicle dynamics are keys to have faster and safer vehicles. Recently, there has been an increasing interest in designing intelligent vehicles so that they can take necessary actions according to the environmental changes around them and they can inform decision makers about these changes. It should be noted that vehicle dynamics is an indispensable tool to design such intelligent vehicles. Besides, in order to have faster and safer vehicles, especially understanding of the dynamic behaviour of a wheelset is *conditio sine qua non*.

In order to investigate the motion of a wheelset, which is the fundamental part of a railway vehicle, firstly geometries of the considered wheel-rail profiles must be investigated and/or decided. As a consequence of understanding the geometrical interaction (i.e. determination of contact points), finding an approximate contact patch becomes easier so that normal force and pressure distribution can be found. Solution to the normal problem is a must to obtain adhesive forces occurred in the contact patch. A creep force model is required to solve tangential problem (i.e. calculation of adhesive forces). After obtaining creep forces, specific dynamic behaviour of the wheelset and vehicle can be predetermined.

The dynamic behaviour of the wheelset can be used to assess some safety critical criteria such as hunting motion, safety against derailment etc. Additionally, this dynamic behaviour contains information about its environment and other related parts (e.g. suspension elements) of the vehicle. It is a fact that change in environmental conditions (e.g. friction condition changes) or a change in some parts of vehicle (e.g. properties of suspension elements) directly influences motion of the wheelset and vehicle. The very essence of this dissertation is to search the possibilities of extracting such information from the dynamic response of a wheelset.

Firstly, maximum friction coefficient between wheel–rail interface is identified by using the lateral dynamic response of a wheelset due to track alignment. It is shown that by using the lateral dynamic response of a wheelset and a novel methodology, friction condition between wheel–rail can be estimated without using post–processing methods. By using the same approach and dynamic model, possibility of estimating

primary suspension parameters is also investigated especially for intelligent maintenance purpose.

Conducting on–track experiments for railway vehicles is difficult, expensive and time consuming. In order to overcome this issue, roller-rig test stands are used for research to enhance the performance of vehicles. Adhesion, wheel–rail contact and traction are such research areas that better observation of these phenomena leads to safer and cheaper transport. In this dissertation, secondly, a model based parameter estimation scheme is presented for a tram wheel test stand which is used for previously mentioned research purposes. Model is validated by means of comparison with measurements taken from the test stand. Then, the focus is given to estimate rolling radius of the wheel just by using angular velocity measurements and this novel estimation methodology can be used for wheel profile detection of railway vehicles.

In order to obtain such information from dynamic response of a wheelset, tram wheel, bogie and/or vehicle, model based filters are widely used. Family of Kalman filters are examples of such kind of model based filters and this dissertation focuses on the consideration of Kalman filters for estimation of states (i.e. position and velocity components of the wheelset, bogie and/or vehicle) and parameters (i.e. friction coefficient, primary spring stifnesses etc.).

1 *Analysis of the Current Situation in the Area of Dissertation*

In order to analyse the current situation in the related area, key components required during the investigation of dynamics of railway vehicle systems are given. After the review of dynamic analysis of railway vehicle systems, use of the model based filters in railway vehicle systems is presented. Furthermore, a review of the use of roller–rigs, which are considered for research purposes in railway vehicle dynamic analysis, is provided.

1.1 Wheel-Rail Contact Geometry and Contact Search

First step of analysing the wheel–rail contact is the investigation of the geometries of the used wheel–rail pair. There exist many types of wheel–rail profiles across the globe. In this dissertation, S1002–UIC60E1 wheel–rail pair, which is one of the widely used wheel–rail pairs across the Europe, is considered. The details of the wheel–rail profiles can be found in related standards by (EN, 2011; UIC, 2004).

Determination of the normal load and the contact locus with an elastic material assumption is dependent not only on the independent states of the wheelset (i.e. lateral shift, yaw angle, longitudinal shift) but also on the dependent states (i.e. all 6 degrees of freedom) of the wheelset as indicated by (Bosso et al., 2013). Therefore, the contact locus search with the elastic material assumption requires high computational cost, whereas the rigid contact search method is fairly simple. Nevertheless, rigid contact search method has two important drawbacks, (Bosso et al., 2013). First drawback is that it does not allow to consider the wheel uplift, and the second one is that this method does not allow to examine double or more contact points which makes this method impractical to apply for worn profiles. Method, which is called quasi–elastic contact search, eliminates the drawbacks of the elastic and rigid contact search methods. Quasi-elastic method is presented by (Arnold and Netter, 1997; Netter et al., 1998; Schupp et al., 2004). The quasi–elastic contact search method assumes the exponential deformation of wheel–rail surfaces. Unlike the rigid contact search method, the distance between profiles no longer represented by vertical distances in the quasi-elastic contact search method. Instead, it is represented by the averaged distance function in the area of possible contact which is obtained by the rigid method. Both rigid and quasi–elastic contact search methods are

considered in this dissertation.

It is emphasized in the previous paragraph that the contact locus depends also on the dependent states. The roll angle of the wheelset is one of the dependent states and it is directly related with the lateral shift and the yaw angle of the wheelset. Roll angle of the wheelset affects the contact locus and it must be found with respect to (abbreviated as w.r.t.) the independent states. The yaw angle does not have much influence on the contact locus, unless it causes a flange contact. Thus, the roll angle can be calculated just w.r.t. the lateral shift of the wheelset. In order to find the roll angle w.r.t. the lateral shift, there are two solutions reported in the literature, namely analytical and semi-analytical methods. These two methods are explained by (Shevtsov, 2008). The analytical method requires the solution of a set of nonlinear equations to find the contact points, the roll angle and the lift of wheelset in vertical direction. The roll angle can be obtained easily w.r.t. the lateral shift of the wheelset by using the semi–analytical method. Due to the small effect of the yaw angle on the roll angle, problem becomes planar and the roll angle is represented as a function of the lateral shift by using the semi-analytical method. Details and explanations of the semi–analytical method are given by (Li, 2002), and this method is preferred in this doctoral work because of its simplicity and low computational cost.

1.2 Wheel-Rail Normal Problem

(Gerlici et al., 2005) emphasize that the size and shape of the contact area influence directly the motion of the vehicle. In the literature, there exist several methods to find the contact patch size and shape. One of the widely used methods is given in the seminal work by (Hertz, 1882). The theory of Hertz is still used in up–to–date multibody simulation (i.e. MBS) packages. The theory of Hertz includes some assumptions which are elastic half spaces, nonconformal elliptical contact (valid if the dimensions of the contact area is small compared to the curvatures of surfaces) and frictionless surfaces. The theory of Hertz provides the most accurate results in case of surfaces with continous curvatures (e.g. conical and cylindrical surfaces). In order to get more accurate results for the curvilinear wheel–rail profiles (i.e. where sudden curvature changes occur in surfaces), the

semi–Hertzian contact must be considered, (Ayasse and Chollet, 2005). A review of the analytical methods for the solution of the normal problem (considering the non-elliptical contact models) is given in the study by (Piotrowski and Chollet, 2005), which also includes the details of the work by (Ayasse and Chollet, 2005). In the related literature, there are not only analytical methods but also boundary element methods (i.e. BEM) and finite element methods (i.e. FEM) to find solution to the normal problem, (Knothe et al., 2001). BEM are based on the discretization of the contact area and the solution of the integral equation w.r.t. this discretization, whereas FEM are based on dividing the whole problem into smaller parts, which are called finite elements, and then solving the problem by using the variational method by minimising an associated error function. The most accurate and widely used BEM are derived by (Kalker, 1990). Solutions proposed by Kalker and FEM have a drawback compared with the analytical methods which is computational complexity. Mostly, the theory of Hertz, which is also used widely within many MBS packages, is considered hereby. In order to use the theory of Hertz, solution of the first and second type of elliptical integrals are required. Coefficients, namely m and n, must be found w.r.t. geometrical parameters of the contacting bodies in order to find the contact patch and size. In the original work by (Hertz, 1882), these coefficients are given as a tabular data w.r.t. geometrical coefficients. In the literature, there exist studies which present approximation functions for this tabular data. Such examples of approximation functions can be found as a closed form (Shabana et al., 2007) and as a curve interpolation (Sebeşan and Zakaria, 2014; Srivastava et al., 2013). In this dissertation, the method to find the Hertzian contact expressed by (Michálek, 2008) is used. It is based on the numerical solution of the elliptical integrals in the theory of Hertz. This method provides more accurate results while maintaining the computational complexity depending on how many terms are selected for the series expansion for the elliptical integrals. Details of the wheel–rail contact geometry and solution to the normal problem by using the theory of Hertz, which are considered hereby, are presented by (Onat et al., 2014). In some sections of the dissertation, the method proposed by (Piotrowski and Kik, 2008) is considered to rescale the Hertzian contact patch. This method is based on the approximation of the contact area by using the virtual interpenetration region. However, it is indicated that the

method does not provide the correct shape unless the contact area is circular. Therefore, rescaling the contact area by referring to the theory of Hertz is introduced, (Piotrowski and Kik, 2008).

1.3 Wheel-Rail Tangential Problem

One of the crucial steps in the determination of the dynamic response of a railway vehicle system is the calculation of the tangential forces between wheel–rail. A very first investigation on the motion of the wheelset is that the wheels do not have *pure rolling* motion. Instead, experiments show that the motion of the wheels consists of *rolling* and *sliding* motion. A notable review, which presents the history of wheel-rail contact mechanics, has become available by (Knothe, 2008). This study includes all the aspects of wheel–rail contact mechanics including the theories developed for the solution of the normal and tangential problem, and the slice of lives of the respective contributors as well.

As stated by (Knothe, 2008), first solution to the tangential problem in wheel–rail contact is provided by Carter. Carter considers the wheel as a cylinder (i.e. disc) rolling over a flat rail. The observation of the Carter is that the motion of the wheels do not switch from full adhesion to full sliding and rather sliding increases up to a certain extent as the traction is gradually increased. This phenomenon is known as creepage and tangential forces are directly related with the amount of the creepage. The first three dimensional solution is given by (Johnson, 1958). Johnson focuses on an elastic sphere rolling on an elastic plane. Johnson investigates the straight rolling motion and spin of elastic sphere. Study by (Johnson, 1958) is limited with the circular contact area and (Vermeulen and Johnson, 1964) extend it to the elliptical area of the contact in two dimensions and they propose a saturation law for tangential forces. The law proposed by (Vermeulen and Johnson, 1964) does not consist of the effect of the spin. The knowledge and experience of Johnson in the area of contact mechanics can be found in the book written by himself, (Johnson, 1985).

Joost Kalker is one of the most important contributors in the area of wheel–rail contact mechanics. His theories and methods are the most accurate analytical and BEM

based solutions to the wheel–rail normal and tangential problem, even nowadays. Main part of Kalker's research is started with his famous PhD thesis, (Kalker, 1967). Kalker assumes the elastic half spaces, elliptical contact area and steady rolling in his thesis. It is stated that the computation times for the exact theory are excessive. (Kalker, 1973) proposes a simplified version of the exact theory which can be computed 100 times faster than the exact theory. This theory is known as the Kalker's linear theory and it provides the longitudinal, lateral forces and spin moment linearly w.r.t. the creepage. Afterwards, (Kalker, 1982) proposes an algorithm that provides faster results than the exact theory. However, it is slower than the linear theory, but its results are more accurate than the linear theory. (Kalker, 1982) models the connection between traction and elastic displacement by using tangential flexibility. The algorithm is based on slicing the contact area and calculating tangential forces accordingly. (Shen et al., 1983) report a nonlinear theory based on Kalker's linear theory. Unlike the study by (Vermeulen and Johnson, 1964), (Shen et al., 1983) include also the effect of spin by rearranging the creep force model including a normalizing factor, which is an indicator of the spin. One of the newest analytical formulations for the solution of the tangential problem is proposed by (Polach, 2005). The decreasing part of the creep force–creep curve can possibly be explained by the decreasing friction coefficient due to increasing temperature in the contact area for large creep, (Polach, 2005). Increase in the temperature of the contact area depends on the slip velocity. This idea firstly presented by (Freibauer, 1983). Study by (Polach, 2005) is the extension of the work by (Freibauer, 1983). In this dissertation, the methods given by (Polach, 2005) and (Kalker, 1982) is preferred for the solution of the tangential problem because of their sufficiently accurate results and simplicity.

1.4 Dynamics of Wheelset and Railway Vehicles

Dynamic analysis of a wheelset and railway vehicles is a mature and still a challenging area. There are still ongoing research and projects across the globe to propose dynamic models which provide better understanding of real world situations. In the first part of this dissertation, lateral dynamics of a wheelset (i.e. hunting motion) is considered extensively. Therefore, the literature, which includes especially the wheelset

lateral dynamics, is given hereby.

Several textbooks exist in the literature which give insight to the dynamics and simulation of railway vehicles. The textbook by (Garg and Dukkipati, 1984) is one of the oldest in the literature, especially for first few chapters in this textbook, steps for obtaining a wheelset dynamic model are provided. (Garg and Dukkipati, 1984) assume the wheelset as a rigid body and show that other degrees of freedom of the wheelset do not have much effect on the lateral and yaw dynamics of the wheelset. Thus, a 2 degrees of freedom (i.e. DOF) lateral dynamic model of the wheelset is provided. This model is called as plan-view model in many studies which are focusing on the dynamic analysis of the wheelset. Another textbook, which concentrates on the dynamic analysis of wheelsets and railway vehicle systems, is given by (Wickens, 2005). In this textbook, the wheelset is considered to be mounted on a bogie with massless suspension systems and it is assumed that the vehicle moves forward with a constant velocity with negligible lateral and vertical motion. The model proposed by (Wickens, 2005) includes 3 DOF and unlike the model given by (Garg and Dukkipati, 1984), rotation of the wheels about the lateral axis is also considered. (Wickens, 2005) shows that body of the vehicle does not strongly participate in the lateral motions of its wheels at high speed. Therefore, it can be concluded from these arguments that an elastically restrained wheelset dynamic model is enough to explain the dynamic behaviour of the complete system. (Iwnicki, 2006) emphasizes several aspects of the dynamics of railway vehicles, but this book is rather a collection of papers about various topics regarding the railway vehicle dynamics which includes also wheel–rail interface, suspension and suspension component design, simulation and testing of electrical and mechanical systems, interaction with surrounding infrastructure, and noise generation. MBS formulations for the dynamics of the wheelset and railway vehicles also exist in the literature and a textbook about these formulations as well as dynamic analyses are provided by (Shabana et al., 2007). One of the newest textbooks in the related area is given by (Spiryagin et al., 2014). (Spiryagin et al., 2014) report information about the design of locomotives and rolling stock, procedures for MBS formulations for the railway vehicle systems and brief information about the MBS computer packages used for the dynamic analysis of wheelsets and railway vehicles.

Hereby, the presented literature with textbooks about the dynamic analysis of the wheelset and railway vehicles presents an introduction for the analysis of different aspects of the railway vehicles.

Generally the aim of the lateral dynamic analysis is to investigate stability (i.e. safety). (Knothe and Böhm, 1999) pay particular attention to the historical development of investigations and observations on the stability due to the lateral dynamic response of the wheelset. A very first observation on the lateral dynamics of a wheelset is given by Stephenson, who is one of the first railway researchers, as cited by (Knothe and Böhm, 1999). This observation is the fact that whenever the wheelset exposes a lateral shift to the right or left; wheel, which the shift occurs towards, rolls with a great diameter. Gradually, this wheel has less diameter and the other wheel has larger diameter. This situation causes an oscillatory motion. This oscillatory motion is called as ***Hunting***. (Knothe, 2008) states that one of the very first investigations of hunting is reported by Klingel in 1883. The assumptions of the Klingel are rigid and conically profiled wheels. Klingel shows that this hunting motion is sinusoidal and its wavelength is proportional to the geometrical characteristics of the wheels. After Klingel, in 1887, another German researcher, Boedecker studies the lateral motion of the 2 axle vehicle which the wheelsets connected to a rigid frame with rigid primary suspensions, (Knothe, 2008). Boedecker concludes in his book that such a vehicle always run laterally unstable. Carter, who is also mentioned in Section 1.3, uses the same model with Boedecker to investigate the lateral stability of a rigid 2 axle vehicle with different contact mechanics. In 1935, Rocard has the same conclusion with Carter about the stability of rigid 2 axle vehicle without knowing the work of Carter. (Knothe and Böhm, 1999) report that Rocard assumes a massless bogie that is elastically connected to the chassis and shows how it can be stabilized by using appropriately chosen suspension parameters. In 1937, Heumann reveals the dynamic behaviour of the wheelset which has worn profiles in curves, and proposes a formula for the effective conicity calculation in his study, as stated by (Iwnicki, 2006). Heumann defines an analytical formula of the effective conicity w.r.t. the lateral shift of the wheelset and concludes that the effective conicity of worn profiles can be larger than the wheels which have conical profiles. Heumann also notices that worn profiled wheels tend to worn slower

than the coned profiles and proposes to use worn profiles instead of coned profiles. During second world war no research was conducted on the stability of railway vehicles, and the situation can be seen in Fig. 19 of (Knothe and Böhm, 1999). This paragraph aims to give brief insight to the related literature before fifthies.

After fifthies, the milestone of such analyses is the competition organized by office for research and experiments (i.e. ORE) of UIC. The theme of the competition was the analysis of the stability of two-axle railway vehicle (Iwnicki, 2006). It is stated that there are three papers winning a prize (by Posel, Boutefoy and Matsudaira). All of the analyses are linear and the Matsudaira's work is the only work which considers longitudinal and lateral stiffness between wheelset and frame without suspension damping. Other noticable difference of Matsudaira's study is that he considers worn profiles with circular arcs. Matsudaira give a stability chart representing the stability limits of the vehicle w.r.t. the lateral stiffness values between the car body and wheelsets. The other important factor for the lateral stability of the vehicle, which is presented for the first time in Possel's and Boutefoy's papers, is the gravitational stifness. The lateral components of the normal force is caused by that stifness and it has a stabilizing effect. However, the effect of this stiffness is countered by the contact stifness. This paragraph intends to give brief insight to the literature until sixthies.

After sixthies, researches are directed towards the validation of the analytical formulas and the other neglected factors causing nonlinear phenomena, (Iwnicki, 2006). Such a phenomena is the spin creep which occurs due to the angular motion of the wheel around the normal axis. First study is carried out by Wickens and published in 1965 and the spin creep is included into the equations of motions. In 1963, King and Pooley are conducted the first full scale experiments and take the measurements of critical speeds and mode shapes. In 1965, Gilchrist et al. carry out the validation of theories with experiments on two kinds of standart 2 axle vehicles. Despite the correctly modelled suspension characteristics, two drawbacks of the linear theory are observed. These are the saturation of creep and uncertainty in wheel-rail geometry. Laws and theories for the creep saturation have already been known, but a more correct representation of the wheel–rail geometry is required. Therefore, the equivalent conicity definition is proposed.

Equivalent conicity of a coned wheel is simply equal to the cone angle of the wheel, but for worn profiles it is defined as the cone angle which the oscillation of same wavelength would occur for coned wheels. Even nowadays, this definition is given in the related standart (EN, 2007) and is used for vehicle acceptance. In 1975, Nefzger shows that the equivalent conicity based on S1002–UIC60 wheel–rail profiles does not only depend on gauge and rail inclination, but also the amplitude of the wheelset hunting motion (Knothe and Böhm, 1999). Same year, Cooperider et al. introduce a formal mechanism which is based on the linearization of nonlinear functions to minimise mean squared error between responses and this formalism is named as *quasilinearisation*. They also report their results with a bifurcation diagram. This diagram shows the critical velocity of the vehicle w.r.t. the lateral shift or suspension parameters. (Yang, 1993) explains that De Pater studies the conventional wheelset thoroughly in 1979, 1981 and 1988. De Pater derives a set of nonlinear algebraic equations to determine the contact constraints between the track and wheelset which is subjected to two holonomic constraints and has four degrees of freedom. This paragraph is the summary of the Section 7 of the first chapter of the textbook by (Iwnicki, 2006), unless another reference is cited.

Advances in the analysis of nonlinear systems lead to the better understanding of the lateral dynamic response of the wheelset. (Jaschinski and Netter, 1992) propose a simplified wheelset model for analysis of hunting motion. This motion is especially investigated for different camber angles and coupling; results are compared with experiments on a roller rig as well, (Jaschinski and Netter, 1992). Recently, MBS approach is usually used for analysis of vehicular systems, and (Yang, 1993) presents a MBS formalism for conventional wheelset in his PhD thesis in 1993. (Yang, 1993) studies the contact constraints given by De Pater comprehensively, and first order theory proposed by De Pater is also used to simplify the nonlinear algebraic equations. Simple dynamic systems like a wheelset with strong nonlinearities can respond to inputs (i.e. track irregularities) in complex ways. Such systems can even respond different inputs in a random way. (Knudsen et al., 1994) provide an analysis of a wheelset as a chaotic system. In this case, the response can be determined, but it strongly depends on the initial conditions. Such a chaotic, symmetrical and asymmetrical motions are also observed by

(Nath et al., 2003). The effect of yaw stiffness on the hunting motion of the wheelset is investigated, (Nath et al., 2003).

Still, the stability assessment using linear (or linearized) methods for railway vehicles is being discussed. (Polach, 2006) compares the nonlinear and linear methods for stability assessment of railway vehicles. The term linearised means quasilinearised which is mentioned in previous paragraphs, (Polach, 2006). It is concluded that linearized calculations can be used for preliminary conclusion about the stability, but nonlinear analyses must be carried out as well. Because equivalent conicity does not take nonlinearity into account, (Polach, 2010) introduces a new parameter named as nonlinearity parameter. This parameter mainly represents the conicity value for sufficient lateral track clearance between wheel and track.

In the literature, there exist also nonlinear methods for stability assessment or analysis. These methods include having solid grasp of the wheel–rail geometry, wheel–rail contact, normal and tangential problem. This paragraph intends to give fairly new studies which present nonlinear methods. A nonlinear dynamic analysis of wheelset, bogie and railway vehicle is reported by (Pombo et al., 2007). Wheel–rail is the crucial part of the nonlinear dynamic analysis and an online contact search formalism considering rails' spatial geometry and irregularities is proposed by (Pombo et al., 2007). (Bozzone, 2009), in his PhD thesis, investigates the approach for a computationally efficient contact model which can be applied in dynamic analysis of railway vehicles since simultaneous solution to all of the problems (geometrical, normal, tangential) previously mentioned has high computational complexity to apply for railway vehicle simulations. A model for dynamic behaviour of wheelsets is also given by (Anyakwo et al., 2012) and solutions to geometric, normal and tangential problem are revealed. (Anyakwo et al., 2012) derive nonlinear equations and solve them with Newton–Raphson method similar to the De Pater's previously mentioned work. An attempt to formulate dynamic equations of the wheelset is given also by (Liu, 2014) similar to the study by (Anyakwo et al., 2012). In analysis, roll angle of the wheelset is taken into account by using semi–analytical method mentioned in Section 1.1, (Liu, 2014).

The state of art methods for dynamic analysis of railway vehicles are based on the

use of available commercial MBS tools. The reasons for using such simulations w.r.t. full scale experiments are

- Conducting simulations are cheaper than full scale track testing and there is no need to interrupt schedule for full scale experiments,
- In simulations, inputs can be diverse and inputs in extreme conditions can even be applied and tested,
- Some variables or states can be obtained easily which they are difficult to obtain in real world situations (e.g. contact forces, contact positions etc.) as emphasized by (Evans and Berg, 2009).

(Elsayed Shaltout, 2013) develops a computational model for the analysis of railway vehicle dynamics based on MBS formalism proposed by (Shabana et al., 2007). It is indicated by (Michálek and Zelenka, 2011) that these commercial MBS tools has a black box tool structure from users' point of view and assessing computational models completely can be cumbersome. That is one of the disadvantages of MBS tools and the second one is the accessibility of these tools by researchers. Since these are commercial tools, they are difficult to obtain (i.e. buy). Therefore in this thesis, the collection of tools for solutions and simulations mentioned in previous sections and paragraphs are used. An example for the use of mentioned methods for dynamic analysis is reported by (Onat et al., 2015).

1.5 Estimation Scheme and Application of Estimation for Wheelset and Railway Vehicles

Advances in statistical mathematics lead to the estimation and tracking of dynamic systems. Even the estimation of nonlinear Gaussian or non–Gaussian systems is possible with a computational complexity drawback. Estimation methods, which are based on Bayesian inference methods, require a set of states and parameters dependent on the measurements or observations. (Haug, 2012) reports that for estimation procedure two models can be defined. First model includes unobservable, nonrandom and constant variables during the observation (or measurement) and second model includes random variables which have the prior probability and noisy observations as well. In this

dissertation, the estimation scheme, which is called Bayesian estimation, is based on the second model. This estimation scheme includes the recursive Bayesian formalism introduced by Reverend Tomas Bayes, which is emphasized by (Haug, 2012). This formalism is the basis of the estimation scheme considered in this dissertation and can be summarised as follows:

1. Start with some prior belief on system states and parameters,
2. Use this prior belief and dynamic model for a prediction,
3. Update prediction with observations (i.e. measurements) by using an observation model to have a posterior belief,
4. Posterior belief is now prior belief, go to the step 2.

Since the estimation methods used in this dissertation are based on the seminal work by Rudolph E. Kalman, a literature summary should be given accordingly. Studies based on the Kalman filtering start with the original paper of Kalman, (Kalman, 1960). Kalman emphasizes the statistical nature of a class of theoretical and practical problems in communication and control. These are (i) prediction of random signals (ii) seperation of random signals from random noise (iii) detection of signals of known form. Kalman's study is based on the pioneering work of Wiener as reported by (Kalman, 1960). Kalman also describes the problems which can be studied with the notation that signal is presented by $x_1(t)$ and noise $x_2(t)$, the assumption of observation can be given as a sum $y(t) = x_1(t) + x_2(t)$. Supposing the exact values for observations (i.e. measurements) up to now are available as $y(t_0) \dots y(t)$. This knowledge of the system can be used (or infered) to obtain the unobservable signal at $t = t_1$. If $t_1 < t$ this scheme is called *data-smoothing (interpolation) problem.* If $t = t_1$ it is called *filtering.* If $t_1 > t$ it is named as *prediction problem.* Kalman chooses the filtering and smoothing problem. Kalman Filter is optimal in sense of expectations (i.e. mean) and using the fact that conditional distributions of Gaussian random process are Gaussian. Theorems and proofs can be found in (Kalman, 1960).

Kalman Filter can only be applied to linear systems successfully. (Grewal and Andrews, 2015) indicate that Stanley F. Schmidt studies associated navigation and guidance problem at the NASA Ames Research Center during the announcement of

Apollo project to send Americans to the surface of the moon and back. It is an already standard practice to use numerical partial differentiation to linearise problems, and Schmidt is the first to recognize potential of Kalman Filtering for this application. The preliminary performance studies are not using full Kalman Filter structure but only covariance computations. Then, Schmidt notices that this linearization procedure can be applied for state estimates. Schmidt calls this filtering scheme as Extended Kalman Filter (i.e. EKF), but after some modifications done by Schmidt, it is recognized as Schmidt–Kalman Filter. The application of EKF for wheelsets or railway vehicle systems is limited because this scheme requires the Jacobian matrices for system model. In case of wheelsets or railway vehicle systems, if linearised models are considered, Kalman Filter and/or Extended Kalman Filter scheme can be applied.

Until UKF (i.e. Unscented Kalman Filter) is introduced, EKF is the one of the most widely used estimation algorithm for nonlinear systems as reported by (Julier and Uhlmann, 2004). EKF has its drawbacks, such as implementation and tuning difficulty. Many of these difficulties arise from linearisation process. Nonlinear filtering method used in this dissertation, namely Unscented Kalman Filter (i.e. UKF), dates back to the study by (Julier et al., 1995). In UKF, states and parameters are again represented by Gaussian random variables from a set of carefully chosen sample points (Wan and Van Der Merwe, 2001). These sample points are named as sigma points and the several versions and detailed explanations of sigma point Kalman filters are provided by (Van Der Merwe, 2004). Readers are referred to the studies by (Kandepu et al., 2008), (Matzuka et al., 2012) which are explaining the application of UKF in nonlinear dynamic systems so that the researchers from all branches of science can understand and apply UKF for nonlinear dynamic systems. In addition, a review of performance measures for such kind of filters can be found in (Haug, 2012).

This paragraph aims to give the related literature briefly to show the evolution of applications of Kalman filters in the area of dynamic analysis of the wheelset and railway vehicles. Use of model based filtering for railway vehicles is not a new concept. Nevertheless, the focus of such model based filtering schemes is mostly estimating the conditions of primary and secondary suspension systems. This is called as *condition*

monitoring and this scheme helps to arrange more efficient maintenance schedules. Examples of a such scheme are presented by (Ward et al., 2011) and (Zhongshun et al., 2014). Previously reported studies reveal that different friction (i.e. adhesion) conditions cause different dynamic responses, especially for the wheelset. A very first attempt of detection of the low adhesion by using a Kalman filter is given by (Charles et al., 2008a). It is proposed by (Charles et al., 2008a) that in order to estimate the low adhesion conditions accurately, more knowledge about the wheel–rail contact must be included. Therefore, it is concluded in the same work that effort must be directed towards estimating the contact forces. (Hussain et al., 2013) propose a multiple model estimation scheme based on the Kalman filtering for the adhesion condition estimation. Instead of estimating the contact forces or moments, the residuals of a set of Kalman filters are analysed. These filters are operating in different points of the creep force–creepage curves. This multiple model scheme given by (Hussain et al., 2013) also requires a post–processing stage to interpret the adhesion conditions from residuals of Kalman filters. Besides, the wheelset considered by (Hussain et al., 2013) has coned wheels which is not realistic since across the globe worn wheel profiles are recently used. The advantage of this plan view dynamic model is that it also consists of torsional dynamic model of the wheelset which can provide extra information in distinguishing different operating points where the dynamic response of the wheelset is same. A model based adhesion estimation scheme is reported by (Ward et al., 2012) based on the contact forces and moments analysis. The dependence of the creep forces and moments upon the level of track irregularity is emphasized by (Ward et al., 2012) as it makes difficult to interpret the adhesion conditions without the prior knowledge of the track irregularity. However, it has also shown that the adhesion conditions can be estimated based on the eigenvalue analysis without the prior knowledge of the track irregularity level. (Hubbard et al., 2013) demonstrate a non–model based method including the comparison of the dynamic responses of leading and trailing wheelsets. In this non–model based estimation scheme, the yaw positions of the leading and trailing bogies are used. A search to find a cross correlation of all dynamic variables of the leading and trailing bogies is conducted and it is concluded that the biggest change in correlation is in the yaw angle and it can be used for interpretation. The main problem

in such model based estimation schemes is to decide a model which represents the physical system exactly in each condition. Dynamic modelling of railway vehicles for estimation purposes is not an exception. Especially at very low adhesion conditions, because of the decreasing creep forces, the restorative force due to the gravitational stiffness term becomes dominant force with respect to creep forces at the wheel–rail contact (Hubbard et al., 2014). Therefore, modelling errors due to the linear contact approximation cause problems in order to identify very low adhesion conditions. Based on a nonlinear contact approximation, a comparison study between lateral dynamic responses of a two DOF dynamic model of a wheelset and a MBS model is provided by (Hubbard et al., 2014). It is concluded and shown that a two degree of freedom dynamic model of a wheelset is sufficient to capture lateral dynamic response of a wheelset with respect to lateral track irregularities. This two DOF lateral dynamic model of the wheelset is also considered in this dissertation. Studies, which are related with this dissertation and carried out in this context, are presented by (Onat et al., 2016b,c).

1.6 Roller–Rigs

In order to verify the safety and performance of the railway vehicles, on–track experiments and measurements are essential. These experiments are generally carried out with specially equipped vehicles. Additionally, measurements and experiments can take even months. During these measurements and tests, qualified test personnel is also a must. The use of vehicles for safety and performance assessment comes with a great expense. Therefore, alternative methods to assess safety and performance of the vehicles are needed. An effective solution to overcome this issue is the use of specially designed roller–rig test stands.

A review article by (Jaschinski et al., 1999) investigates the several roller–rigs used around the world and their applications for railway research up to 1999. More recent textbook by (Bosso et al., 2013) presents the historical development and all other aspects of the roller–rigs. Zhang et al. also cover the similar topics in the chapter 14 of the textbook by (Iwnicki, 2006). The brief information about the historical development of roller–rigs, which is provided in this section, is based on these sources. Therefore, it is

recommended for readers to read these references for details.

Reported roller–rig configurations in the related literature differ in size. According to the size, roller–rigs can be specified as full scale and reduced scale. Full scale roller–rigs are useful to understand the behaviour of complete vehicle systems, whereas scaled roller–rigs are the cheap, easy to construct and purpose specific version of the full scale ones.

This paragraph intends to give the brief information on the historical evolution of the important roller–rigs for railway research across the globe. One of the first full scale roller–rig was used in the United Kingdom in order to verify the performance of a steam locomotive in 1904. As reported by (Jaschinski et al., 1999), one of the most important study on railway vehicle dynamics was presented by Carter where he tested his models on a small scale track in 1920s. After the second world war, researches on railway vehicles gathered pace. One of the prize winning researcher Matsudaira indicated the significance of suspension to stabilise a wheelset and he supported his theoretical work with 1/10 and 1/5 scale models in the 1950s and first reported in 1952, as indicated by (Jaschinski et al., 1999). In the early 1950s a 1/10 scale model roller–rig is used for performance assessment of new lightweight passenger trains and a freight car in the United States. In 1962, the Research Department of British Railways built a dynamically scaled 1/5 model roller–rig and full scale two–axle roller–rig in 1963-64, (Jaschinski et al., 1999). In 1964, a French private company built a roller–rig which allows lateral and vertical motions of each axle so that running safety and ride performance can be investigated, (Iwnicki, 2006). In 1963-64, the Research Department of British Railways built full scale two-axle roller–rig to support the theoretical work, to demonstrate the instabilities experienced by current designs of rolling stock and experiments were carried out on the lateral stability of two-axle vehicles, (Jaschinski et al., 1999). A roller–rig, which allows evaluation of traction equipment, acceptance tests for vehicle springs, and assessment of braking systems, was built in Berlin, Germany (Iwnicki, 2006). In 1977, a full-scale roller–rig was built in Munich, Germany at Deutsche Bahn AG. The rollers have four degrees of freedom including vertical, lateral, inclination, and rotation. The servohydraulic excitation control system was adopted for the roller–rig and it can accurately simulate track conditions for the dynamic simulation of

a vehicle operating on tracks and it has played a very important part in the development of ICE high-speed trains, (Iwnicki, 2006). In 1978, a roller rig, which is called the Roll Dynamics Unit, began to operate in the United States with the capability to handle cars and locomotives at full speed and power and with the vibrations applied through the wheels to simulate track conditions, (Jaschinski et al., 1999). In 1995, a four-axle roller–rig was built at the State Key Laboratory of Traction Power (Southwest Jiaotong University) at Chengdu, China. This roller rig was built for the optimum design and testing of railway vehicles, (Iwnicki, 2006).

Roller–rigs are extensively used for a better observation of the wheel–rail contact, adhesion, traction phenomena. According to the research purpose, the substitution of the rail with the roller and the vehicle with the substitutive configuration differ. The details of the several cases for substitution and the differences from real case are reported by (Liu and Bruni, 2015; Voltr, 2015).

For many years, experimental research has been conducted in Jan Perner Transport Faculty (i.e. DFJP), University of Pardubice (i.e. UPCE), Czech Republic on a test stand originally built by Výzkumný Ústav Kolejových Vozidel–Rail Vehicle Research Institute (i.e. VÚKV). Extensive reconstruction has been made at the Jan Perner Transport Faculty. Adhesion (Voltr and Lata, 2015; Voltr et al., 2009, 2012) and traction (Cerný et al., 2007; Doleček et al., 2009) are the focus of the research by using this tram wheel test stand. This test stand is a full scale roller rig which has a wheel on roller configuration. This wheel on roller configuration has some advantages and disadvantages, (Meymand, 2016). Most significant advantage of such configuration is that it provides better contact mechanics (adhesion, contact geometry, creep forces, etc.) studies. Obviously, the disadvantage is that it does not allow to study hunting and curving dynamics.

Especially, the effect of adhesion conditions is studied extensively on roller–rigs which have wheel on roller configuration,(Bosso et al., 2015; Wang et al., 2011). In order to simulate such adhesion conditions, water, oil, sand, lubricants etc. are used by (Bosso et al., 2015; Wang et al., 2011). Use of such contaminants causes wear and defects on wheel and roller surface. This situation degrades the accuracy in such studies as contact is directly formed by the profiles. During experiments, measuring profiles and rolling

radii is a difficult process and can cause long delays in the experiments. For the case in real vehicles, such wear and defects can even cause safety problems. In this dissertation, estimation of the rolling radius of the wheel of the existing test stand is aimed.

2 *Dissertation Objectives*

Adhesion conditions, rolling radius of the wheel, suspension parameters etc. are the examples of parameters that can affect the run of a vehicle. Even, these parameters can cause safety and operation critical situations. For example, a change in adhesion conditions can cause delays in the operation because of the long breaking and acceleration distances for very low adhesion conditions. Another example can be given as the rolling radius of the wheel since very low values of the rolling radius due to severe wear with respect to the nominal case can cause safety problems.

Shortly, the main objective is to test use of model based filtering methods for the parameter estimation of the wheelset and railway vehicles. These model based filtering methods require the good understanding of the physical system. Instead of using an MBS tool, which has a black box structure as stated previously, models representing the physical system must be generated to apply estimation approach. Creating models, which are forming the overall system, were determined as the sub–objectives in this dissertation. These are:

1. Determination of the wheel–rail profiles is essential such that the interaction of these two profiles forms the contact. In this dissertation, first objective is to understand and present solution methods to solve geometrical problem.
2. After the geometrical problem is solved, the second objective is to solve the normal problem. By using the outputs of the solution to the geometrical problem, contact patch dimensions are obtained by using the solution methodology considered in this dissertation.
3. Determination of the contact patch leads to the solution of the tangential problem. In order to obtain dynamic response of a wheelset (or a tram wheel on test stand), forces occurring in the contact patch are vital. In this dissertation, methods to solve the tangetial problem are presented.
4. As well as contact forces, there are other sources that can affect the dynamics of a wheelset. These sources are the track irregularities and the traction devices like electric motors attached to the wheelset. Therefore, another objective in this dissertation is to model these sources so that effect of these sources on dynamic

response can be investigated for parameter estimation.

5. According to the estimated parameter, a suitable dynamic model of the investigated system must be identified. Furthermore, this model must be strongly connected with the parameter so that it can be detected by using the dynamic response.
6. Another objective is to interpret the data obtained from dynamic response. The family of Kalman type filters are extensively used in the context of this dissertation.
7. Additionally, model based filters require the measurements (observations). These measurements can be simulated or taken from a test stand (or a real vehicle). Another objective is to create these measurements or obtain them from a test stand.

The overall structure of the system is illustrated by a diagram given in Figure 2.1.

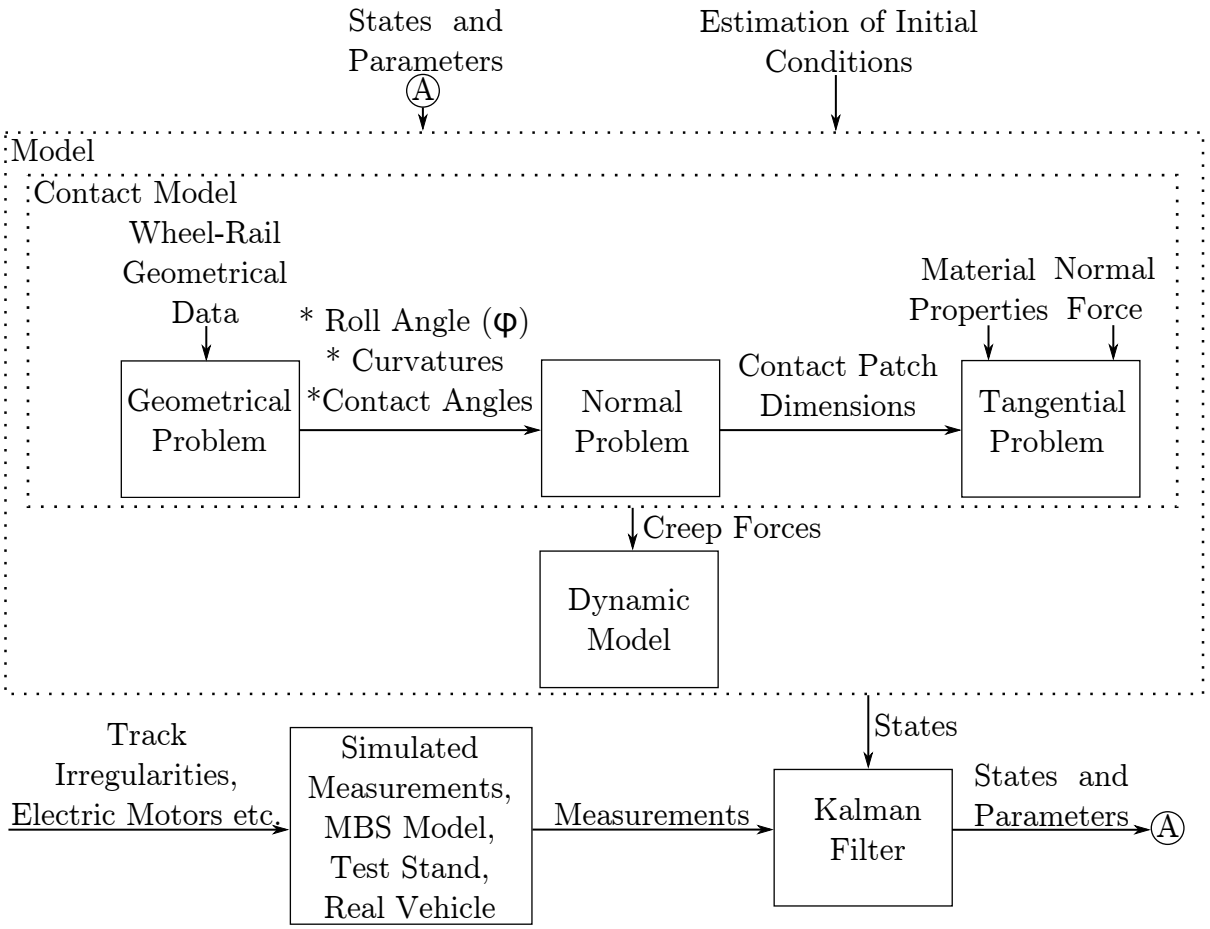

Figure 2.1: Overall structure of the system (to realise main objective) and sub–models (to realise sub–objective) of the considered system

3 *Overview of the Selected Methods and Models*

3.1 Wheel–Rail (Roller) Contact Geometry and Contact Search

3.1.1 Wheel–Rail (Roller) Geometries and Specifications

The wheel, which is considered in this study, has a theoretical S1002 profile and rail has a theoretical UIC60E1 profile as mentioned previously. It should be noted that the rails are imbedded in track with an inclination in practice. The value of 1:40 for is used here. The rail profile data is rotated about the track gauge distance measurement point by using the well–known Euler's rotation theorem during the application. Track gauge is taken as 1435 mm in this work. Track gauge measurement point is accepted as the point under the 14 mm of the top of rail (i.e. TOR). This wheel–rail profile is used while analysing the dynamic response of a wheelset.

Due to extensive use of the tram wheel test stand in Jan Perner Transport Faculty, Pardubice, Czech Republic originally built by VÚKV, the wheel has recently been reprofiled by considering the theoretical profile of the wheel, namely "VM", used in Prague trams and designed by VÚKV. The roller is also reprofiled by considering the theoretical profile of the rail, namely "NT1", and designed by the manufacturer Třinecké Železárny, Czech Republic.

For the S1002 wheel presented by (UIC, 2004), sections of the profile are given as lines and curves with equations of coordinates. The profile can be discretized by using these equations. In this dissertation, the wheel profile is discretized with a 0.01 mm step. However, for the rail profile, instead of such equations, only the technical drawing of the profile is provided by (EN, 2011). In order to discretize the rail profile, mathematical tools from analytical geometry are used. It should be noted that rail profile includes the circular arcs and lines. Therefore, the equations of coordinates for the UIC60E1 profile is obtained by using the line and circular arc equations from the analytical geometry. Center points of the circular arcs and reference points for the lines are already indicated in the technical drawing. A plot of the wheel–rail profiles can be seen in Figure 3.1a.

The geometrical data of the nominal profiles of the wheel–roller of the tram wheel test stand is provided by Transport Means and Diagnostics Department of University of

Pardubice, Czech Republic. As well as nominal profiles, real wheel–roller profiles measured by a mini–prof device are also provided. Measured wheel–roller profiles are illustrated in Figure 3.1b. Furthermore, a comparison between measured and nominal profiles of the tram wheel test stand is presented in Figure 3.2. The wear in the wheel of the test stand is not clearly observable, but there is about an 1 mm wear in the diameter around the region of rolling, whereas the wear can clearly be seen from the Figure 3.1a.

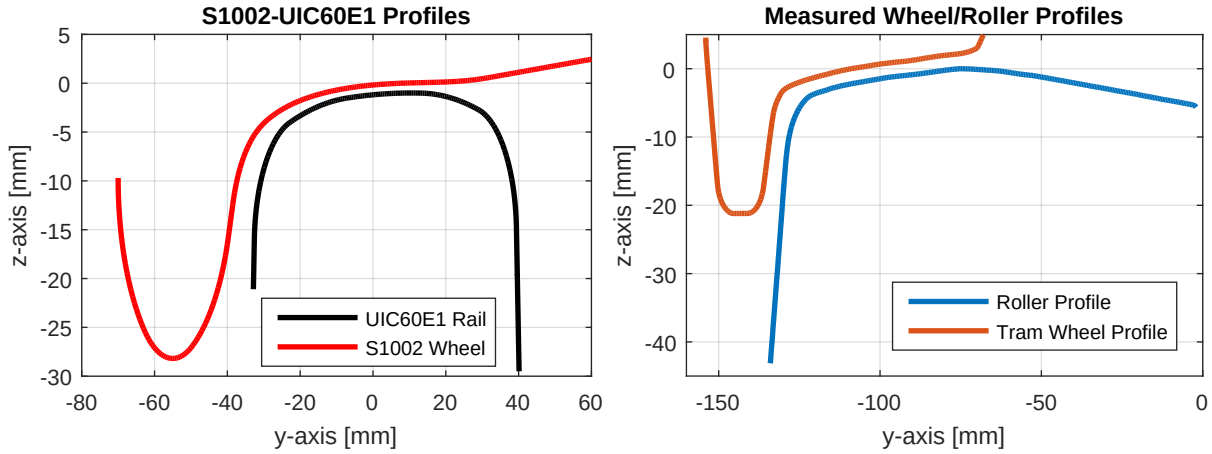

(a) S1002–UIC60E1 wheel–rail pair **(b)** Measured wheel–roller profiles

Figure 3.1: S1002–UIC60E1 wheel-rail profiles and measured wheel–roller profiles

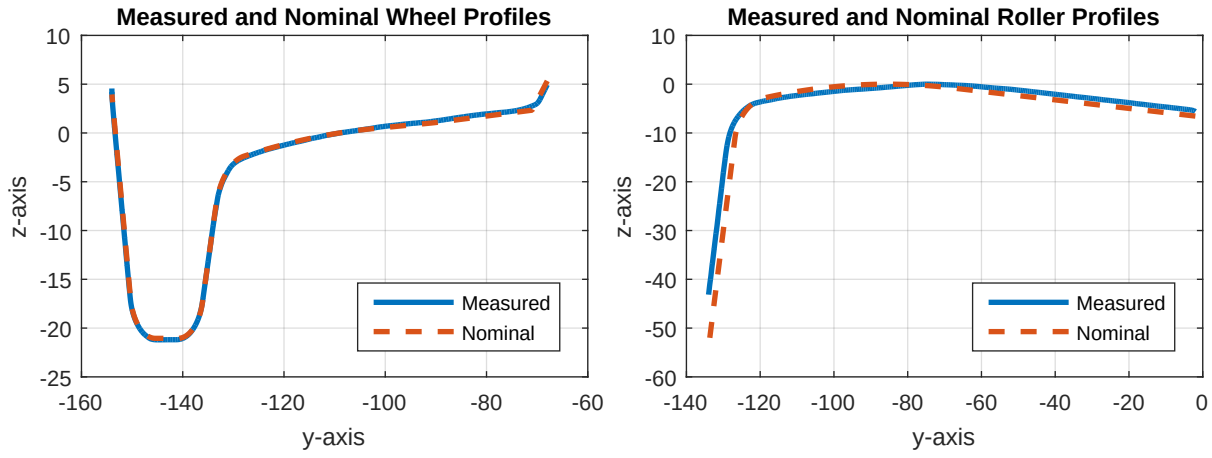

(a) Wheel of the stand **(b)** Roller of the stand

Figure 3.2: Comparison of measured and nominal wheel–roller profiles

Conicity angles for wheel–rail (and roller) must be found, as this characteristic is especially important about finding the components of contact forces. The conicity angle

is defined as

$$tan\delta_p = \frac{dz_p}{dy_p}, \tag{3.1}$$

where γ_p represents the conicity angle of the respective profile, z_p and y_p are the vertical and lateral axes of the considered profile, respectively. In order to obtain the conicity angles, first derivative of the vertical axis w.r.t. lateral axis is required. In order to find this derivative, numerical derivation method provided by (Fornberg, 1988) is used. This method is preffered because of its usability for also worn profiles. For a second degree of accuracy, forward derivation equation is given by

$$\frac{dz_p}{dy_p} = \frac{z_p(j) - z_p(j-1)}{h}, \tag{3.2}$$

where numerator equals to the difference between consecutive points in z–axis and denominator h equals to the difference between consecutive points in y–axis (i.e. $y_p(j) - y_p(j-1)$).

Lateral and longitudinal curvatures of the profiles must also be obtained. In the wheel–rail case, it can be obtained by using the geometrical data. However, for measured profiles of the wheel–roller, especially the lateral curvatures must be calculated. In order to find signed lateral curvature of the wheel–roller profiles, the expression is defined as

$$\kappa_p = \frac{\frac{d^2 z_p}{dy_p^2}}{\left(1 + \left(\frac{dz_p}{dy_p}\right)^2\right)^{\frac{3}{2}}}. \tag{3.3}$$

3.1.2 Rigid Contact Search & Semi–Analytical Method for Contact Locus

Rigid contact search method is based on finding the minimum distance on the z–axis. Condition for the contact point is

$$\min d(y_p, z_p) = 0, \tag{3.4}$$

where d represents the distance between wheel–rail (or roller) profiles. In other words, rigid contact search is a numerical method based on finding the zeros of the distance function given in Equation 3.4. Rigid contact search method is computationally fast. However, since it does not consider the elasticities of the bodies, results found by this method are not accurate.

In the wheel–rail case, due to the curvilinear profiles of the wheel, lateral shift of the wheelset causes roll angle in the center of wheelset and this roll angle changes contact locus on both wheels. In order to find contact locus on each wheel, this effect must be taken into account. This is illustrated in Figure 3.3. Semi–analytical method given by (Li, 2002) provides a solution for this effect and it is based on the fact that the vertical distances at the contact points of right and left wheels are equal.

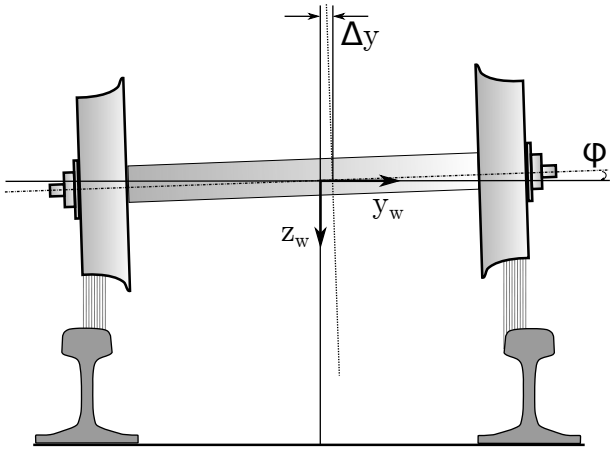

Figure 3.3: Roll angle due to the lateral shift of the wheelset

As presented in Equation 3.4, first step is to find vertical distance and calculate the respective minima d_{min_r}, d_{min_l} for each point. If these two points are contact points, then these minima are equal. If they are not equal, roll angle must be adjusted. Supposing $d_{min_r} > d_{min_l}$, then the wheelset must be rotated clockwise with an angle

$$\Delta\phi = \frac{d_{min_r} - d_{min_l}}{y_{min_l} - y_{min_r}}. \tag{3.5}$$

Rotation must be repeated until distances for two contact points are equal. Equality is

satisfied in terms of tolerance ϵ. This means

$$|d_{min_r} - d_{min_l}| < \epsilon_s. \tag{3.6}$$

10^{-4} is enough tolerance for engineering calculations. Finally, roll angle can be found as the sum of incremental rotations

$$\phi = \phi_0 + \sum_{i=1}^{k} \Delta\theta_i, \tag{3.7}$$

where k is the number of iterations and ϕ_0 is the initial roll angle. In this dissertation, initial roll angle is taken as zero for all lateral shifts.

3.1.3 Quasi–Elastic Contact Search

Elastic contact search method is a more realistic approach, but it requires use of finite element methods and computational complexity is very high. In this dissertation, the quasi-elastic method is considered, which is presented by (Arnold and Netter, 1997; Netter et al., 1998; Schupp et al., 2004). This method has lower computational complexity than elastic contact search and is more accurate than rigid contact search. Figure 3.4 demonstrates the parameters used for quasi-elastic method.

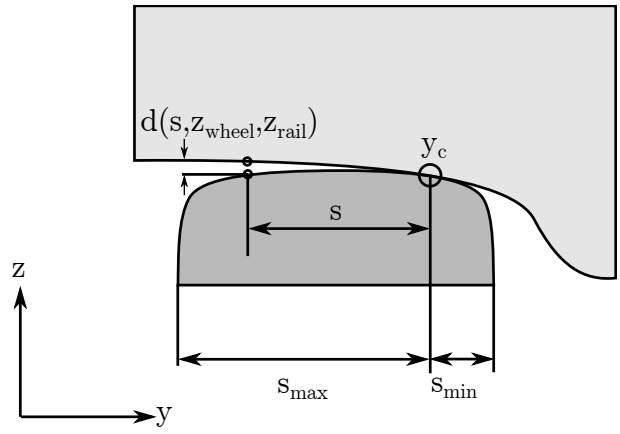

Figure 3.4: Illustration of the definitions for quasi–elastic contact search

$d(s, z_{wheel}, z_{rail})$ is considered as the distance between two corresponding points on the wheel and the rail curves in vertical direction and it depends on the lateral wheel profile coordinate s which represents the lateral distance of the consecutive points with

respect to the rigid contact point and is defined as $s = y - y_c$. Necessary condition for the contact is $\frac{\partial}{\partial s}\left(d(s, z_{wheel}, z_{rail})\right) = 0$, as stated by (Netter et al., 1998). Especially for worn profiles, the location of the contact point can be discontinuous with respect to s. Due to these jumps of the contact point, the rigid contact condition given in Equation 3.4 is only piecewise differentiable while the integration algorithm requires system equations to be at least two times differentiable, (Netter et al., 1998). The maximum deformation occurs at the contact patch and deformation decreases for other distant points. Relationship between deformations of both surfaces is assumed to be exponential. The weight function w.r.t. the distance function can be given by

$$w(s, z_{wheel}, z_{rail}) = exp\left(\frac{-d(s, z_{wheel}, z_{rail})}{\epsilon_{reg}}\right), \tag{3.8}$$

where ϵ_{reg} is the regularization parameter indicated by (Netter et al., 1998). It should be noted that the points far from contact patch are negligible as weight function increases with an increasing vertical distance. The regularization parameter is chosen so that vertical displacement of the wheel has same size as the elastic deformation in pure elastic normal contact model, (Arnold and Netter, 1997). Such a quasi–elastic contact model avoids unrealistic step changes of the contact point location which are known from the classical rigid contact model, (Netter et al., 1998). For the selected S1002 wheel and UIC60E1 rail profiles, it is in the range of $10^{-5} \ldots 5 \times 10^{-5}$ and in this dissertation, it is taken as 2×10^{-5} which is the same value considered by (Arnold and Netter, 1997). The new contact location in terms of s is given by

$$\bar{s} = \frac{\int_{s_{min}}^{s_{max}} s.w(s, z_{wheel}, z_{rail})ds}{\int_{s_{min}}^{s_{max}} w(s, z_{wheel}, z_{rail})ds}. \tag{3.9}$$

The assumption M2 of the study by (Arnold and Netter, 1997) is also valid for this study. This assumption includes the consideration of the undeformed surfaces as paraboloids locally so that Hertzian contact model can be applied. However, in order to use theory of Hertz, also curvatures around the contact patch must also be averaged by

using weights. The same weight function given in Equation 3.8 is also used. Only if this approach is used, approximation of the surfaces for the wheel–rail in the contact patch is obtained. Like Equation 3.9 curvatures can be expressed as

$$\bar{\kappa} = \frac{\int_{s_{min}}^{s_{max}} \kappa.w(s, z_{wheel}, z_{rail})ds}{\int_{s_{min}}^{s_{max}} w(s, z_{wheel}, z_{rail})ds}. \tag{3.10}$$

3.2 Solution of the Normal Problem

3.2.1 Theory of Hertz

In 1882, Hertz proposed a theory to find area of contact between nonconformal bodies, (Hertz, 1882). Hertz assumed the contact area as an ellipse, in general. Furthermore, he assumed the bodies as elastic half–spaces. This assumption means that contact stresses can be separately evaluated without considering the stresses in each body. This assumption is valid when the dimensions of the each body is much bigger than the dimensions of the contact area, (Shabana et al., 2007). Hertz did not consider the effect of tangential forces (i.e. frictionless surfaces) and he assumed small elastic deformation of the bodies in static loading.

Hertz presumed that the two bodies are in contact as illustrated by Figure 3.5. Considering the assumptions of Hertz, shape of each surface can be given in the form

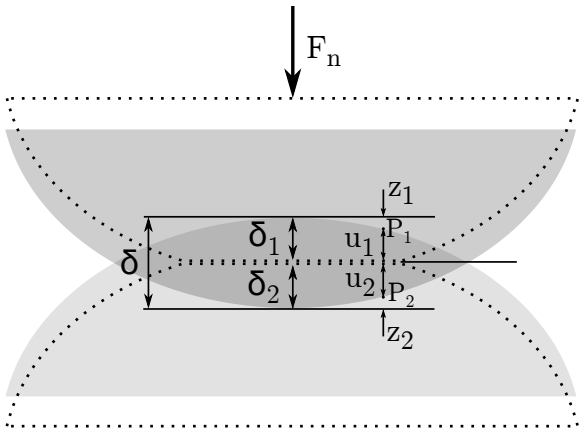

Figure 3.5: Displacement and indentation of bodies under an applied load

$$z_1 = A_1 x_1^2 + B_1 y_1^2 + C_1 x_1 y_1 + \ldots, \tag{3.11a}$$

$$z_2 = A_2 x_2^2 + B_2 y_2^2 + C_2 x_2 y_2 + \ldots \tag{3.11b}$$

By considering the shape of the bodies and neglecting other terms, contact shape is also given by

$$z = Ax^2 + By^2. \tag{3.12}$$

Assumptions of the Hertz for geometries are illustrated in Figure 3.6, similar to the illustrations by (Santos et al., 2004).

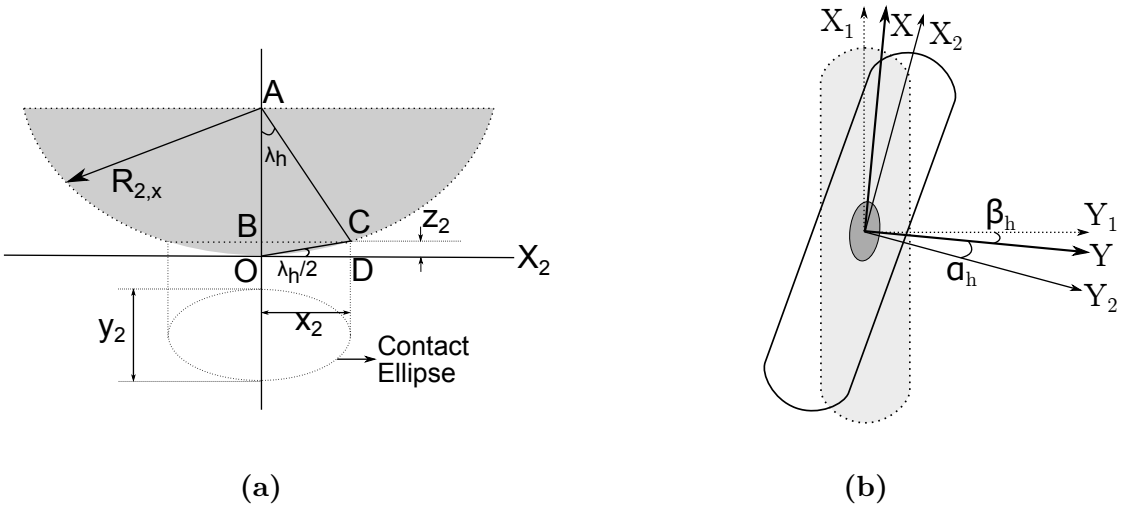

Figure 3.6: Deformations in the contact surface

For example, the shape of the second body, which is assumed as the nonconformal body, implies small λ_h. Considering the OCD triangle in Figure 3.6a, z_2 can be found from

$$z_2 = x_2 tan\left(\frac{\lambda_h}{2}\right) = \frac{1}{2} x_2 \lambda_h. \tag{3.13}$$

Hertz indicates the small elastic deformation so that line segment AB in Figure 3.6a

approximately equals to $R_{2,x}$. From ABC triangle in Figure 3.6a, λ_h is obtained by

$$tan(\lambda_h) = \lambda_h = \frac{BC}{AB} = \frac{x_2}{R_{2,x}}. \tag{3.14}$$

Substituting Equation 3.14 into Equation 3.13

$$z_2 = \frac{x_2^2}{2R_{2,x}}, \tag{3.15}$$

and likewise for the y–axis

$$z_2 = \frac{y_2^2}{2R_{2,y}}. \tag{3.16}$$

For an arbitrary point which is not on the main axes (i.e. x_2 and y_2), shape of the body is simply the sum of Equation 3.15 and 3.16

$$z_2 = \frac{x_2^2}{2R_{2,x}} + \frac{y_2^2}{2R_{2,y}}. \tag{3.17}$$

Similar derivation is made for the first body and shape of the first body is given by

$$z_1 = \frac{x_1^2}{2R_{1,x}} + \frac{y_1^2}{2R_{1,y}}, \tag{3.18}$$

and the total shape of the contact

$$z = z_1 + z_2 = \frac{x_1^2}{2R_{1,x}} + \frac{y_1^2}{2R_{1,y}} + \frac{x_2^2}{2R_{2,x}} + \frac{y_2^2}{2R_{2,y}}. \tag{3.19}$$

In Equation 3.19, all coordinates must be put into same coordinate system. Coordinate system of the second body can be transformed into the reference coordinate system (i.e. x, y) as

$$\begin{bmatrix} x_2 \\ y_2 \end{bmatrix} = \begin{bmatrix} cos(\alpha_h) & sin(\alpha_h) \\ -sin(\alpha_h) & cos(\alpha_h) \end{bmatrix} \begin{bmatrix} x \\ y \end{bmatrix}. \tag{3.20}$$

The relation between the first body coordinate system and the reference coordinate system

(i.e. x, y) can be expressed as

$$\begin{bmatrix} x_1 \\ y_1 \end{bmatrix} = \begin{bmatrix} cos(\beta_h) & -sin(\beta_h) \\ sin(\beta_h) & cos(\beta_h) \end{bmatrix} \begin{bmatrix} x \\ y \end{bmatrix}. \tag{3.21}$$

Substituting Equations 3.20 and 3.21 into 3.19

$$\begin{aligned} z = &\frac{1}{2R_{1,x}}(cos^2\beta_h x^2 + sin^2\beta_h y^2 - 2cos\beta_h sin\beta_h xy) + \\ &\frac{1}{2R_{1,y}}(sin^2\beta_h x^2 + cos^2\beta_h y^2 + 2cos\beta_h sin\beta_h xy) + \\ &\frac{1}{2R_{2,x}}(cos^2\alpha_h x^2 + sin^2\alpha_h y^2 + 2cos\alpha_h sin\alpha_h xy) + \\ &\frac{1}{2R_{2,y}}(sin^2\alpha_h x^2 + cos^2\alpha_h y^2 - 2cos\alpha_h sin\alpha_h xy), \end{aligned} \tag{3.22}$$

and by comparing Equation 3.22 with 3.12, it is obvious that in order to satisfy Equation 3.12, sum of terms with xy must be zero

$$\begin{aligned} &\frac{1}{2R_{1,x}}(-2cos\beta_h sin\beta_h xy) + \frac{1}{2R_{1,y}}(2cos\beta_h sin\beta_h xy) + \\ &\frac{1}{2R_{2,x}}(2cos\alpha_h sin\alpha_h xy) + \frac{1}{2R_{2,y}}(-2cos\alpha_h sin\alpha_h xy) = 0, \end{aligned} \tag{3.23}$$

and organising this equation

$$\left(\frac{1}{2R_{2,x}} - \frac{1}{2R_{2,y}}\right)(2cos\alpha_h sin\alpha_h) - \left(\frac{1}{2R_{1,x}} - \frac{1}{2R_{1,y}}\right)(2cos\beta_h sin\beta_h) = 0, \tag{3.24}$$

and finally this leads to

$$\left(\frac{1}{2R_{2,x}} - \frac{1}{2R_{2,y}}\right)(sin2\alpha_h) = \left(\frac{1}{2R_{1,x}} - \frac{1}{2R_{1,y}}\right)(sin2\beta_h). \tag{3.25}$$

This equation defines a triangle. Polynomial equality between Equation 3.22 with 3.12

provides

$$\begin{aligned} A+B =& \frac{1}{2R_{1,x}}(cos^2\beta_h + sin^2\beta_h) + \frac{1}{2R_{1,y}}(sin^2\beta_h + cos^2\beta_h) + \\ & \frac{1}{2R_{2,x}}(cos^2\alpha_h + sin^2\alpha_h) + \frac{1}{2R_{2,y}}(sin^2\alpha_h + cos^2\alpha_h), \\ A+B =& \frac{1}{2R_{1,x}} + \frac{1}{2R_{1,y}} + \frac{1}{2R_{2,x}} + \frac{1}{2R_{2,y}}, \end{aligned} \tag{3.26}$$

likewise

$$\begin{aligned} B-A =& \frac{1}{2R_{1,x}}(sin^2\beta_h - cos^2\beta_h) + \frac{1}{2R_{1,y}}(cos^2\beta_h - sin^2\beta_h) + \\ & \frac{1}{2R_{2,x}}(sin^2\alpha_h - cos^2\alpha_h) + \frac{1}{2R_{2,y}}(cos^2\alpha_h - sin^2\alpha_h), \\ B-A =& \left(\frac{1}{2R_{1,y}} - \frac{1}{2R_{1,x}}\right)(cos2\beta_h) + \left(\frac{1}{2R_{2,y}} - \frac{1}{2R_{2,x}}\right)(cos2\alpha_h). \end{aligned} \tag{3.27}$$

By using Equation 3.27, the triangle rule in Equation 3.25 and law of cosines, $B-A$ is obtained as

$$\begin{aligned} B-A = \frac{1}{2}\Bigg(&\left(\frac{1}{R_{1,x}} - \frac{1}{R_{1,y}}\right)^2 + \left(\frac{1}{R_{2,x}} - \frac{1}{R_{2,y}}\right)^2 + \\ & 2\left(\frac{1}{R_{1,x}} - \frac{1}{R_{1,y}}\right)\left(\frac{1}{R_{2,x}} - \frac{1}{R_{2,y}}\right)cos2\psi_h\Bigg)^{1/2}. \end{aligned} \tag{3.28}$$

Geometrical constants for the contact patch are expressed by using Equations 3.26 and 3.28

$$\begin{aligned} A = \frac{1}{4}\Bigg[&\sum_{i=1}^{2}\left(\frac{1}{R_{i,x}} + \frac{1}{R_{i,y}}\right) - \Bigg(\sum_{i=1}^{2}\left(\frac{1}{R_{i,x}} + \frac{1}{R_{i,y}}\right)^2 + \\ & 2\left(\frac{1}{R_{1,x}} - \frac{1}{R_{1,y}}\right)\left(\frac{1}{R_{2,x}} - \frac{1}{R_{2,y}}\right)cos2\psi_h\Bigg)^{1/2}\Bigg], \\ B = \frac{1}{4}\Bigg[&\sum_{i=1}^{2}\left(\frac{1}{R_{i,x}} + \frac{1}{R_{i,y}}\right) + \Bigg(\sum_{i=1}^{2}\left(\frac{1}{R_{i,x}} + \frac{1}{R_{i,y}}\right)^2 + \\ & 2\left(\frac{1}{R_{1,x}} - \frac{1}{R_{1,y}}\right)\left(\frac{1}{R_{2,x}} - \frac{1}{R_{2,y}}\right)cos2\psi_h\Bigg)^{1/2}\Bigg]. \end{aligned} \tag{3.29}$$

From Figure 3.5, indentation and displacements can be expressed by considering the contact shape as

$$\begin{aligned} \delta - z &= u_1 + u_2, \\ \delta - Ax^2 - By^2 &= u_1 + u_2. \end{aligned} \tag{3.30}$$

It is shown in Appendix A of the study by (Shabana et al., 2007) that the pressure p in the contact area produces a displacement

$$u_1 + u_2 = \frac{1-\nu^2}{\pi E}(L - Mx^2 - Ny^2), \tag{3.31}$$

where E is the Young's modulus and ν is the Poisson's ratio of the materials. By considering a combined Young's modulus for the two bodies as

$$\frac{1}{E_{12}} = \frac{1-\nu_1^2}{E_1} + \frac{1-\nu_2^2}{E_2}, \tag{3.32}$$

Equation 3.31 becomes

$$u_1 + u_2 = \frac{L - Mx^2 - Ny^2}{\pi E_{12}}, \tag{3.33}$$

by using Equations 3.33 and 3.30

$$\delta - Ax^2 - By^2 = \frac{L - Mx^2 - Ny^2}{\pi E_{12}}, \tag{3.34}$$

and finally from polynomial equality

$$\delta = \frac{L}{\pi E_{12}} = \frac{p_{z_0} b}{E_{12}} \mathbf{K}_e, \tag{3.35a}$$

$$A = \frac{M}{\pi E_{12}} = \frac{p_{z_0} b}{E_{12} e^2 a^2} (\mathbf{K}_e - \mathbf{E}_e), \tag{3.35b}$$

$$B = \frac{N}{\pi E_{12}} = \frac{p_{z_0} b}{E_{12} e^2 a^2} \left[\left(\frac{a}{b} \right)^2 \mathbf{E}_e - \mathbf{K}_e) \right]. \tag{3.35c}$$

$\mathbf{K}_e$ and $\mathbf{E}_e$ in these equations are the elliptical integrals of first and second kind of the

eccentricity $e = \sqrt{1 - \frac{b^2}{a^2}}$, respectively and definitions of these integrals can be found in Appendix B of the textbook given by (Shabana et al., 2007). p_{z_0} is the maximum pressure in the contact area, a is the contact ellipse semi–length, b is the contact ellipse semi–width. Pressure distribution p in the contact area is semi–ellipsoidal and it is expressed as

$$p = \frac{3F_n}{2\pi ab}\sqrt{1 - \left(\frac{x}{a}\right)^2 - \left(\frac{y}{b}\right)^2}, \tag{3.36}$$

where F_n is the normal force. From Equation 3.36, maximum pressure is given by

$$p_{z_0} = \frac{3F_n}{2\pi ab}. \tag{3.37}$$

Contact ellipse semi–length a, semi–width b, indentation δ and eccentricity e can be found by using the expressions in Equation 3.35 and Equation 3.37. After necessary substitutions of the equations they are defined as

$$a = \sqrt[3]{3\frac{(\mathbf{K}_e - \mathbf{E}_e)}{e^2}\frac{F_n}{2\pi A E_{12}}}, \tag{3.38a}$$

$$b = a\sqrt{1 - e^2}, \tag{3.38b}$$

$$\delta = \mathbf{K}_e\sqrt[3]{\frac{9e^2}{8(\mathbf{K}_e - \mathbf{E}_e)}\frac{F_n^2 2A}{\pi^2}}, \tag{3.38c}$$

$$e = \sqrt{1 - \frac{b^2}{a^2}} = \sqrt{1 - \frac{A}{B}\frac{\mathbf{E}_e - (1 - e^2)\mathbf{K}_e}{\mathbf{K}_e - \mathbf{E}_e}}. \tag{3.38d}$$

Series expansion around the point $e = 0$ for elliptical integrals of first and second kind are computed as presented by (Vatankhah, 2011)

$$\mathbf{K}_e = \frac{\pi}{2}\left[1 + \left(\frac{1}{2}\right)^2 e^2 + \left(\frac{1 \times 3}{2 \times 4}\right)^2 e^4 + \cdots + \left(\frac{(2n-1)!!}{(2^n \times n!)}\right)^2 e^{2n} + \ldots\right], \tag{3.39a}$$

$$\mathbf{E}_e = \frac{\pi}{2}\left[1 - \left(\frac{1}{2^2}\right) e^2 - \left(\frac{1^2 \times 3}{2^2 \times 4^2}\right) e^4 - \cdots - \left(\frac{(2n-1)!!}{(2^n \times n!)}\right)^2 \frac{e^{2n}}{2n-1} + \ldots\right]. \tag{3.39b}$$

In these equations n represents the number of terms to approximate elliptical integrals.

A more appropriate calculation model is presented by (Michálek, 2008) as

$$\mathbf{K}_e = \sum_{n=1}^{\infty} P_n, where : P_{n+1} = P_n \left(\frac{2n-1}{2n}\right)^2 e^2, \tag{3.40a}$$

$$\mathbf{E}_e = \sum_{n=1}^{\infty} P_n, where : P_{n+1} = P_n \left(\frac{2n-1}{2n}\right)^2 e^2 \left(\frac{2n-3}{2n-1}\right). \tag{3.40b}$$

In both cases of the calculation of elliptical integrals, P_1 is considered as 2π. In each iteration e must be calculated. The initial value for the calculation of e is taken as 0.5 and the maximum iteration number is considered as 10^3. It is stated by (Vatankhah, 2011) that if e is taken between $0 \leq e \leq 0.99$ and considering just the four terms of the series for practical application, maximum percentage errors of expressions in Equations 3.39 and 3.40 are 30% and 6% for $\mathbf{K}_e$ and $\mathbf{E}_e$, respectively. For the range $0 \leq e \leq 0.8$, these errors reduces to 2% and 0.4%. In this dissertation, if the highest term is smaller than a threshold (e.g. 10^{-3}), iterations are terminated regardless of the iteration count. Therefore, more efficient and accurate calculation of elliptical integrals can be obtained. The value of eccentricity is needed for given geometrical parameters A and B in each calculation by using the Equation 3.38d.

3.2.2 Virtual Penetration Method and The Correction of Shape of the Area

Linder's method, which is cited by (Sichani et al., 2014), is considered in some applications of the dissertation.

In order to determine the contact, displacements in the surface are neglected in this approach. Assumption is that bodies can penetrate each other. Observations show that a smaller value of interpenetration leads to a contact shape closer to the real contact shape. Such a virtual penetration value is based the observations and it is determined as $\delta_0 = 0.55\delta$ by Linder and (Piotrowski and Kik, 2008). This value is compared by (Piotrowski and Kik, 2008) with the results of the well–known contact solution program CONTACT by Kalker and results are in good agreement. By considering the Equation

3.30 without displacement, it can be expressed as

$$\begin{aligned} \delta - Ax^2 - By^2 = 0, \\ \delta = Ax^2 + By^2. \end{aligned} \tag{3.41}$$

Using the proposed virtual penetration for the previous equation, indentation is defined as

$$\delta_0 = Ax^2 + By^2. \tag{3.42}$$

In case of Hertzian contact, solution is given by an ellipse. By using the Linder's method, the scaled Hertzian contact dimensions are expressed as

$$\begin{aligned} a = \sqrt{\frac{0.55\delta}{A}}, \\ b = \sqrt{\frac{0.55\delta}{B}}. \end{aligned} \tag{3.43}$$

3.3 Solution of the Tangential Problem

3.3.1 Creepage Definition

As previously indicated, a very first investigation on the motion of the wheelset is that the wheels do not have a *pure rolling* motion. Instead, experiments show that the motion of the wheels consists of *rolling* and *sliding* motion. Due to this effect, the circumferential and translational velocity of the vehicle is different. The difference between these two velocities is called *creepage* and forces occurring in the contact area due to this phenomenon are called *creep forces*. Ayasse and Chollet (Iwnicki, 2006) express the mathematical definitions of the creepages in quasi–static situation w.r.t the projected speeds, and the definitions are given in Equation 3.44 and illustrated in Figure 3.7.

$$\xi_x = \frac{proj(x)(V_w - Vr)}{\frac{1}{2}(V_w + Vr)}, \tag{3.44a}$$

$$\xi_y = \frac{proj(y)(V_w - Vr)}{\frac{1}{2}(V_w + Vr)}, \tag{3.44b}$$

$$\xi_s = \frac{proj(z)(\omega_w - \omega r)}{\frac{1}{2}(V_w + Vr)} \tag{3.44c}$$

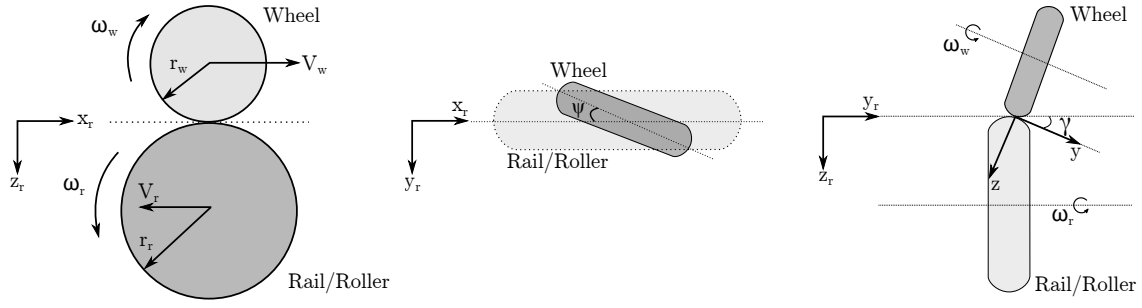

Figure 3.7: Creepage definition according to geometries

3.3.2 Kalker's Linear Theory

The theory of Hertz does not consider the surface shear tractions (i.e. tangential tractions) p_x and p_y which are important to determine the tangential forces. Tangential tractions exist in the contact area of the two bodies which are interacted. In the contact area, these tractions are given by the well–known Columb's law as

$$\begin{cases} V_{wr} & = 0; |p_x, p_y| \leq \mu\sigma_z;\ adhesion\ area \\ V_{wr} & \neq 0; (p_x, p_y) = \mu\sigma_z \frac{V_{wr}}{|V_{wr}|};\ slip\ area \end{cases} \tag{3.45}$$

where V_{wr} velocity of wheel on rail (or roller), μ is the friction coefficient and σ_z is the normal pressure in the contact. As stated by (Kalker, 1973), if the position of a particle, which is inside the contact area, is assumed as (x, y, z) before deformation and then it is $(x + u_x, y + u_y, z + u_z)$. Hereby, u with indices represent the elastic deformations in the related directions. By using the continuum mechanics, the Euler equation for this particle, (Kalker, 1973, 1967), is expressed as

$$\mathbf{V_{par}} = \mathbf{V_{par,uns}} + \frac{\partial \mathbf{u}}{\partial t} + \mathbf{V_{par,uns}}.\nabla \mathbf{u}, \tag{3.46}$$

where $\mathbf{V_{par}}$ and $\mathbf{V_{par,uns}}$ are the velocities of the particle in deformed and unstressed states, respectively. ∇ indicates the gradient. By considering this equation, the slip between two bodies are defined as

$$\begin{aligned}\mathbf{v_s} = \mathbf{V_w} - \mathbf{V_r} =&(\mathbf{V^w_{par,uns}} - \mathbf{V^r_{par,uns}}) + \frac{\partial(\mathbf{u_w} - \mathbf{u_r})}{\partial t} + \\ &\frac{1}{2}(\mathbf{V^w_{par,uns}} - \mathbf{V^r_{par,uns}}).\nabla(\mathbf{u_w} + \mathbf{u_r}) + \\ &\frac{1}{2}(\mathbf{V^w_{par,uns}} + \mathbf{V^r_{par,uns}}).\nabla(\mathbf{u_w} - \mathbf{u_r}).\end{aligned} \tag{3.47}$$

The assumption in this equation is that the displacement gradients are small and the third term in the right–hand side can be neglected compared to first term. If it is assumed that the rolling direction approximately coincides with the axis in the centre of the contact patch, for example x–axis, material will flow in the negative direction with a velocity equal to the rolling velocity, (Kalker, 1973). Therefore, $\frac{1}{2}(\mathbf{V^w_{par,uns}} + \mathbf{V^r_{par,uns}})$ can be expressed as the negative of rolling velocity. Additionally, since displacement gradients are small, fourth term in the Equation 3.47 can be taken as the rolling velocity. The firt term (velocity difference in unstressed states) can be regarded as translations and rotations and they are given by

$$\mathbf{V^w_{par,uns}} - \mathbf{V^r_{par,uns}} = V(\xi_x - \xi_s y, \xi_y + \xi_s x), \tag{3.48}$$

where ξ_x and ξ_y are the creepages, ξ_s is the spin. $(\mathbf{u_r} - \mathbf{u_w}) = (u_x, u_y, u_z)$ is the displacement difference and substituting all the assumptions and derivations to the Equation 3.47 leads to

$$\begin{aligned}\mathbf{V_w} - \mathbf{V_r} = \Bigg(&V\xi_x - V\xi_s y - \frac{\partial u_x}{\partial t} + V\frac{\partial u_x}{\partial x}, \\ &V\xi_y + V\xi_s x - \frac{\partial u_y}{\partial t} + V\frac{\partial u_y}{\partial x}\Bigg),\end{aligned} \tag{3.49}$$

where z component is neglected due to contact between bodies. Relative slip can be

written as

$$(s_x, s_y) = \frac{\mathbf{V_w} - \mathbf{V_r}}{V} = \left(\xi_x - \xi_s y - \frac{1}{V}\frac{\partial u_x}{\partial t} + \frac{\partial u_x}{\partial x}, \right. \\ \left. \xi_y + \xi_s x - \frac{1}{V}\frac{\partial u_y}{\partial t} + \frac{\partial u_y}{\partial x}\right). \tag{3.50}$$

In steady state rolling, the displacement is independent on time. Therefore, relative slip is given by

$$(s_x, s_y) = \left(\xi_x - \xi_s y + \frac{\partial u_x}{\partial x}, \xi_y + \xi_s x + \frac{\partial u_y}{\partial x}\right). \tag{3.51}$$

If a simple relationship between displacement and traction are considered as presented by (Kalker, 1973), these relationships are defined by

$$u_x = L_x p_x, \tag{3.52a}$$

$$u_y = L_y p_y, \tag{3.52b}$$

where L_x and L_y are the flexibility parameters. By considering identical material assumption and expressions in Equations 3.51 and 3.52, and by using the fact that slip is zero in the adhesion area, the proceeding expression is written as

$$\begin{aligned} 0 =& \xi_x - \xi_s y + L_x \frac{\partial p_x}{\partial x}, \\ 0 =& \xi_y + \xi_s x + L_y \frac{\partial p_y}{\partial x}. \end{aligned} \tag{3.53}$$

In the linearised theory, the slip condition in Equation 3.45 is neglected. From Equation 3.53 tractions are obtained as

$$\begin{aligned} \frac{\partial p_x}{\partial x} =& -\left(\frac{1}{L_x}\right)(\xi_x - \xi_s y), \\ \frac{\partial p_y}{\partial x} =& -\left(\frac{1}{L_y}\right)(\xi_y - \xi_s x), \end{aligned} \tag{3.54}$$

by integration

$$\begin{aligned} p_x &= -\left(\frac{1}{L_x}\right)(\xi_x - \xi_s y)x + f(y), \\ p_y &= -\left(\frac{1}{L_y}\right)\left(\xi_y - \frac{1}{2}\xi_s x\right)x + g(y), \end{aligned} \tag{3.55}$$

and arbitrary functions $f(y)$ and $g(y)$ are determined as follows, (Kalker, 1973). At the leading edge particles do not carry any traction. According to the no slip condition, creepage and spin do not vanish and traction increases. As soon as particles leave the contact, traction falls to zero. By using this fact, tractions are given by

$$\begin{aligned} p_x &= -\left(\frac{1}{L_x}\right)(\xi_x - \xi_s y)(\bar{a} - x), \\ p_y &= -\left(\frac{1}{L_y}\right)\left[\xi_y(\bar{a} - x) - \frac{1}{2}\xi_s(\bar{a}^2 - x^2)\right], \end{aligned} \tag{3.56}$$

where $\bar{a} = a\sqrt{1 - \frac{y^2}{b^2}}$ is the x coordinate of the leading edge. By integrating tractions in the contact area, creep force components and creep moment are obtained as

$$F_x = \iint_C p_x dxdy = \frac{8a^2 b\xi_x}{3L_x} = Gabc_{11}\xi_x, \tag{3.57a}$$

$$F_y = \iint_C p_y dxdy = \frac{8a^2 b\xi_y}{3L_y} + \frac{\pi a^3 b\xi_s}{4L_x} = Gab\left[c_{22}\xi_y + \sqrt{ab}c_{23}\xi_s\right], \tag{3.57b}$$

$$\begin{aligned} M_z &= \iint_C (xp_y - yp_x)\, dxdy = \frac{-\pi a^3 b\xi_y}{4L_y} + \frac{8a^2 b^3 \xi_s}{15L_x} \\ &= G(ab)^{3/2}\left[c_{32}\xi_y + \sqrt{ab}c_{33}\xi_s\right], \end{aligned} \tag{3.57c}$$

where c_{ij} $i, j = 1, 2, 3$ are the creepage and spin coefficients and G is the modulus of rigidity. c_{ij} are also called as Kalker coefficients which are calculated with the exact theory proposed by (Kalker, 1979). These coefficients are also tabulated by Kalker w.r.t. $\frac{b}{a}$ and Poisson's ratio. Polynomial functions are consiered to calculate approximate values of these coefficients in the table. These functions are given in Appendix A. In this dissertation, this theory is used for the calculations of creep moments.

3.3.3 Fastsim

Fastsim is an algorithm proposed by (Kalker, 1982) which is based on the simplified theory. In the simplified theory, the relationship between traction and surface displacement in the general form are given by

$$\mathbf{u} = L\mathbf{p}, \tag{3.58}$$

where $\mathbf{u} = \begin{bmatrix} u_x & u_y & u_z \end{bmatrix}$ is the deformation vector, $\mathbf{p} = \begin{bmatrix} p_x & p_y & p_z \end{bmatrix}$ is the traction vector and L is the flexibility parameter. Flexibility components can be found by using the results of the linear theory. In order to find flexibility parameters in different directions, Equation 3.57 is used and these parameters are obtained as

$$L_x = \frac{8a}{3Gc_{11}}, L_y = \frac{8a}{3Gc_{22}}, L_\phi = \frac{\pi a^2}{4Gc_{23}\sqrt{ab}}, \tag{3.59}$$

where components of these expressions are explained in the previous section. Besides, a weighted mean of the flexibilities can be used for calculations as stated by (Kalker, 1991; Vollebregt and Wilders, 2011)

$$L = \frac{|\xi_x|L_x + |\xi_y|L_y + |\xi_s|L_\phi}{\sqrt{\xi_x^2 + \xi_y^2 + \xi_s^2 ab}}. \tag{3.60}$$

However, the use of weighted mean of flexibilities causes differences from the results of the exact theory.

In this algorithm, it is assumed that the normal problem is solved and the contact patch dimensions are present. In this work, elliptical contact patch is assumed and normal surface tractions (i.e. pressure distribution) are given as semi–ellipsoidal in Equation 3.36. Furthermore, as stated by (Vollebregt and Wilders, 2011), semi–ellipsoidal traction bound prevents slip at the leading edge of the contact area. Therefore, a parabolic traction bound is an alternative and given by

$$p = \frac{2F_n}{\pi ab}\left(1 - \left(\frac{x}{a}\right)^2 - \left(\frac{y}{b}\right)^2\right). \tag{3.61}$$

A representation of the algorithm can be found in Algorithm 1. Briefly, first step is the discretization of the contact patch. Then, rigid slips and traction are calculated for each point and tractions in longitudinal and lateral directions are checked whether they are smaller than the traction bound. If they are bigger than traction bound, they are equated to the traction bound. The last step is the approximation of the integration

$$\mathbf{F} = \int_{-b}^{b} \int_{-a_y}^{a_y} \mathbf{p}(x, y) dx dy. \tag{3.62}$$

3.3.4 Heuristic Nonlinear Creep Force Model

The problem in linear theory is that it does not consider a saturation law as expressed by (Shen et al., 1983). A heuristic creep force model based on the cubic saturation law is provided by (Vermeulen and Johnson, 1964). This law is presented as

$$\begin{aligned} F_{x_{NL}} &= F_x \epsilon_{sat}, \\ F_{y_{NL}} &= F_y \epsilon_{sat}, \\ M_{z_{NL}} &= M_z \epsilon_{sat}, \end{aligned} \tag{3.63}$$

where ϵ_{sat} is the creep force reduction coefficient and defined as

$$\epsilon_{sat} = \begin{cases} \dfrac{\mu F_n}{F_{Res}} \left[\dfrac{F_{Res}}{\mu F_n} - \dfrac{1}{3} \left(\dfrac{F_{Res}}{\mu F_n} \right)^2 + \dfrac{1}{27} \left(\dfrac{F_{Res}}{\mu F_n} \right)^3 \right] & F_{Res} < 3\mu F_n, \\ \dfrac{\mu F_n}{F_{Res}} & F_{Res} > 3\mu F_n, \end{cases} \tag{3.64}$$

where $F_{Res} = \sqrt{F_x^2 + F_y^2}$ is the resultant creep force. In this dissertation, this theory is used for correcting creep moments with a saturation law.

3.3.5 Polach's Nonlinear Creep Force Model

(Polach, 2000) considers the elliptical contact patch and normal pressure distribution. The creep force model proposed by (Polach, 2000) presents that tangential

Algorithm 1 Fastsim algorithm

procedure FASTSIM(a, b)
  $d_y \leftarrow \frac{2b}{n_y}$ ▷ n_y:y axis discretization
  $F_x \leftarrow 0$ ▷ Longitudinal Creep Force
  $F_y \leftarrow 0$ ▷ Lateral Creep Force
  $L_x \leftarrow \frac{8a}{3Gc_{11}}$ ▷ Longitudinal Flexibility
  $L_y \leftarrow \frac{8a}{3Gc_{22}}$ ▷ Lateral Flexibility
  $L_\phi \leftarrow \frac{\pi a^2}{4Gc_{23}\sqrt{ab}}$ ▷ Spin Flexibility
  for $j \leftarrow 1, n_y$ **do**
    $y \leftarrow -b + (j - 1/2)d_y$
    $a_y \leftarrow a\sqrt{1 - \left(\frac{y}{b}\right)^2}$ ▷ Boundary on the x axis
    $d_x \leftarrow \frac{2a_y}{n_x}$ ▷ n_x:x axis discretization
    $p_x \leftarrow 0$ ▷ Longitudinal Traction
    $p_y \leftarrow 0$ ▷ Lateral Traction
    for $i \leftarrow 1, n_x$ **do**
      $x \leftarrow a_y - (i - 1/2)d_x$
      $w_x \leftarrow \frac{\xi_x}{L_x} - \frac{y\xi_\phi}{L_\phi}$ ▷ Longitudinal Rigid Slip
      $w_y \leftarrow \frac{\xi_y}{L_y} + \frac{x\xi_\phi}{L_\phi}$ ▷ Lateral Rigid Slip
      $p_z \leftarrow \frac{2N}{\pi ab}\left(1 - \frac{x^2}{a^2} - \frac{y^2}{b^2}\right)$ ▷ Pressure Distribution
      $p_{N_x} \leftarrow p_x - d_x \times w_x$ ▷ x– Traction
      $p_{N_y} \leftarrow p_y - d_y \times w_y$ ▷ y– Traction
      $p_N \leftarrow \sqrt{p_{N_x}^2 + p_{N_y}^2}$ ▷ Total– Traction
      if $|p_N| \leq \mu \times p_z$ **then** ▷ Traction Bound Control
        $p_x \leftarrow p_{N_x}$
        $p_y \leftarrow p_{N_y}$
      else
        $p_x \leftarrow \mu \times p_z \times \left(\frac{p_{N_x}}{|p_N|}\right)$
        $p_y \leftarrow \mu \times p_z \times \left(\frac{p_{N_y}}{|p_N|}\right)$
      end if
    end for
  end for
  $F_x \leftarrow F_x + p_x \times d_x \times d_y$;
  $F_y \leftarrow F_y + p_y \times d_x \times d_y$;
  return F_x, F_y ▷ Creep Forces
end procedure

stress increases with increasing creepage similar to Kalker's linear theory. However, in this creep force model, tangential stresses are limited by friction coefficient and normal pressure. After this limit is reached, a relative motion between two surfaces occurs and the

part of contact patch related with this motion is called slip area. It can be seen in Figure 3.8. In general form, tangential force is obtained by using Equation 3.62. Tangential force components are given by

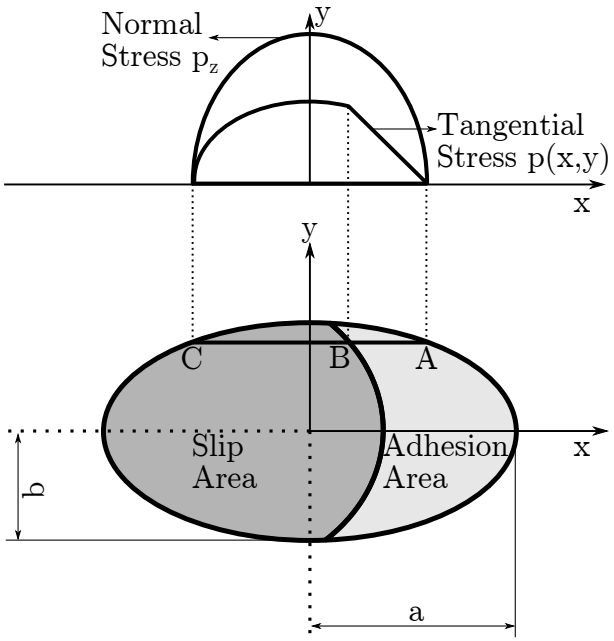

Figure 3.8: Stress distribution and the part of contact patch adapted from (Polach, 2000)

$$F_i = F\frac{s_i}{s}, \quad i = x, y \tag{3.65}$$

where $s = \sqrt{s_x^2 + s_y^2}$ is the total slip. (Polach, 2000) reports that (Freibauer, 1983) solved the integration by using a transformation of the tangential stress distribution from ellipsoid to hemisphere and this transformation is defined as

$$\begin{aligned} y^* &= \frac{a}{b}y, \\ \mathbf{p}^* &= \frac{a}{p_0}\mathbf{p}, \end{aligned} \tag{3.66}$$

where $y*$ and $\mathbf{p}*$ are transformed variables. (Polach, 2000) uses a proportionality constant C, which represents the elasticity of contact (i.e. reciprocal of tangential contact stiffness).

The gradient of tangential stress in the area of adhesion is given by (Polach, 2000) as

$$\epsilon = \frac{2}{3}\frac{C\pi a^2 b}{F_n \mu}s. \tag{3.67}$$

The tangential force is found by solving the integral given in Equation 3.62 with transformed variables as

$$\mathbf{F} = p_0 \frac{b}{a^2}\int_{-b}^{b}\int_{-a}^{a}\mathbf{p}^*(x,y)dxdy^* = -p_0\frac{b}{a^2}\frac{4}{3}a^3\left(\frac{\epsilon}{1+\epsilon^2}+\arctan\epsilon\right), \tag{3.68}$$

where the components of the force can be found by using Equation 3.63.

Spin has an observable effect on the creep force. Simply, spin is the rotation about the vertical axis due to the wheel conicity. For a wheel relative spin can be given as

$$\xi_s = \frac{\omega.\sin\gamma_p}{V_w} = \frac{\sin\gamma_p}{r_w}, \tag{3.69}$$

where r_w is the rolling radius of the wheel and other parameters are previously explained. Longitudinal component of the creep force vanishes at pure spin. In this case, the centre of rotation is the origin of the contact patch with the assumption that semi–axis a is too small. Using the same transformation used by Freibauer in Equation 3.66, lateral force due to pure spin is calculated as

$$F_y = p_0\frac{b}{a^2}\int_{-b}^{b}\int_{-a}^{a}p_y^* dxdy^* = -\frac{3}{8}\pi p_0 ab\left[|\epsilon|\left(\frac{\delta_p^3}{3}-\frac{\delta_p^2}{2}+\frac{1}{6}\right)-\frac{1}{3}\sqrt{\left(1-\delta_p^2\right)^3}\right], \tag{3.70}$$

where δ_p is

$$\delta_p = \frac{\epsilon^2-1}{\epsilon^2+1}. \tag{3.71}$$

By considering Equation 3.37, Equation 3.70 can be rewritten as

$$F_y = -\frac{9}{16} F_n \mu K_M, \tag{3.72}$$

and K_M is

$$K_M = |\epsilon| \left(\frac{\delta_p^3}{3} - \frac{\delta_p^2}{2} + \frac{1}{6} \right) - \frac{1}{3} \sqrt{\left(1 - \delta_p^2\right)^3}. \tag{3.73}$$

(Polach, 2000) states that for increasing semi–axis ratio $\frac{a}{b}$ the effect of the spin also increases. In this case, the assumption, which semi–axis a is too small, fails. Therefore, forces due to the longitudinal and lateral creepages, and lateral force due to the spin are calculated separately. Instead of the slip s, corrected resulting slip $s_C = \sqrt{s_x^2 + s_{y_C}^2}$ should be considered in previous equations. s_{y_C} is the corrected lateral slip due to the spin and given by

$$s_{y_C} = s_y + \xi_s.a \qquad for \quad |s_y + \xi_s.a| > |s_y| \tag{3.74a}$$

$$s_{y_C} = s_y \qquad for \quad |s_y + \xi_s.a| \leq |s_y|. \tag{3.74b}$$

Corrected lateral force which includes an increase due to the spin is defined as

$$F_{y_C} = F_y + F_{y_S}. \tag{3.75}$$

(Polach, 2000) derives the equations by considering the Kalker's linear theory which is presented in Equation 3.57. Total force in the proposed method is in the form

$$\mathbf{F} = -\frac{8}{3} a^2.b.C.s, \tag{3.76}$$

and the total force according to the Kalker's linear theory is

$$\mathbf{F} = -G.a.b.c_{jj}.s. \tag{3.77}$$

By using the analogy between Equation 3.76 and Equation 3.77, contact stiffness C can be obtained easily. c_{jj} is expressed as

$$c_{jj} = \sqrt{\left(c_{11}\frac{s_x}{s}\right)^2 + \left(c_{22}\frac{s_y}{s}\right)^2}. \tag{3.78}$$

Similar to the comparison of the proposed method with the Kalker's linear theory, a comparison can be carried out for the increase in tangential force due to spin as

$$F_{y_S} = -\frac{1}{4}\pi.a^3.b.C_s.\xi_s, \tag{3.79a}$$

$$F_{y_S} = -G.c_{23}.\xi_s.\sqrt{(a.b)^3}. \tag{3.79b}$$

The first equation in Equation 3.79 represents the calculation of increase in lateral tangential force due to the spin by proposed method and the second one represents the calculation by using Kalker's linear theory. C_s is defined as the tangential contact stiffness for the spin. The gradient of tangential stress ϵ_{sp} for the calculation of increase in lateral tangential force is expressed as

$$\epsilon_{sp} = \frac{8}{3}\frac{G.b.\sqrt{a.b}}{F_n.\mu}\frac{c_{23}.s_{y_C}}{1 + 6.3\left[1 - exp\left(-\frac{a}{b}\right)\right]}, \tag{3.80}$$

and the increase in lateral tangential force due to the spin is given by

$$F_{y_S} = -\frac{9}{16}a.F_n.\mu.K_M\left[1 + 6.3\left(1 - exp\left(-\frac{a}{b}\right)\right)\right]\frac{\xi_s}{s_C}. \tag{3.81}$$

In Equation 3.81, K_M is calculated by using the gradient definition given in Equation 3.80. Then, Polach extends this creep force model for large creep applications. As well as extension of creep force model, (Polach, 2005) considers a variable friction coefficient dependent on the slip velocity. (Polach, 2005) reports that increasing creep increases the temperature in the contact and this causes a decrease in the friction coefficient. This

friction coefficient is defined by

$$\mu = \mu_0 \left[(1 - A)exp(-Bw) + A\right], \tag{3.82}$$

where $A = \dfrac{\mu_\infty}{\mu_0}$ is the ratio of limit friction coefficient μ_∞ at infinite slip to maximum friction coefficient μ_0, B is the coefficient of exponential friction decrease (s/m), $w = s.V_w$ is the slip velocity.

(Polach, 2005) explains that in case of wet or polluted contact conditions, adhesion optimum can be obtained by reducing the coefficients from Kalker's linear theory. However, measurements show that such reduction in Kalker coefficients do not represent real conditions. Therefore, (Polach, 2005) extends the creep force model for several contact conditions. This extension is based on modelling the creep forces for combination of dry, wet or polluted contact conditions. In wet or polluted contact conditions, due to a third layer in the contact, the slip area increases in the contact patch. As a result, the initial gradient of the creep force w.r.t. the slip increases. In order to model this effect, (Polach, 2005) proposes different reduction factors k_A in the adhesion area and k_S in the area of slip. Thus, the result of Equation 3.68 can be rewritten in the form

$$\mathbf{F} = -\frac{2F_n\mu}{\pi}\left(\frac{k_A\epsilon}{1 + (k_A\epsilon)^2} + \arctan k_S\epsilon\right), \quad k_S \leq k_A \leq 1. \tag{3.83}$$

(Polach, 2005) also states that the reduction of Kalker's coefficient at the origin is given by

$$k = \frac{k_A + k_S}{2}. \tag{3.84}$$

3.4 Track Irregularities

In this doctoral study, one of the main objectives is to use estimation of parameters and states by considering the dynamic response of the wheelset due to the track irregularities. In order to be consistent with the real situation, instead of randomly generated step inputs for track irregularity, measurements taken from a track section (3 km length) between Choceň-Dobřikov, Czech Republic are considered. Data is provided

by DFJP, UPCE.

The details of how track irregularities are measured w.r.t. the related standards are given by (Karis, 2009). In estimation of friction coefficient as a parameter, the lateral (alignment) track irregularities are used since only lateral and yaw dynamics are considered. Lateral alignment can be derived from the lateral shift of the rails as stated in Chapter 14 of textbook by (Iwnicki, 2006)

$$y_{irr} = \frac{y_{irr_L} + y_{irr_R}}{2}, \tag{3.85}$$

An illustration of the considered irregularities are given in Figure 3.9. Similar to the work by (Pombo et al., 2007), track irregularities are also parametrized by using shape preserving cubic splines with respect to the track length. The statistical characteristics of the lateral alignment, vertical track irregularities for right and left rails can be found in Table 3.1, 3.2 and 3.3, respectively.

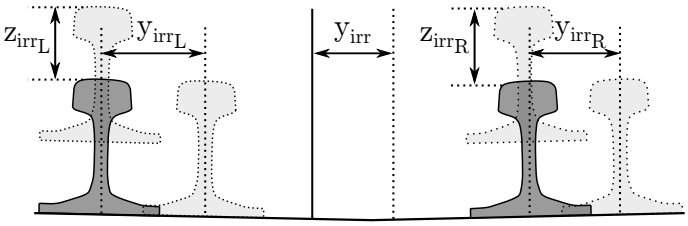

Figure 3.9: Vertical and lateral rail irregularities

Table 3.1: Lateral track irregularity statistical characteristics

Maximum irregularity (mm)	Minimum irregularity (mm)	Standard deviation (mm)	Variance (mm^2)
3.8 mm	-3.3541 mm	0.8103 mm	0.9002 mm^2

Table 3.2: Right rail vertical irregularity of statistical characteristics

Maximum irregularity (mm)	Minimum irregularity (mm)	Standard deviation (mm)	Variance (mm^2)
7.3851 mm	-4.8160 mm	1.1022 mm	1.2149 mm^2

Especially, findings given in Table 3.1 show that the lateral alignment irregularities do not have such a magnitude which can cause a flange contact with the assumption of

Table 3.3: Left rail vertical irregularity of statistical characteristics

Maximum irregularity (mm)	Minimum irregularity (mm)	Standard deviation (mm)	Variance (mm^2)
6.62 mm	-4.35 mm	0.9731 mm	0.9469 mm^2

straight track. As illustrated in Figure 4.9, a flange contact occurs around 6 mm lateral shift of a wheelset. Thus, there is no need to consider complex models for flange contact, which occurs generally in case of negotiating curves, switches and turnouts as stated by (Burgelman et al., 2014).

3.5 Dynamic Models for Estimation Purposes

3.5.1 Equations of Motion of a Wheelset on Straight Track

Wheelset is a crucial part in the dynamic analysis of railway vehicles. Besides, it is the only component which interacts with the rails (or rollers for experimental case). The so called plan view dynamics of the wheelset, which is presented by (Garg and Dukkipati, 1984), is considered.

3.5.1.1 Kinematics

Three coordinate system is used in the dynamic analysis of the wheelset and these axes can be seen in Figure 3.10. Equilibrium coordinate system x_{eq}, y_{eq}, z_{eq} has an origin on the centreline of the track and has a constant velocity of V_w with respect to fixed inertial frame. $x_{int}, y_{int}, z_{int}$ is the intermediate frame and it is obtained by rotating the equilibrium axes with an angle ψ around z_{eq}. x_w, y_w, z_w is the wheelset axes which are located in the centre of mass of the wheelset. Additionally, two sets of coordinate systems are assigned for each contact point. x_{Lc}, y_{Lc}, z_{Lc} and x_{Rc}, y_{Rc}, z_{Rc} are the axes for the left and right contact points, respectively. These axes can be seen in Figure 3.11. In Figure 3.11, δ_L and δ_R are the contact angles of the left and right wheel, r_L and r_R are the left and right rolling radii, respectively. Transformation matrices between these coordinate systems can be found in Appendix B.

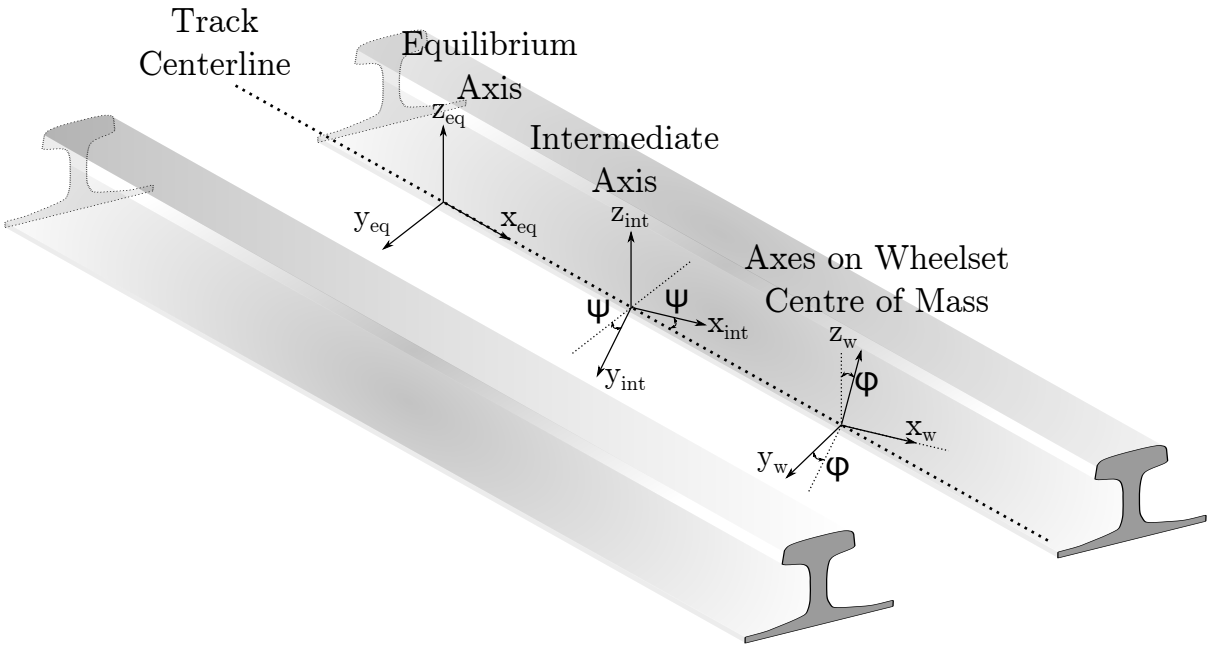

Figure 3.10: Coordinate systems which are considered in the dynamic analysis of a wheelset, figure is adapted from (Garg and Dukkipati, 1984)

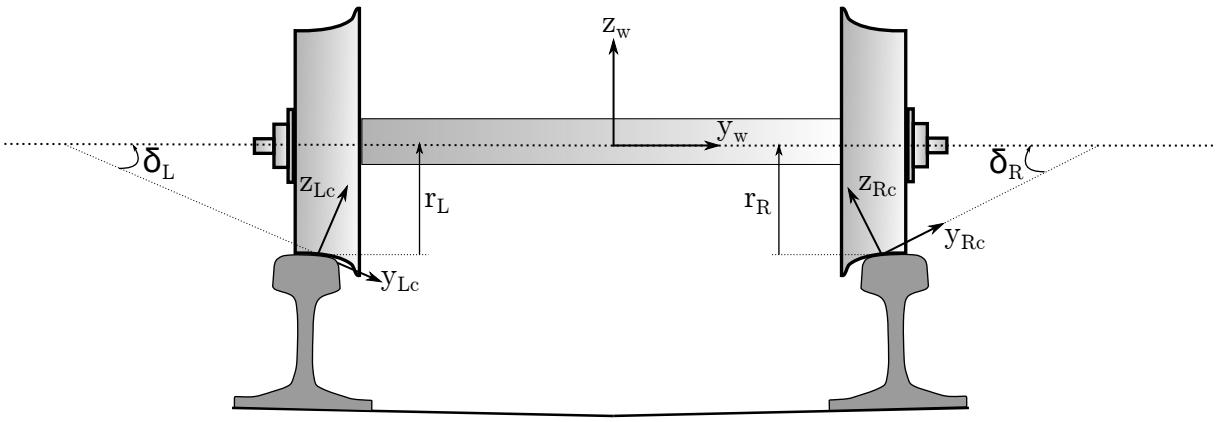

Figure 3.11: Coordinate systems for contact points, figure is adapted from (Garg and Dukkipati, 1984)

3.5.1.2 General Dynamic Equations of a Wheelset, Lateral and Yaw Dynamics

General equations of motion of the wheelset are derived in equilibrium axes. Angular velocity $\boldsymbol{\omega}_w$ of the wheelset can be expressed in the wheelset axes as

$$\boldsymbol{\omega}_w = \omega_{w_x}\mathbf{i}_w + \omega_{w_y}\mathbf{j}_w + \omega_{w_z}\mathbf{k}_w, \tag{3.86}$$

where $\boldsymbol{\omega}_w$ is the angular velocity vector of the wheelset, $\mathbf{i}_w, \mathbf{j}_w, \mathbf{k}_w$ are the unit vectors in wheelset axes. Angular velocity components of the wheelset can be represented by using the motions in the direction of degrees of freedom where $\omega_{w_x} = \dot{\phi}$, $\omega_{w_y} = \Omega + \dot{\beta} + \dot{\psi}\sin\phi$, and $\omega_{w_z} = \dot{\psi}\cos\phi$. ϕ is the roll displacement of the wheelset, ψ is the yaw displacement of the wheelset and β is the angular perturbation from nominal angular velocity $\Omega = \frac{V_w}{r_0}$ of wheelset. Furthermore, the angular velocity of the wheelset can be given in wheelset axes as

$$\mathbf{H} = I_{w_x}\omega_{w_x}\mathbf{i}_w + I_{w_y}\omega_{w_y}\mathbf{j}_w + I_{w_z}\omega_{w_z}\mathbf{k}_w, \tag{3.87}$$

where $I_{w_x}, I_{w_y}, I_{w_z}$ are the moments of inertia of the wheelset. Due to the symmetry, $I_{w_x} = I_{w_z}$ is assumed. Angular velocity of the body coordinate systems (i.e. intermediate axes and wheelset axes) can be expressed as

$$\boldsymbol{\omega}_{axis} = \dot{\phi}\mathbf{i}_\mathbf{w} + \dot{\psi}\mathbf{k}_\mathbf{int} = \dot{\phi}\mathbf{i}_w + \dot{\psi}\sin\phi\mathbf{j}_w + \dot{\psi}\cos\phi\mathbf{k}_w. \tag{3.88}$$

The rate of change of momentum can be given as

$$\frac{d\mathbf{H}}{dt} = I_{w_x}\dot{\omega}_{w_x}\mathbf{i}_w + I_{w_y}\dot{\omega}_{w_y}\mathbf{j}_w + I_{w_z}\dot{\omega}_{w_z}\mathbf{k}_w + \boldsymbol{\omega}_{axis}\times\mathbf{H}, \tag{3.89}$$

after substituting Equation 3.87 and 3.88 into Equation 3.89, and transforming the equations into equilibrium axes by using the transformation matrices given in Appendix B with small ϕ, ψ angles assumption, rate of change of momentum can be rewritten as

$$\frac{d\mathbf{H}}{dt} = \left(I_{w_x}\ddot{\phi} - I_{w_y}\Omega\dot{\psi}\right)\mathbf{i}_{eq} + I_{w_y}\ddot{\beta}\mathbf{j}_{eq} + \left(I_{w_x}\ddot{\psi} + I_{w_y}\Omega\dot{\phi}\right)\mathbf{k}_{eq}. \tag{3.90}$$

In general form, the equations of motion are expressed in the equilibrium axes as

$$m_w\ddot{\mathbf{r}} = \sum\mathbf{F}, \tag{3.91a}$$

$$\frac{d\mathbf{H}}{dt} = \sum\mathbf{M}, \tag{3.91b}$$

where m_w is the mass of the wheelset and $\mathbf{r}$ is the position vector. The forces acting on the wheelset is shown in Figure 3.12 and connections between wheelset and bogie frame are illustrated in Figure 3.13. In these free body diagram, F_L and F_R are the creep forces at the left and right contact points, M_L and M_R are the left and right creep moments, N_L and N_R are the left and right normal forces at contact points, $\mathbf{F}_S$ and $\mathbf{M}_S$ are the suspension forces and moments, respectively. W_w is the weight of the wheelset.

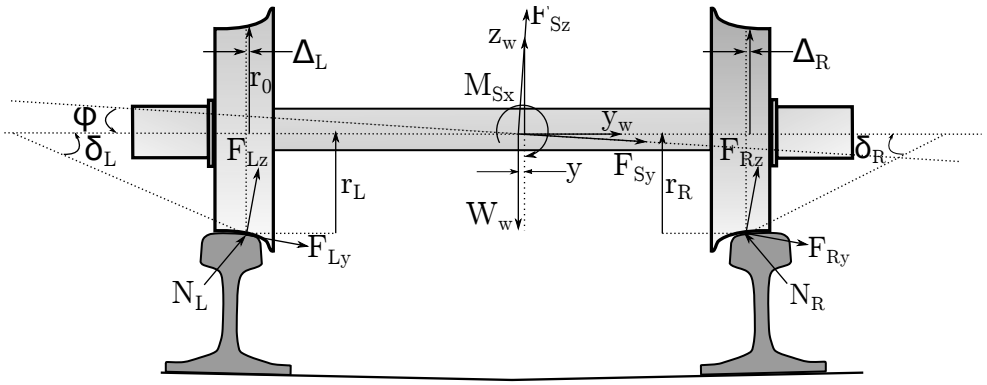

Figure 3.12: Free body diagram of the wheelset, figure is adapted from (Garg and Dukkipati, 1984)

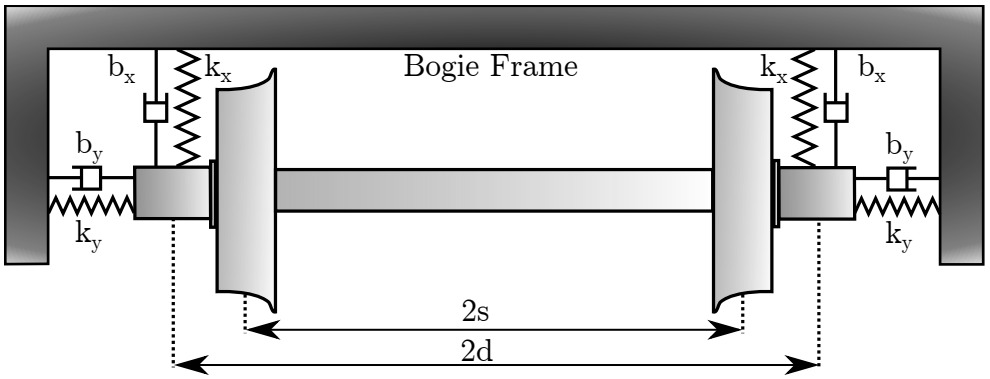

Figure 3.13: Connections between bogie frame and wheelset

Δ_L and Δ_R represent the lateral displacement of the contact points, s is the half of the tape line distance, r_L and r_R are the rolling radii at left and right wheel, respectively. Position vectors of the right and left contact points can be written in terms of wheelset coordinate system as

$$\mathbf{R}_L = -\left(s + \Delta_L\right)\mathbf{j}_w - r_L\mathbf{k}_w, \tag{3.92a}$$

$$\mathbf{R}_R = \left(s - \Delta_R\right)\mathbf{j}_w - r_R\mathbf{k}_w. \tag{3.92b}$$

In terms of equilibrium axes, by using the coordinate transformation matrices, these position vectors are defined as

$$\begin{aligned} R_{L_x} &= \left(s + \Delta_L\right)\cos\phi\sin\psi - r_L\sin\phi\sin\psi, \\ R_{L_y} &= -\left(s + \Delta_L\right)\cos\phi\cos\psi + r_L\sin\phi\cos\psi, \\ R_{L_z} &= -\left(s + \Delta_L\right)\sin\phi - r_L\cos\phi, \end{aligned} \tag{3.93}$$

and for the right contact

$$\begin{aligned} R_{R_x} &= -\left(s - \Delta_R\right)\cos\phi\sin\psi - r_R\sin\phi\sin\psi, \\ R_{R_y} &= \left(s - \Delta_R\right)\cos\phi\cos\psi + r_R\sin\phi\cos\psi, \\ R_{R_z} &= \left(s - \Delta_R\right)\sin\phi - r_R\cos\phi. \end{aligned} \tag{3.94}$$

General equations of motion presented in Equation 3.91 can be rewritten as

$$\sum \mathbf{F} = \mathbf{F}_L + \mathbf{F}_R + \mathbf{N}_L + \mathbf{N}_R + \mathbf{F}_S + W_w\mathbf{k}_{eq}, \tag{3.95a}$$

$$\sum \mathbf{M} = \mathbf{R}_R \times \left(\mathbf{F}_R + \mathbf{N}_R\right) + \mathbf{R}_L \times \left(\mathbf{F}_L + \mathbf{N}_L\right) + \mathbf{M}_L + \mathbf{M}_R + \mathbf{M}_S. \tag{3.95b}$$

Finally, for each degree of the wheelset the general equations of motion can be given by

Longitudinal Equation

$$m\ddot{x} = F_{L_x} + F_{R_x} + N_{L_x} + N_{R_x} + F_{S_x}, \tag{3.96a}$$

Lateral Equation

$$m\ddot{y} = F_{L_y} + F_{R_y} + N_{L_y} + N_{R_y} + F_{S_y}, \tag{3.96b}$$

Vertical Equation

$$m\ddot{z} = F_{L_z} + F_{R_z} + N_{L_z} + N_{R_z} + F_{S_z} - W_w, \tag{3.96c}$$

Roll Equation

$$\begin{aligned} I_{w_x}\ddot{\phi} = I_{w_y}\left(\frac{V_w}{r_0}\right)\dot{\psi} + R_{R_y}\left(F_{R_z} + N_{R_z}\right) - R_{R_z}\left(F_{R_y} + N_{R_y}\right) + \\ R_{L_y}\left(F_{L_z} + N_{L_z}\right) - R_{L_z}\left(F_{L_y} + N_{L_y}\right) + M_{L_x} + M_{R_x} + M_{S_x}, \end{aligned} \tag{3.96d}$$

Spin Equation

$$\begin{aligned} I_{w_y}\ddot{\beta} = R_{R_z}F_{R_x} - R_{R_x}\left(F_{R_z} + N_{R_z}\right) + R_{L_z}F_{L_x} - \\ R_{L_x}\left(F_{L_z} + N_{L_z}\right) + M_{L_y} + M_{R_y} + M_{S_y}, \end{aligned} \tag{3.96e}$$

Yaw Equation

$$\begin{aligned} I_{w_x}\ddot{\psi} = I_{w_y}\left(\frac{V_w}{r_0}\right)\dot{\phi} + R_{R_x}\left(F_{R_y} + N_{R_y}\right) - R_{R_y}F_{R_x} + \\ R_{L_x}\left(F_{L_y} + N_{L_y}\right) - R_{L_y}F_{L_y} + M_{L_z} + M_{R_z} + M_{S_z}. \end{aligned} \tag{3.96f}$$

3.5.1.3 Creepages, Creep Forces and Moments

General form of the creepages are given in Equation 3.44. Assuming that $\mathbf{R}_L^{eq}$ and $\mathbf{R}_R^{eq}$ represents the position vectors for the contact points defined w.r.t. the equilibrium axes and they are given by

$$\begin{aligned} \mathbf{R}_L^{eq} &= x\mathbf{i}_{eq} + y\mathbf{j}_{eq} + z\mathbf{k}_{eq} - (s + \Delta_L)\mathbf{j}_w - r_L\mathbf{k}_w, \\ \mathbf{R}_R^{eq} &= x\mathbf{i}_{eq} + y\mathbf{j}_{eq} + z\mathbf{k}_{eq} + (s - \Delta_R)\mathbf{j}_w - r_R\mathbf{k}_w, \end{aligned} \tag{3.97}$$

then the creepages for the left wheel are defined as

$$\begin{aligned}
\xi_{x_L} &= \left(\dot{\mathbf{R}}_L^{eq}\mathbf{i}_{L_c} - V_w\left(\frac{r_L}{r_0}\right)\cos\psi\right)/V_w, \\
\xi_{y_L} &= \left(\dot{\mathbf{R}}_L^{eq}\mathbf{j}_{L_c}\right)/V_w, \\
\xi_{s_L} &= \left(\omega\mathbf{k}_{L_c}\right)/V_w,
\end{aligned} \tag{3.98}$$

and for the right wheel

$$\begin{aligned}
\xi_{x_R} &= \left(\dot{\mathbf{R}}_R^{eq}\mathbf{i}_{R_c} - V_w\left(\frac{r_R}{r_0}\right)\cos\psi\right)/V_w, \\
\xi_{y_R} &= \left(\dot{\mathbf{R}}_R^{eq}\mathbf{j}_{R_c}\right)/V_w, \\
\xi_{s_R} &= \left(\omega\mathbf{k}_{R_c}\right)/V_w,
\end{aligned} \tag{3.99}$$

where $\mathbf{i}_{L_c}, \mathbf{j}_{L_c}, \mathbf{k}_{L_c}$ and $\mathbf{i}_{R_c}, \mathbf{j}_{R_c}, \mathbf{k}_{R_c}$ are the unit vectors located on the contact axes on the left and right wheels, respectively. Rewriting all vectors in Equation 3.97, 3.98, 3.99 in equilibrium axes and by using algebra with small roll and yaw angles assumption, creepages for the left wheel can be expressed as

$$\begin{aligned}
\xi_{x_L} &= \left(\frac{1}{V_w}\right)\left(V_w\left[1-\left(\frac{r_L}{r_0}\right)\right] + s\dot{\psi}\right), \\
\xi_{y_L} &= \left(\frac{1}{V_w}\right)\left(\dot{y} + r_L\dot{\phi} - V_w\psi\right), \\
\xi_{s_L} &= \left(\frac{1}{V_w}\right)\left(\dot{\psi} + \Omega\delta_L\right)/V_w,
\end{aligned} \tag{3.100}$$

and for the right wheel

$$\begin{aligned}
\xi_{x_R} &= \left(\frac{1}{V_w}\right)\left(V_w\left[1-\left(\frac{r_R}{r_0}\right)\right] - s\dot{\psi}\right), \\
\xi_{y_R} &= \left(\frac{1}{V_w}\right)\left(\dot{y} + r_R\dot{\phi} - V_w\psi\right), \\
\xi_{s_R} &= \left(\frac{1}{V_w}\right)\left(\dot{\psi} - \Omega\delta_R\right)/V_w.
\end{aligned} \tag{3.101}$$

In order to obtain creep forces and moments, theories and models, which are given in Section 3.3, are used. Nevertheless, these creep forces and moments are defined in contact axes. These forces and moments must be expressed in equilibrium coordinate system and for the left wheel and they are defined as

$$\begin{aligned}
F_{L_x}^{eq} &= F_{L_x}^{c}\cos\psi - F_{L_y}^{c}\cos(\delta_L-\phi)\sin\psi,\\
F_{L_y}^{eq} &= F_{L_x}^{c}\sin\psi + F_{L_y}^{c}\cos(\delta_L-\phi)\cos\psi,\\
F_{L_z}^{eq} &= -F_{L_y}^{c}\sin(\delta_L-\phi),\\
M_{L_x}^{eq} &= -M_{L_z}^{c}\sin(\delta_L-\phi)\sin\psi,\\
M_{L_y}^{eq} &= M_{L_z}^{c}\sin(\delta_L-\phi)\cos\psi,\\
M_{L_z}^{eq} &= M_{L_z}^{c}\cos(\delta_L-\phi)
\end{aligned} \tag{3.102}$$

and for the right wheel

$$\begin{aligned}
F_{R_x}^{eq} &= F_{R_x}^{c}\cos\psi - F_{R_y}^{c}\cos(\delta_R+\phi)\sin\psi,\\
F_{R_y}^{eq} &= F_{R_x}^{c}\sin\psi + F_{R_y}^{c}\cos(\delta_R+\phi)\cos\psi,\\
F_{R_z}^{eq} &= F_{R_y}^{c}\sin(\delta_R+\phi),\\
M_{R_x}^{eq} &= M_{R_z}^{c}\sin(\delta_R+\phi)\sin\psi,\\
M_{R_y}^{eq} &= -M_{R_z}^{c}\sin(\delta_R+\phi)\cos\psi,\\
M_{R_z}^{eq} &= M_{R_z}^{c}\cos(\delta_R+\phi).
\end{aligned} \tag{3.103}$$

In this doctoral work, lateral, yaw and vertical dynamics of the wheelset is used for estimation purposes. Especially, lateral and yaw dynamics of the wheelset are used since lateral and yaw dynamic response of the wheelset is strongly connected with the estimated parameters (e.g. friction coefficient and lateral primary suspension). Furthermore, torsional dynamic model of a wheelset would also be a choice for friction estimation, but slip control systems, which are designed to prevent excessive slip (especially at low and very low friction conditions), would not allow a continuous monitoring on the track.

Instead of a rigid support between the wheelset and bogie, dynamic model used here includes a laterally constrained suspended mass (m_m) which can be given by

$$m_m \ddot{y}_m = -F_{Sy}. \tag{3.104}$$

In this equation, F_{Sy} is the acting lateral force due to the lateral suspension elements, and M_{Sz} in Equation 3.96 is the acting yaw moment due to the longitudinal suspension elements, which are defined by

$$F_{Sy} = -2k_y(y - y_m) - 2b_y(\dot{y} - \dot{y}_m), \tag{3.105a}$$

$$M_{Sz} = -2k_x d^2 \psi - 2b_x d^2 \dot{\psi}, \tag{3.105b}$$

where d is the half of the distance between suspension centres and it can be seen clearly in Figure 3.13. These forces and moments are defined in the axis of wheelset centre, and they must be transformed into the fixed inertial frame by using transformation matrices. Parameters for the dynamic model of the wheelset, which are considered here, can be found in Table 3.4. Unless stated otherwise, parameters in Table 3.4 are used throughout this study.

Table 3.4: Wheelset dynamic model parameters

Parameters	Definitions	Values
V_w	Longitudinal Velocity of Wheelset	40 m/s
r_0	Nominal Radius of Wheels	0.46 m
s	Half of the Tape Line Distance	0.75 m
G	Shear Modulus of Rigidity of Wheel and Rail	8×10^{10} Pa
F_n	Wheel Load	55 kN
k_y	Lateral Spring Stiffness	2×10^6 N/m
k_x	Longitudinal Spring Stiffness	4×10^6 N/m
b_y	Lateral Damping Coefficient	1×10^3 Ns/m
b_x	Longitudinal Damping Coefficient	1×10^3 Ns/m
d	Half of the Distance Between Suspension Centers	1 m
m_w	Mass of the Wheelset	1813 kg
m_m	Suspended Mass	6241 kg
I_{wy}	Moment of Inertia of Wheelset Around y Axis	112 kgm^2
I_{wz}	Moment of Inertia of Wheelset Around x Axis	1120 kgm^2

3.5.2 Dynamic Model of a Railway Vehicle

A 7 DOF dynamic model, which is reported in the chapter II.5 of the study by (Gerlici et al., 2005), is also used to reveal if secondary vertical suspension of a vehicle can be identified from its dynamic response. Parameters are selected according to the values of European Rail Research Institute (i.e. ERRI) B176 benchmark vehicle presented by (Iwnicki, 1998). Parameters, which are considered for this dynamic model, can be found in Table 3.5. As well as wheelsets, this dynamic model considers all other parts (i.e. bogie and vehicle body) of the vehicle. Since wheelsets do not have significant mass compared to bogies and coaches, wheelsets are assumed to be massless in this model. Another assumption is that the input for this system is vertical irregularities in the left and right rails. The vehicle is illustrated in Figure 3.14.

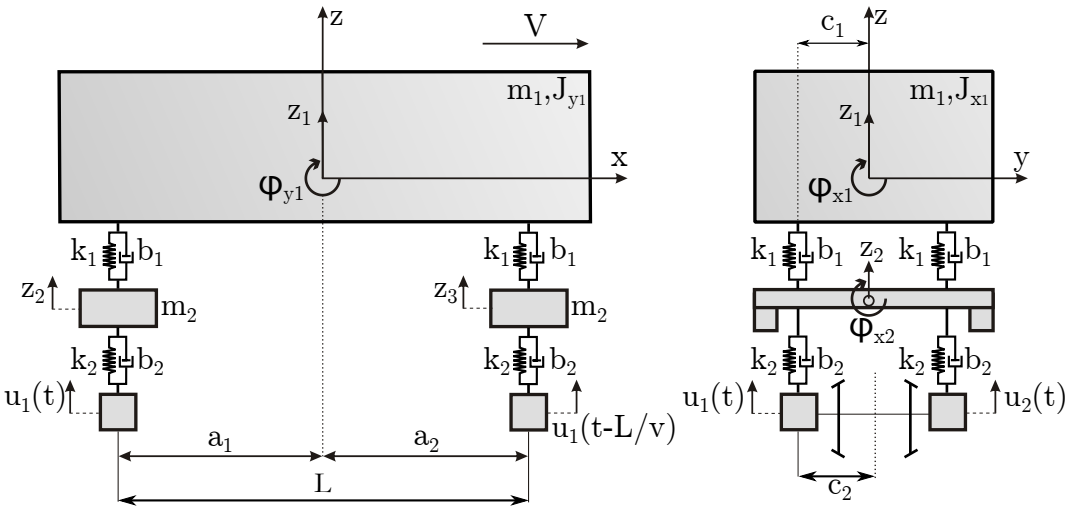

Figure 3.14: A 7 DOF dynamic model of a railway vehicle, figure is adapted from (Gerlici et al., 2005)

This dynamic model is assumed to be linearised around the operating state and the state in vector form can be expressed as

$$\mathbf{x} = \left[z_1, \quad \phi_{y1}, \quad \phi_{x1}, \quad z_2, \quad \phi_{x2}, \quad z_3, \quad \phi_{x3} \right], \tag{3.106}$$

where z_1, z_2, z_3 represents the displacement on the z–axis of the coach, bogie on the left and right side, respectively and $\phi_{y1}, \phi_{x2}, \phi_{x3}$ represents the roll displacement around the

Table 3.5: Parameters for the dynamic model of the vehicle

Parameters	Definitions	Values
m_1	Mass of the Coach	32000 kg
m_2	Mass of the Bogie	2615 kg
k_1	Stiffness of the Secondary Spring	430×10^3 N/m
k_2	Stiffness of Primary Spring	122×10^4 N/m
b_1	Damping Coefficient of Secondary Suspension	20×10^3 Ns/m
b_2	Damping Coefficient of Primary Suspension	4×10^3 Ns/m
J_{y1}	Moment of Inertia of the Coach around y–axis	197×10^4 kgm^2
J_{x1}	Moment of Inertia of the Coach around x–axis	56800 kgm^2
J_{x2}	Moment of Inertia of the Bogie around x–axis	1722 kgm^2
c_1	Lateral Semi–Spacing of Secondary Suspension	1 m
c_2	Lateral Semi–Spacing of Primary Suspension	1 m
a_1	Longitudinal Semi–Spacing of Secondary Suspension	9.5 kg
a_2	Longitudinal Semi–Spacing of Primary Suspension	9.5 kg
V	Velocity of the Vehicle	20 m/s

specified axes of the bodies. In general form, equations of motion for this 7 DOF system can be presented as

$$\mathbf{M}\ddot{\mathbf{x}} + \mathbf{B}\dot{\mathbf{x}} + \mathbf{K}\mathbf{x} = \mathbf{T}_b\dot{\mathbf{u}} + \mathbf{T}_k\mathbf{u}, \tag{3.107}$$

where $\mathbf{M}$ is the mass matrix, $\mathbf{B}$ is the damping matrix, $\mathbf{K}$ is the stiffness matrix, $\mathbf{T}_b$ is the damping matrix for the velocity of vertical track irregularities and $\mathbf{T}_k$ is the stiffness matrix for vertical track irregularities. $\mathbf{u}$ is the vector of vertical track irregularities and $\dot{\mathbf{u}}$ is the velocity vector of vertical track irregularities. Elements of these matrices can be found in the Appendix of the Section II.5 of the study by (Gerlici et al., 2005). $\mathbf{u}$ is simply equal to the z_{irr_L} and z_{irr_R} of each rail segment presented in Figure 3.9, and $\dot{\mathbf{u}}$ is obtained by using numerical derivation of z_{irr_L} and z_{irr_R} w.r.t. time.

For simplicity in numerical calculations, Equation 3.107 can be rewritten as a first order differential equation as

$$\begin{bmatrix} \mathbf{I} & 0 \\ 0 & \mathbf{M} \end{bmatrix} \dot{\mathbf{x}}_{red} + \begin{bmatrix} 0 & -\mathbf{I} \\ \mathbf{K} & \mathbf{B} \end{bmatrix} \mathbf{x}_{red} = \mathbf{T}_b\dot{\mathbf{u}} + \mathbf{T}_k\mathbf{u}, \tag{3.108}$$

where $\mathbf{x}_{red}$ represents the reduced order state and it is given by

$$\mathbf{x}_{red} = \left[z_1,\ \phi_{y1},\ \phi_{x1},\ z_2,\ \phi_{x2},\ z_3,\ \phi_{x3},\ \dot{z}_1,\ \dot{\phi}_{y1},\ \dot{\phi}_{x1},\ \dot{z}_2,\ \dot{\phi}_{x2},\ \dot{z}_3,\ \dot{\phi}_{x3} \right]. \tag{3.109}$$

3.5.3 Dynamic Model of the Tram Wheel Test Stand

Conducting on–track experiments for railway vehicles is difficult and for research purposes roller–rig test stands are frequently used. Test stand used in DFJP, UPCE, Czech Republic has a wheel on roller configuration. A schema of this test stand can be seen in Figure 3.15 and in Figure 3.16 pictures of the roller–rig can be found. In this doctoral study, an estimation case is defined to validate the use of estimation algorithms by considering measurements.

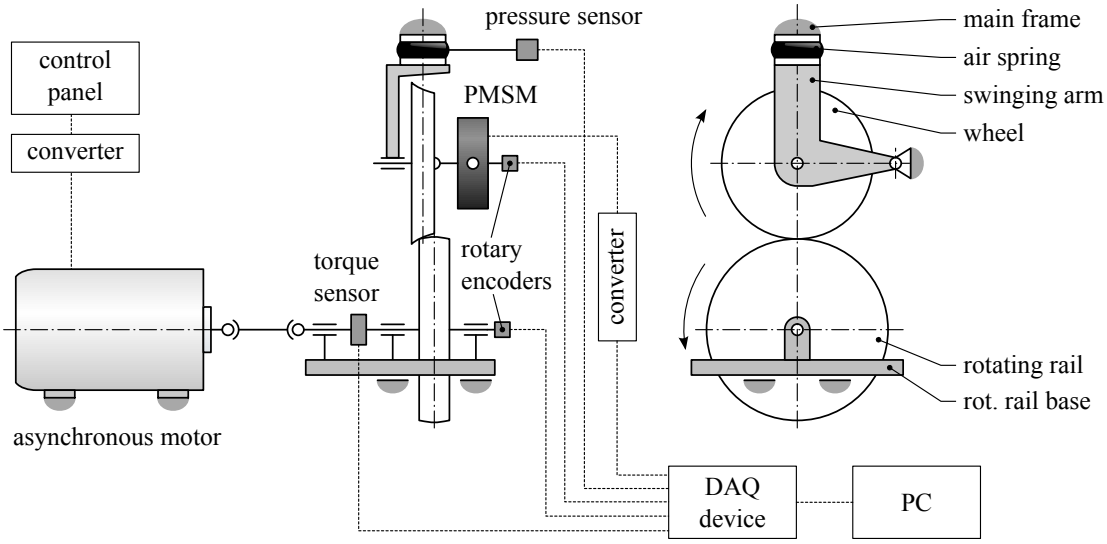

Figure 3.15: A schema of the tram wheel test stand

The test rig includes a full-scale tram wheel and a roller ("rotating rail") manufactured from a railway wagon wheel. Both wheel and roller are carried by an upright frame, the wheel is attached to a swinging arm with a pneumatic spring for normal force, the roller is mounted on bearings of a base plate. A limited angle of attack can be adjusted in this setup and it can be shifted laterally. In order to provide traction or braking on the wheel, the machine is equipped with a torque–controlled permanent

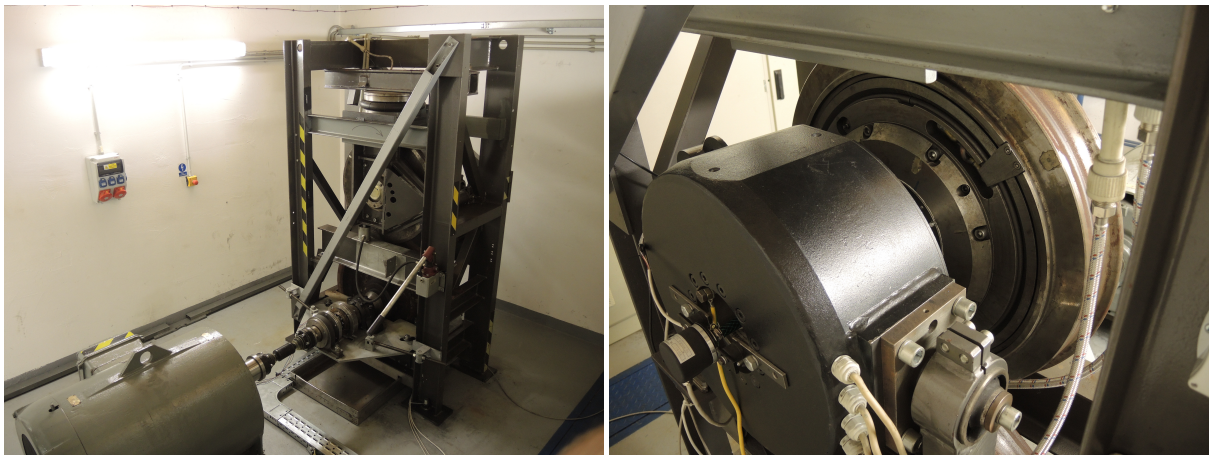

(a) **(b)**

Figure 3.16: Tram wheel test stand DFJP, UPCE

magnet synchronous motor (i.e. PMSM). Its effect is opposed by an asynchronous motor of the roller which is operated to keep constant speed as stated by (Voltr and Lata, 2015).

A pressurised air spring generates the normal force and the air pressure is observed by a pressure transmitter of type DMP331 produced by BD SENSORS, Germany. The incremental rotary encoders of type IRC315 produced by LARM, Czech Republic are mounted on both shafts to provide the angular velocities of the wheel (ω_w) and the roller (ω_r). The tangential force T and the coefficient of adhesion f (ratio of the tangential force to the normal force) are calculated from the output of a torque transducer on the roller shaft. The data acquisiton (i.e. DAQ) device of type NI USB-6341 produced by National Instruments, United States is used to collect sensory data. Similar configurations are used around the globe and such an example of roller–rig with contact force calculation is presented by using a dynamo-meter by (Meymand and Ahmadian, 2016). The electric motor connected to the wheel is a PMSM which has a nominal power of 58 kW, a nominal torque of 852 Nm and maximum torque of 2000 Nm. Additionally, the electric motor connected to the roller is an asynchronous motor produced by the manufacturer MEZ Brno, Czech Republic which has a nominal power of 55 kW and a nominal torque of 891 Nm. The nominal rolling diameter of the wheel is 700 mm and the nominal rolling diameter of the roller is 905 mm.

3.5.3.1 Electrical Motors of Tram Wheel Test Stand

The tram wheel is driven by a PMSM with feedback flux weakening control as stated by (Doleček et al., 2009). The details of this motor and control procedure is reported by (Doleček et al., 2009). Therefore, details about PMSM and its control method are omitted hereby. In this doctoral work, torque applied by this motor is provided as a torque request from this controller. However, the asynchronous motor attached to the roller, which is used for breaking, were ignored in previous researches since tangential force and adhesion coefficient are obtained by using a torque transducer attached to the roller shaft. In order to obtain opposing torque of this asynchronous motor w.r.t. the angular velocity, its equivalent circuit model should be obtained by some simple tests as mentioned by (Sen, 2007). These are no load test, blocked rotor test and measuring per phase stator resistances. After these tests were carried out, the Thevenin equivalent circuit was obtained at 50 Hz and the equivalent circuit for this frequency can be seen in Figure 3.17. This asynchronous motor is controlled with an open loop volts per Hertz (i.e. V/f) control scheme by using a rectifier and inverter couple as it is seen in the diagram given in Figure 3.18. When the frequency decreases, in order to keep constant flux and to protect the motor, line voltage must also decrease proportionally to frequency so that V/f ratio can be kept constant as stated by (Sen, 2007). Mechanical torque of the asynchronous motor can be given as follows

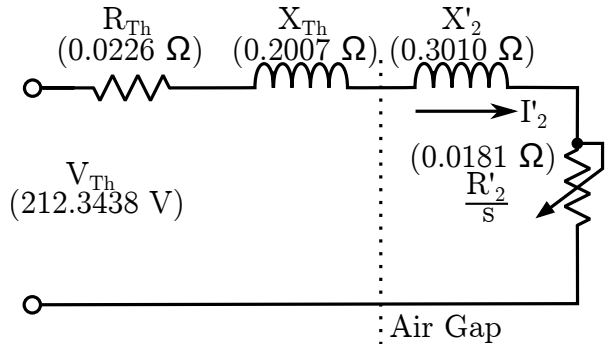

Figure 3.17: Thevenin equivalent circuit of the asynchronous motor

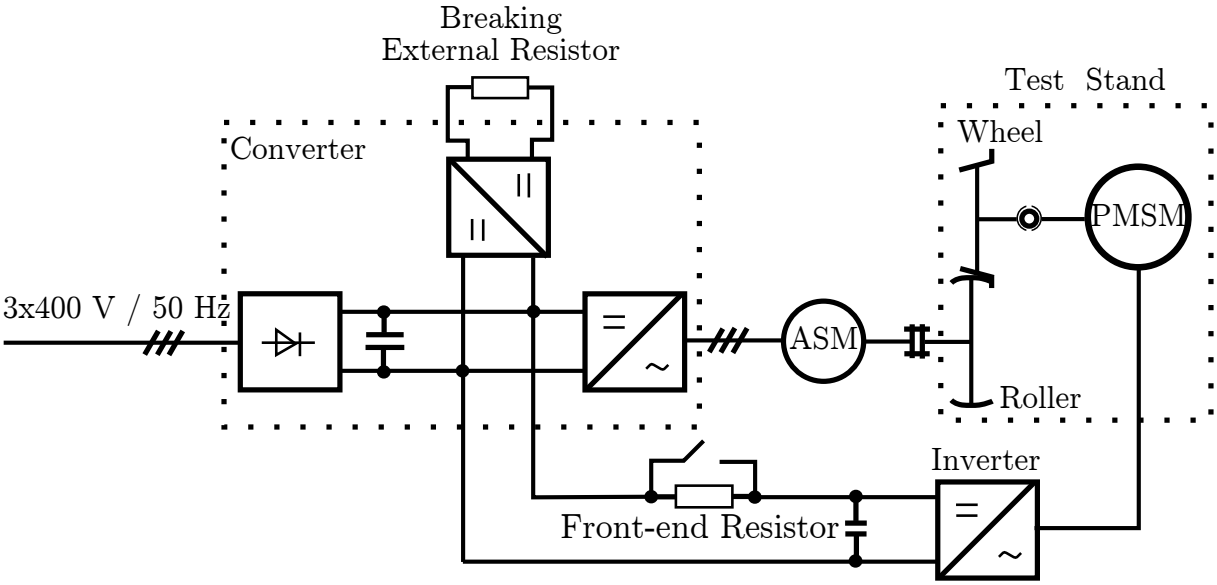

Figure 3.18: Electrical schema of the test stand, figure is adapted from (Doleček et al., 2009)

$$T_{mech} = \frac{3}{\omega_{syn}} \frac{V_{Th}^2}{\left(R_{Th} + \frac{R_2'}{s}\right)^2 + \left(X_{Th} + X_2'\right)^2} \frac{R_2'}{s_m}, \tag{3.110}$$

where ω_{syn} is the synchronous speed of the electrical motor, s_m is the slip. V_{Th}, R_{Th}, X_{Th} is the Thevenin voltage, resistance and reactance on the stator side. R_2' and X_2' is the reflected resistance and the reactance of the rotor, respectively.

By using the measured electrical parameters of the asynchronous motor, torque–speed characteristic is obtained at 50 Hz and it can be seen in Figure 3.19. Observable maximum torque in Figure 3.19 is about 2000 Nm. For comparison, the datasheet of a similar motor from same manufacturer, which is reported by (MEZ, 2016), is used. This motor is named as 3AFP–315–S and it has same number of poles, nominal power and similar structural properties. In the data–sheet given by (MEZ, 2016), the motor used for comparison has a nominal torque of 889 Nm and the ratio of maximum torque to nominal torque is 2. The asynchronous motor attached to the roller is fairly old (produced in 1982) and undergone a lot of maintenance. Therefore, it is concluded that the difference between measurements and datasheet information is admissible. These measurements are also validated by simulations in which a torsional dynamic model is

used and in Section 4.5 results are provided.

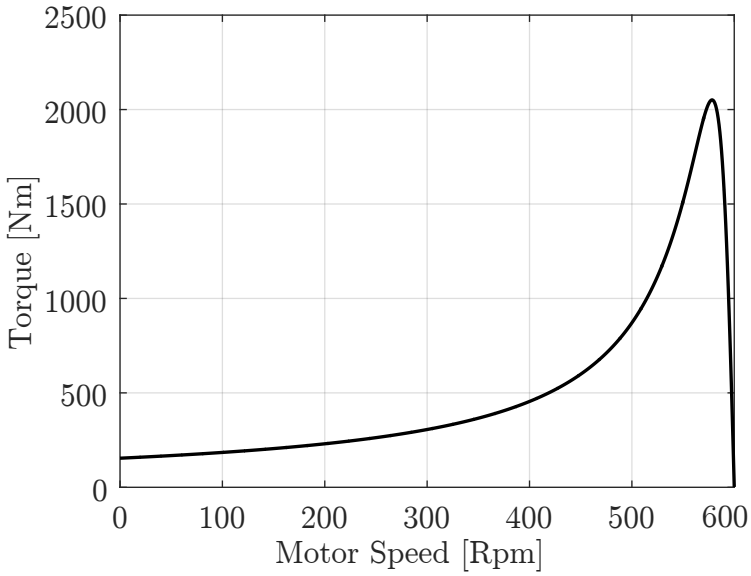

Figure 3.19: Torque–speed characteristic of the asynchronous motor at 50 Hz

3.5.3.2 Torsional Dynamic Model of the Tram Wheel Test Stand

Forces and torques, which are affecting on the system, can be seen in Figure 3.20. Torsional dynamic model of the roller–rig can be expressed as

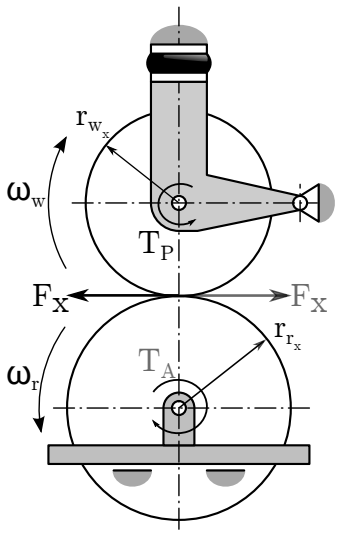

Figure 3.20: Forces and torques acting on the test stand

$$\frac{d\dot{\omega}_r}{dt} = \frac{T_A + (F_x \times r_{r_x})}{J_{r_{total}}}, \tag{3.111a}$$

$$\frac{d\dot{\omega}_w}{dt} = \frac{-T_P - (F_x \times r_{w_x})}{J_{w_{total}}}, \tag{3.111b}$$

where $J_{w_{total}}$ and $J_{r_{total}}$ are the total moment of inertias of wheel–roller with connection components, respectively. These values for the wheel–roller are obtained as 17.86 kgm^2 and 47.2 kgm^2 by using a 3D modelling software, respectively. T_A and T_P are the applied torques by asynchronous motor and PMSM, respectively. r_{w_x} and r_{r_x} are the longitudinal rolling radii of the wheel and roller, respectively. Additionally, F_x is the longitudinal creep force, which occurs in the contact plane, and it can be calculated by using the methods in Section 3.3.

3.6 Filtering and Estimation

In this doctoral study, the family of Kalman filters are preferred. Therefore, in this section details of these filters are provided.

3.6.1 Discrete Time Kalman Filter

The studies based on Kalman filtering start with the original paper of Kalman, (Kalman, 1960). As stated by (Faragher et al., 2012), even Kalman filter is 50 years old, it is still one of the most important data fusion and filtering algorithm.

Throughout the dissertation, dynamic models previously presented are used in discrete time form. Therefore, discrete time Kalman filter is derived here. The procedure reported by (Simon, 2006) is followed.

It is assumed that a linear discrete time system, which is similar to the system presented in Section 3.5.2, is given in the form

$$\mathbf{x}_k = \mathbf{F}_{k-1}\mathbf{x}_{k-1} + \mathbf{G}_{k-1}\mathbf{u}_{k-1} + \mathbf{q}_{k-1}, \tag{3.112a}$$

$$\mathbf{y}_k = \mathbf{H}_k\mathbf{x}_k + \mathbf{r}_k. \tag{3.112b}$$

Aim is to obtain state $\mathbf{x}_k$ at discrete time instant k by using the equation given in 3.112a with the available noisy measurements. $\mathbf{q}_k \sim N(0, \mathbf{Q})$ and $\mathbf{r}_k \sim N(0, \mathbf{R})$ are zero-mean, uncorrelated Gaussian white noises. If all the measurements up to time k are present, a posteriori estimate can be expressed by using these measurements and it is denoted as $\hat{\mathbf{x}}_k^+$. In order to find out posteriori estimate, conditional probability of the expected (i.e. mean) value of $\mathbf{x}_k$ on all measurements up to discrete time k should be found and it is expressed as

$$\hat{\mathbf{x}}_k^+ = \mathbf{E}\left[\mathbf{x}_k | \mathbf{y}_1, \mathbf{y}_2 \dots \mathbf{y}_k\right] \ (\textit{posteriori estimate}). \tag{3.113}$$

If measurements up to discrete time k–except at time k–are available, then a priori estimate can be found by using this data and it can be given as

$$\hat{\mathbf{x}}_k^- = \mathbf{E}\left[\mathbf{x}_k | \mathbf{y}_1, \mathbf{y}_2 \dots \mathbf{y}_{k-1}\right] \ (\textit{priori estimate}). \tag{3.114}$$

Both priori and posteriori estimates are predictions of the state. However, priori estimate is the estimate before the measurement at time k is taken.

If it is desired to find best prediction of the state ahead of the measurements, a predicted estimate should be defined. Simply, it can be given as conditional probability of the expected (i.e. mean) value of $\mathbf{x}_k$ on all available measurements up to discrete time k

$$\hat{\mathbf{x}}_{k|k-M} = \mathbf{E}\left[\mathbf{x}_k | \mathbf{y}_1, \mathbf{y}_2 \dots \mathbf{y}_{k-M}\right] \ (\textit{predicted estimate}), \tag{3.115}$$

where M is a positive integer. An illustration of the posteriori, priori and predicted estimates can be found in Figure 3.21.

$\hat{\mathbf{x}}_0^+$ is called the initial estimate. Since there is no measurement available before time $k = 0$, $\hat{\mathbf{x}}_0^+$ can be defined as expected value of initial state x_0.

$$\hat{\mathbf{x}}_0^+ = \mathbf{E}\left[\mathbf{x}_0\right] \ (\textit{initial estimate}). \tag{3.116}$$

In Kalman filtering, $\mathbf{P}_k$ is called as covariance of the estimation error. $\mathbf{P}_k^-$ refers to

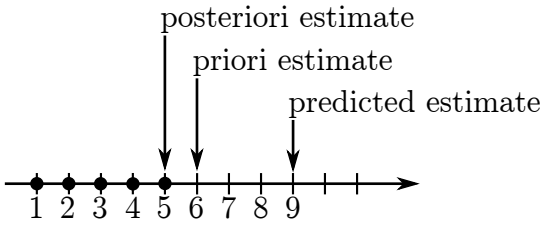

Figure 3.21: An illustration of the posteriori, priori and predicted state estimates. It is assumed that only measurements up to time $k = 5$ is available. An estimation of time $k = 5$ is called posteriori, at time $k = 6$ is called priori and for time $k > 6$ is called predicted estimate, figure is adapted from (Simon, 2006)

the covariance of the estimation error $\hat{\mathbf{x}}_k^-$ and $\mathbf{P}_k^+$ refers to the covariance of the estimation error $\hat{\mathbf{x}}_k^+$. These covariances are expresed as

$$\mathbf{P}_k^- = \mathbf{E}\left[\left(\mathbf{x}_k - \hat{\mathbf{x}}_k^-\right)\left(\mathbf{x}_k - \hat{\mathbf{x}}_k^-\right)^T\right], \tag{3.117a}$$

$$\mathbf{P}_k^+ = \mathbf{E}\left[\left(\mathbf{x}_k - \hat{\mathbf{x}}_k^+\right)\left(\mathbf{x}_k - \hat{\mathbf{x}}_k^+\right)^T\right]. \tag{3.117b}$$

After initial estimate, priori estimate $\hat{\mathbf{x}}_1^-$ must be calculated. State vector evolves by using Equation 3.112a. $\hat{\mathbf{x}}_1^-$ is defined as

$$\hat{\mathbf{x}}_1^- = \mathbf{F}_0\hat{\mathbf{x}}_0^+ + \mathbf{G}_0\mathbf{u}_0. \tag{3.118}$$

In general form, this equation is given by

$$\hat{\mathbf{x}}_k^- = \mathbf{F}_{k-1}\hat{\mathbf{x}}_{k-1}^+ + \mathbf{G}_{k-1}\mathbf{u}_{k-1}, \tag{3.119}$$

which is called time update equation. There are no measurements available up to that time. Therefore, system state can only be predicted by using the system dynamics (i.e. model). The next step is the calculation of covariance of the state estimation error. If initial state is available, then $\mathbf{P}_0^+ = 0$. $\mathbf{P}_0^+$ represents the uncertainty of the initial estimate $\hat{\mathbf{x}}_0^+$ and can be expressed as

$$\mathbf{P}_0^+ = \mathbf{E}\left[\left(\mathbf{x}_0 - \hat{\mathbf{x}}_0^+\right)\left(\mathbf{x}_0 - \hat{\mathbf{x}}_0^+\right)^T\right]. \tag{3.120}$$

Then $\mathbf{P}_1^-$ should be calculated by using the Equation 3.119 and Equation 3.117b, general form of propagation is defined as

$$\begin{aligned}\left[\left(\mathbf{x}_k-\hat{\mathbf{x}}_k\right)\left(\mathbf{x}_k-\hat{\mathbf{x}}_k\right)^T\right] &= \left(\mathbf{F}_{k-1}\mathbf{x}_{k-1}+\mathbf{G}_{k-1}\mathbf{u}_{k-1}+\mathbf{q}_{k-1}-\hat{\mathbf{x}}_k\right)\\ &\quad \left(\mathbf{F}_{k-1}\mathbf{x}_{k-1}+\mathbf{G}_{k-1}\mathbf{u}_{k-1}+\mathbf{q}_{k-1}-\hat{\mathbf{x}}_k\right)^T\\ &= \left[\mathbf{F}_{k-1}\left(\mathbf{x}_{k-1}-\hat{\mathbf{x}}_{k-1}\right)+\mathbf{q}_{k-1}\right]\\ &\quad \left[\mathbf{F}_{k-1}\left(\mathbf{x}_{k-1}-\hat{\mathbf{x}}_{k-1}\right)+\mathbf{q}_{k-1}\right]^T, \end{aligned} \tag{3.121}$$

and finally by recalling that $(\mathbf{x}_{k-1}-\hat{\mathbf{x}}_{k-1})$ is uncorrelated with noise vector $\mathbf{q}_{k-1}$, general form of propagation of covariance can be expressed as

$$\mathbf{P}_k^- = \mathbf{F}_{k-1}\mathbf{P}_{k-1}^+\mathbf{F}_{k-1}^T+\mathbf{Q}_{k-1}.^1 \tag{3.122}$$

Thus, if $\mathbf{P}_0^+$ is provided, then by using Equation 3.122, $\mathbf{P}_1^-$ can be expressed as

$$\mathbf{P}_1^- = \mathbf{F}_0\mathbf{P}_0^+\mathbf{F}_0^T+\mathbf{Q}_0. \tag{3.123}$$

Equation 3.122 is called as the time-update equation for P. These are the time update equations for state estimate and covariance. $\hat{\mathbf{x}}_k^+$ should be calculated when $\hat{\mathbf{x}}_k^-$ is provided. By considering the relation ship between $\hat{\mathbf{x}}_k^+$ and $\hat{\mathbf{x}}_k^-$, $\hat{\mathbf{x}}_k^+$ is written as

$$\hat{\mathbf{x}}_k^+ = \hat{\mathbf{x}}_k^- + \mathbf{K}_k\left(\mathbf{y}_k-\mathbf{H}_k\hat{\mathbf{x}}_k^-\right). \tag{3.124}$$

By following a similar procedure carried out to obtain Equation 3.122, general form of the update equation for covariance matrix after measurement is obtained as

$$\mathbf{P}_k^+ = \left(\mathbf{I}-\mathbf{K}_k\mathbf{H}_k\right)\mathbf{P}_k^-\left(\mathbf{I}-\mathbf{K}_k\mathbf{H}_k\right)^T+\mathbf{K}_k\mathbf{R}_k\mathbf{K}_k^T. \tag{3.125}$$

Equations 3.124 and 3.125 are denoted as measurement update equations. In these

[1] In Equation 3.122 - and + signs are used to show whether covariances are obtained before or after the measurements are given at specific time instant.

equations, $\mathbf{K}_k$ is called Kalman gain. Attention must be paid to this gain since Kalman gain should be optimal. The most suitable optimality criterion is the minimization of the sum of the covariances of estimation errors up to time k. Sum of the covariances of estimation errors stands for a cost function which is expressed as

$$\begin{aligned}\mathbf{J}_k =& \mathbf{E}\left[\left(\mathbf{x}_1 - \hat{\mathbf{x}}_1^+\right)\left(\mathbf{x}_1 - \hat{\mathbf{x}}_1^+\right)^T\right] + \cdots + \mathbf{E}\left[\left(\mathbf{x}_k - \hat{\mathbf{x}}_k^+\right)\left(\mathbf{x}_k - \hat{\mathbf{x}}_k^+\right)^T\right], \\ \mathbf{J}_k =& Tr\left(\mathbf{P}_k^+\right),\end{aligned} \tag{3.126}$$

where Tr represents the trace of a square matrix. In order to find optimal value of the Kalman gain, first partial derivative of the Equation 3.126 w.r.t. $\mathbf{K}_k$ must be taken. The property, which $\frac{\partial Tr(XYX^T)}{\partial X} = 2XY$, if Y is symmetric, should be noted. Then, by using the chain rule, partial derivative of the cost function is obtained as

$$\frac{\partial \mathbf{J}_k}{\partial \mathbf{K}_k} = 2\left(\mathbf{I} - \mathbf{K}_k\mathbf{H}_k\right)\mathbf{P}_k^-\left(-\mathbf{H}_k^T\right) + 2\mathbf{K}_k\mathbf{R}_k. \tag{3.127}$$

Equation 3.127 should be zero for optimal gain, then optimal Kalman filter gain can be found by solving this equation as

$$\begin{aligned}\mathbf{K}_k\mathbf{R}_k &= \left(\mathbf{I} - \mathbf{K}_k\mathbf{H}_k\right)\mathbf{P}_k^-\mathbf{H}_k^T, \\ \mathbf{K}_k\left(\mathbf{R}_k + \mathbf{H}_k\mathbf{P}_k^-\mathbf{H}_k^T\right) &= \mathbf{P}_k^-\mathbf{H}_k^T, \\ \mathbf{K}_k &= \mathbf{P}_k^-\mathbf{H}_k^T\left(\mathbf{H}_k\mathbf{P}_k^-\mathbf{H}_k^T + \mathbf{R}_k\right)^{-1}.\end{aligned} \tag{3.128}$$

Finally, by using first equation of Equation 3.128 and Equation 3.125, covariance update equation after the measurement can be rewritten as

$$\mathbf{P}_k^+ = \left(\mathbf{I} - \mathbf{K}_k\mathbf{H}_k\right)\mathbf{P}_k^-, \tag{3.129}$$

and by using first equation of Equation 3.128 and Equation 3.129, Kalman gain in terms

of $\mathbf{P}_k^+$ is given by

$$\mathbf{K}_k = \mathbf{P}_k^+ \mathbf{H}_k^T \mathbf{R}_k^{-1}. \tag{3.130}$$

An algorithmic approach for Kalman filter can be found in Algorithm 2.

Algorithm 2 Kalman filter

function KF($\hat{\mathbf{x}}$, $\dot{\hat{\mathbf{x}}}$,$\mathbf{P}$)
  Initialize
    $\hat{\mathbf{x}}_0^+ \leftarrow \mathbb{E}[\mathbf{x}_0]$ ▷ Initial State Estimation
    $\mathbf{P}_0^+ \leftarrow \mathbb{E}\left[(\mathbf{x_0} - \hat{\mathbf{x}}_\mathbf{0})(\mathbf{x_0} - \hat{\mathbf{x}}_\mathbf{0})^T\right]$ ▷ Initial Covariance Estimation
  End
end function
function TIME UPDATE($\hat{\mathbf{x}}_{k-1}^+$, $\mathbf{P}_{k-1}^+$)
  for $k \in \{1, \ldots, \infty\}$ **do**
    $\mathbf{x}_k^- \leftarrow \mathbf{F}_{k-1}\hat{\mathbf{x}}_{k-1}^+ + \mathbf{G}_{k-1}\mathbf{u}_{k-1}$ ▷ Priori State Estimation
  end for
  for $k \in \{1, \ldots, \infty\}$ **do**
    $\mathbf{P}_k^- \leftarrow \mathbf{F}_{k-1}\mathbf{P}_{k-1}^+\mathbf{F}_{k-1}^T + \mathbf{Q}_{k-1}$ ▷ Priori Covariance Matrix
  end for
end function
function MEASUREMENT UPDATE($\mathbf{x}_k^-$, $\mathbf{P}_k^-$)
  for $k \in \{1, \ldots, \infty\}$ **do**
    $\mathbf{K}_k \leftarrow \mathbf{P}_k^-\mathbf{H}_k^T\left(\mathbf{H}_k\mathbf{P}_k^-\mathbf{H}_k^T + \mathbf{R}_k\right)^{-1}$ ▷ Kalman Gain Calculation
  end for
  for $k \in \{1, \ldots, \infty\}$ **do**
    $\mathbf{x}_k^+ \leftarrow \hat{\mathbf{x}}_k^- + \mathbf{K}_k\left(\mathbf{y}_k - \mathbf{H}_k\hat{\mathbf{x}}_k^-\right)$ ▷ Posteriori State Estimation
  end for
  for $k \in \{1, \ldots, \infty\}$ **do**
    $\mathbf{P}_k^+ \leftarrow (\mathbf{I} - \mathbf{K}_k\mathbf{H}_k)\,\mathbf{P}_k^-$ ▷ Posteriori Covariance Matrix
  end for
end function

3.6.2 Discrete Time Unscented Kalman Filter

Kalman filter is an effective method in case of linear systems. However, most of the systems in practice are nonlinear in nature. Therefore, Kalman filter is not applicable for such systems.

EKF is an alternative for nonlinear systems. Nevertheless, Jacobian matrix of

the nonlinear system is needed to use EKF. Even in linearisable systems, calculation of Jacobian matrix is not an easy task and it is an error prone operation. Unscented transformation (i.e. UT) is proposed to overcome these difficulties. Very first explanation of this transformation is provided by (Julier et al., 1995). In UKF states and parameters are used as Gaussian random variables from a set of carefully chosen points, (Wan and Van Der Merwe, 2001). These sample points are named as sigma points and various type of filters based on sigma points are presented by (Van Der Merwe, 2004). UKF and particle filters are similar in structure, but the most obvious difference is that sigma points are chosen deterministically unlike the particles in particle filter. Thus, almost same amount of information can be extracted by using small amount of points. Most significant properties of the UKF can be listed as

- UKF uses finite number of points. Therefore, when a model with inputs and outputs are defined, UKF can be used as a black box filtering to estimate states and parameters,
- Computational complexity of the UKF is as low as EKF,
- UKF can be used with discontinuous transformations of the systems.

3.6.2.1 Unscented Transformation

Given the error covariance $\mathbf{P}_x$, points with same error covariance can be generated. If original distribution has zero mean, these points will also have zero mean. Otherwise, by simply adding the mean of the distribution, these sample points can be generated. Easily, by considering the positive and negative roots of the distribution (i.e. $\sqrt{\mathbf{P}_x}$ with dimension L) a symmetric $2L$ points with same error covariance can be obtained. This is the minimum number of points that can be obtained by using the error covariance. Points carrying unnecessary information may exist by using a random sampling even if the distribution of these points have same mean and covariance.

Considering propragation of a random variable $\mathbf{x}$ through a nonlinear function $\mathbf{y} = f(\mathbf{x})$ and assuming $\mathbf{x}$ has mean $\bar{\mathbf{x}}$ together with the covariance $\mathbf{P}_x$, in order to calculate statistical information about $\mathbf{y}$, a vector of sample points $\boldsymbol{\chi}$ with $2L+1$ elements is defined as

$$\chi_0 = \bar{\mathbf{x}} \tag{3.131}$$

$$\chi_i = \bar{\mathbf{x}} + \left(\sqrt{L + \lambda \mathbf{P}_x}\right)_i, \qquad i =, \ldots, L \tag{3.132}$$

$$\chi_i = \bar{\mathbf{x}} - \left(\sqrt{L + \lambda \mathbf{P}_x}\right)_{i-L}, \quad i = L+1, \ldots, 2L \tag{3.133}$$

where λ

$$\lambda = \alpha^2 (L + \kappa) - L, \tag{3.134}$$

is a scaling parameter. α is a constant which determines the distribution of the sigma points around the mean $\bar{\mathbf{x}}$ and usually considered as $10^{-4} \leq \alpha \leq 1$. κ is the secondary scaling parameter and it is considered generally as $3 - L$.

These sigma points should also be propagated in order to obtain statistical properties of the $\mathbf{y}$

$$\boldsymbol{\Upsilon}_i = f(\boldsymbol{\chi}_i). \quad i = 0, \ldots, 2L \tag{3.135}$$

Mean and covariance of $\mathbf{y}$ are found by using the weighted mean and covariance of posteriori sigma points as

$$\bar{\mathbf{y}} = \sum_{i=0}^{2L} W_i^{(m)} \boldsymbol{\Upsilon}_i, \tag{3.136}$$

$$\mathbf{P}_{\mathbf{y}} = \sum_{i=0}^{2L} W_i^{(c)} \left(\boldsymbol{\Upsilon}_i - \bar{\mathbf{y}}\right) \left(\boldsymbol{\Upsilon}_i - \bar{\mathbf{y}}\right)^T, \tag{3.137}$$

where these weights are defined as

$$W_0^{(m)} = \frac{\lambda}{L + \lambda}, \tag{3.138}$$

$$W_0^{(c)} = \frac{\lambda}{L + \lambda} + 1 - \alpha^2 + \beta, \tag{3.139}$$

$$W_i^{(m)} = W_i^{(c)} = \frac{1}{2\,(L+\lambda)}, \qquad i = L+1, \ldots, 2L \tag{3.140}$$

and β represents the prior knowledge about the distribution of the $\mathbf{x}$ and for Gaussian distributions optimal value of β is 2. Determination of sigma points differ from the particles of particle filter or Monte Carlo sampling methods. As stated by (Wan and Van Der Merwe, 2001), for Gaussian inputs UT provides third–order accurate approximations. For non–Gaussian case, UT provides at least second order accurate approximations and accuracy can be further improved by choosing appropriate α and β. An illustration of the UT can be seen in Figure 3.22.

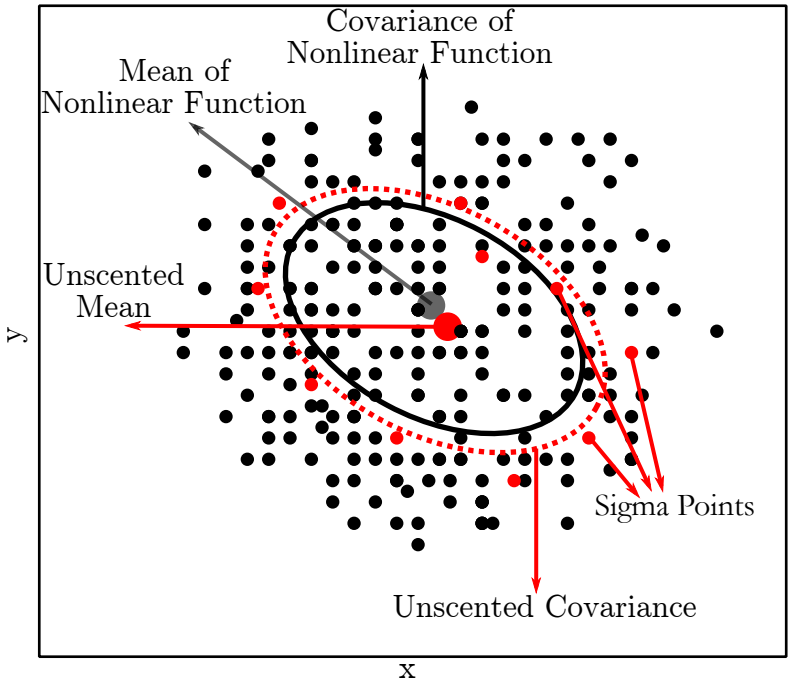

Figure 3.22: Illustration of UT, figure is adapted from (Simon, 2006)

3.6.2.2 Filtering Method

Consider the continuous time nonlinear system in the form as stated by (Zheng et al., 2010):

$$\dot{\mathbf{x}}(t) = f\left(\mathbf{x}(t), \mathbf{u}(t)\right) + \mathbf{q}(t), \tag{3.141}$$

$$\mathbf{y}(t) = h\left(\mathbf{x}(t), \right) + \mathbf{r}(t), \tag{3.142}$$

where $\mathbf{x}(t) \in \mathbb{R}^n$ is the system state vector, $\mathbf{u}(t) \in \mathbb{R}$ is the input, $\mathbf{y}(t) \in \mathbb{R}^m$ is the measurement vector (i.e. system output), $\mathbf{q}(t) \sim N(0, \mathbf{Q}(t))$ and $\mathbf{r}(t) \sim N(0, \mathbf{R}(t))$ are process and measurement noises, respectively. In this doctoral work, systems are considered as discretized continuous systems and they are expressed as

$$\mathbf{x}_k = f_d\left(\mathbf{x}_{k-1}, \mathbf{u}_{k-1}, k-1\right) + \mathbf{q}_{k-1}, \tag{3.143}$$

$$\mathbf{y}_k = h\left(\mathbf{x}_k, k-1\right) + \mathbf{r}_k, \tag{3.144}$$

where $\mathbf{x}_k = \mathbf{x}(kT)$, the subscript k represents discrete time, and T is the sampling period. The function f_d does not require an explicit formula.

A non-augmented (i.e. additive noise case) joint unscented Kalman filter structure is used in this doctoral work since it has an advantage of less computational complexity.

Similar to the Kalman filtering in linear case, the first step in UKF is also initialization and initial state estimate and the covariance is given by

$$\hat{\mathbf{x}}_0^+ = \mathbf{E}\left[\mathbf{x}_0\right], \tag{3.145}$$

$$\mathbf{P}_0^+ = \mathbf{E}\left[\left(\mathbf{x}_0 - \hat{\mathbf{x}}_0^+\right)\left(\mathbf{x}_0 - \hat{\mathbf{x}}_0^+\right)^T\right]. \tag{3.146}$$

The next step in UKF is the generation of sigma points by using

$$\chi_0 = \hat{\mathbf{x}}_{k-1}, \tag{3.147}$$

$$\chi_i = \hat{\mathbf{x}}_{k-1} + \left(\gamma_f S_{k-1}\right)_i, \quad i =, \ldots, L \tag{3.148}$$

$$\chi_i = \hat{\mathbf{x}}_{k-1} - \left(\gamma_f S_{k-1}\right)_i . \quad i = L+1, \ldots, 2L \tag{3.149}$$

where $\gamma_f = \sqrt{L+\lambda}$ and $S_{k-1} = \sqrt{P_{k-1}}$. Then, these sigma points must be propagated by using the nonlinear system equation without noise

$$\chi^{(i)}_{k|k-1} = f_d\left(\chi^{(i)}_{k-1}, \mathbf{u}_{k-1}, k-1\right), \tag{3.150}$$

and a priori state estimate and error covariance are provided as

$$\hat{\mathbf{x}}^-_k = \sum_{i=0}^{2L} W^m_i \chi^{(i)}_{k|k-1}, \tag{3.151}$$

$$\mathbf{P}^-_{x_k} = \sum_{i=0}^{2L} W^c_i \left(\chi^{(i)}_{k|k-1} - \hat{\mathbf{x}}^-_k\right)\left(\chi^{(i)}_{k|k-1} - \hat{\mathbf{x}}^-_k\right)^T + \mathbf{Q}. \tag{3.152}$$

Equation 3.151 and 3.152 are the time update equations for UKF. Now, the measurement update equations must be formed. In this step, propagated sigma points obtained in Equation 3.135 are used to form predicted measurements

$$\Upsilon^{(i)}_{k|k-1} = h\left(\chi^{(i)}_{k-1}, k-1\right). \tag{3.153}$$

Thus, priori measurement estimate and error covariance can be expressed as

$$\hat{\mathbf{y}}^-_k = \sum_{i=0}^{2L} W^m_i \Upsilon^{(i)}_{k|k-1}, \tag{3.154}$$

$$\mathbf{P}^-_{y_k} = \sum_{i=0}^{2L} W^c_i \left(\Upsilon^{(i)}_{k|k-1} - \hat{\mathbf{y}}^-_k\right)\left(\Upsilon^{(i)}_{k|k-1} - \hat{\mathbf{y}}^-_k\right)^T + \mathbf{R}. \tag{3.155}$$

Additionally, a cross covariance between state estimates and predicted measurements are given by

$$\mathbf{P}^-_{x_k y_k} = \sum_{i=0}^{2L} W^c_i \left(\chi^{(i)}_{k|k-1} - \hat{\mathbf{x}}^-_k\right)\left(\Upsilon^{(i)}_{k|k-1} - \hat{\mathbf{y}}^-_k\right)^T. \tag{3.156}$$

Similar to the measurement updates in Kalman filtering, posteriori state estimates

and error covariance are written as

$$\mathbf{K}_k = \mathbf{P}^-_{x_k y_k} \mathbf{P}^-_{y_k}, \tag{3.157}$$

$$\hat{\mathbf{x}}^+_k = \hat{\mathbf{x}}^-_k + \mathbf{K}_k \left(\mathbf{y}_k - \hat{\mathbf{y}}^-_k \right), \tag{3.158}$$

$$\mathbf{P}^+_{x_k} = \mathbf{P}^-_{x_k} - \mathbf{K}_k \mathbf{P}^-_{y_k} \mathbf{K}^T_k. \tag{3.159}$$

Readers of this study are highly referred to the studies of (Kandepu et al., 2008), (Matzuka et al., 2012) which are explaining the application of UKF for nonlinear dynamic systems which the researchers from all branches of science can understand and apply UKF for state and parameter estimation in nonlinear dynamic systems. Besides, a review of performance measures for such kind of filters are presented by (Haug, 2012). An algorithmic approach of the UKF is provided in Algorithm 3.

Algorithm 3 Joint Unscented Kalman filter - Additive Noise Case Algorithm

Define Filter Parameters and Weights
  $L, \alpha, \kappa, \beta \leftarrow constant$ ▷ Filter Parameters
  $\lambda \leftarrow \alpha^2(L+\kappa) - L$ ▷ Scaling Parameter
  $\gamma_f \leftarrow \sqrt{L+\lambda}$
  $W_0^{(m)} \leftarrow \frac{\lambda}{L+\lambda}$ ▷ Initial Weights in UKF
  $W_0^{(c)} \leftarrow \frac{\lambda}{L+\lambda} + 1 - \alpha^2 + \beta$ ▷ Initial Weights in UKF
  for $i \leftarrow \{1, \ldots, 2L\}$ **do**
    $\mathbf{W}_i^{(m)} \leftarrow \mathbf{W}_i^{(c)} := \frac{1}{2(L+\lambda)}$ ▷ Weights in UKF
  end for
End
function UKF($\hat{\mathbf{x}}$, $\dot{\hat{\mathbf{x}}}$,$\mathbf{P}$)
  Initialize
    $\hat{\mathbf{x}}_0^+ \leftarrow \mathbb{E}[\mathbf{x}_0]$ ▷ Initial State Estimation
    $\mathbf{P}_0^+ \leftarrow \mathbb{E}\left[(\mathbf{x_0} - \hat{\mathbf{x}}_0^+)(\mathbf{x_0} - \hat{\mathbf{x}}_0^+)^T\right]$ ▷ Initial Error Covariance
  End
end function
function Sigma Points($\hat{\mathbf{x}}$, $\mathbf{P}$)
  Define
    $\mathbf{S}_{k-1} \leftarrow \sqrt{\mathbf{P}_{k-1}}$
  End
  for $k \in \{1, \ldots, \infty\}$ **do**
    $\boldsymbol{\chi}_{k-1} \leftarrow \left[\hat{\mathbf{x}}_{k-1}, \hat{\mathbf{x}}_{k-1} + \gamma_f \mathbf{S}_{k-1}, \hat{\mathbf{x}}_{k-1} - \gamma_f \mathbf{S}_{k-1}\right]$ ▷ Sigma Point Generation
  end for
end function
function Time Update(χ_{k-1}, $\mathbf{P}$, $\mathbf{Q}$)
  $\chi^i_{k|k-1} \leftarrow f(\chi^i_{k-1}, u_{k-1})$ ▷ Propagation of Sigma Points
  $\hat{\mathbf{x}}_k^- \leftarrow \sum_{i=0}^{2L} \mathbf{W}_i^{(m)} \chi^i_{i,k|k-1}$ ▷ Priori State Estimate
  $\mathbf{P}_k^- \leftarrow \sum_{i=0}^{2L} \mathbf{W}_i^{(c)} (\chi^i_{i,k|k-1} - \hat{\mathbf{x}}_k^-)(\chi^i_{i,k|k-1} - \hat{\mathbf{x}}_k^-)^T + \mathbf{Q}$ ▷ Priori Error Covariance
end function
function Measurement Update($\chi^i_{k|k-1}$, $\mathbf{R}$)
  $\boldsymbol{\Upsilon}^i_{k|k-1} \leftarrow h(\chi^*_{k|k-1}, u_{k-1})$
  $\hat{\mathbf{y}}_k^- \leftarrow \sum_{i=0}^{2L} \mathbf{W}_i^{(m)} \boldsymbol{\Upsilon}^i_{i,k|k-1}$ ▷ Priori Measurement Estimate
  $\mathbf{P}_{y_k} \leftarrow \sum_{i=0}^{2L} \mathbf{W}_i^{(c)} (\boldsymbol{\Upsilon}^i_{i,k|k-1} - \hat{\mathbf{y}}_k^-)(\boldsymbol{\Upsilon}^i_{i,k|k-1} - \hat{\mathbf{y}}_k^-)^T + \mathbf{R}$ ▷ Measurement Error Covariance
  $\mathbf{P}_{x_k y_k} \leftarrow \sum_{i=0}^{2L} \mathbf{W}_i^{(c)} (\chi^i_{i,k|k-1} - \hat{\mathbf{x}}_k^-)(\boldsymbol{\Upsilon}^i_{i,k|k-1} - \hat{\mathbf{y}}_k^-)^T$ ▷ Cross Error Covariance
  $\mathbf{K}_k \leftarrow \mathbf{P}_{x_k y_k} \mathbf{P}_{y_k}^{-1}$ ▷ Kalman Gain Calculation
  $\hat{\mathbf{x}}_k^+ \leftarrow \hat{\mathbf{x}}_k^- + \mathbf{K}_k(y_k - \hat{\mathbf{y}}_k^-)$ ▷ Posteriori State Estimate
  $\mathbf{P}_k^+ \leftarrow \mathbf{P}_k^- - \mathbf{K}_k \mathbf{P}_{\tilde{y}_k \tilde{y}_k} \mathbf{K}_k^T$ ▷ Posteriori Error Covariance
end function

4 *Results and Discussion*

4.1 Wheel–Rail (Roller) Geometrical Specifications

In this section, results, which include wheel–rail geometrical specifications, are presented.

Firstly, the conicity angle and lateral curvature of the UIC60E1 type rail with 1:40 inclination is provided and a comparison with a previous research by (Shevtsov, 2008) is given. These results can be seen in Figure 4.1.

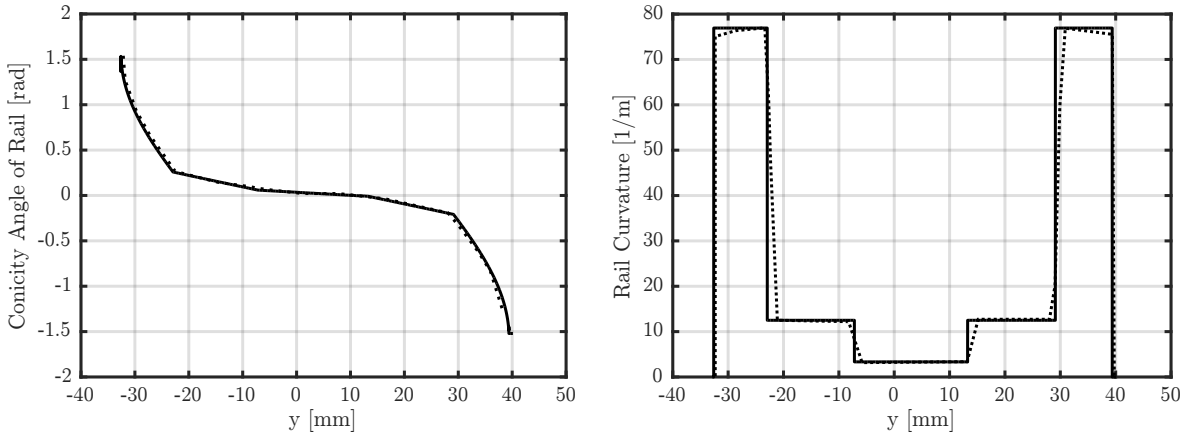

(a) Conicity angle of the rail **(b)** Lateral curvature of the rail

Figure 4.1: Two parameters of the UIC60E1 rail profile, solid line represents result of this study and dashed line represents results of the study by (Shevtsov, 2008) (figure is adapted from that study)

The small difference between the results are caused by the use of different calculation approaches. The discrete points created for wheel–rail profiles are connected with piecewise cubic Hermite interpolating polynomial by (Shevtsov, 2008), whereas in this study, just the discrete points are used. These points are formed with a 0.01 mm grid and for geometrical analysis of the wheel–rail, this grid is fine (i.e. sufficient) when compared with the grid (0.02 mm) of the MBS tool by (Gensys, 2016).

Given the discrete points for the wheel–rail, conicity angles are calculated by using Equation 3.1. Wheel–rail lateral curvature can be obtained by using Equation 3.3. Longitudinal curvature of the rail is considered as zero due to the straight track assumption and the longitudinal curvature of the wheel is provided by finding the rolling

radius of the wheel. During calculation of conicity angles and curvatures, the derivatives are taken by using the numerical differentiation scheme proposed by the (Fornberg, 1988), as stated previously. Results for the right wheel of a wheelset is also provided and can be seen in Figure 4.1. These parameters are also compared with the results of the study by (Shevtsov, 2008) and it is observed that results of both studies are in very good agreement.

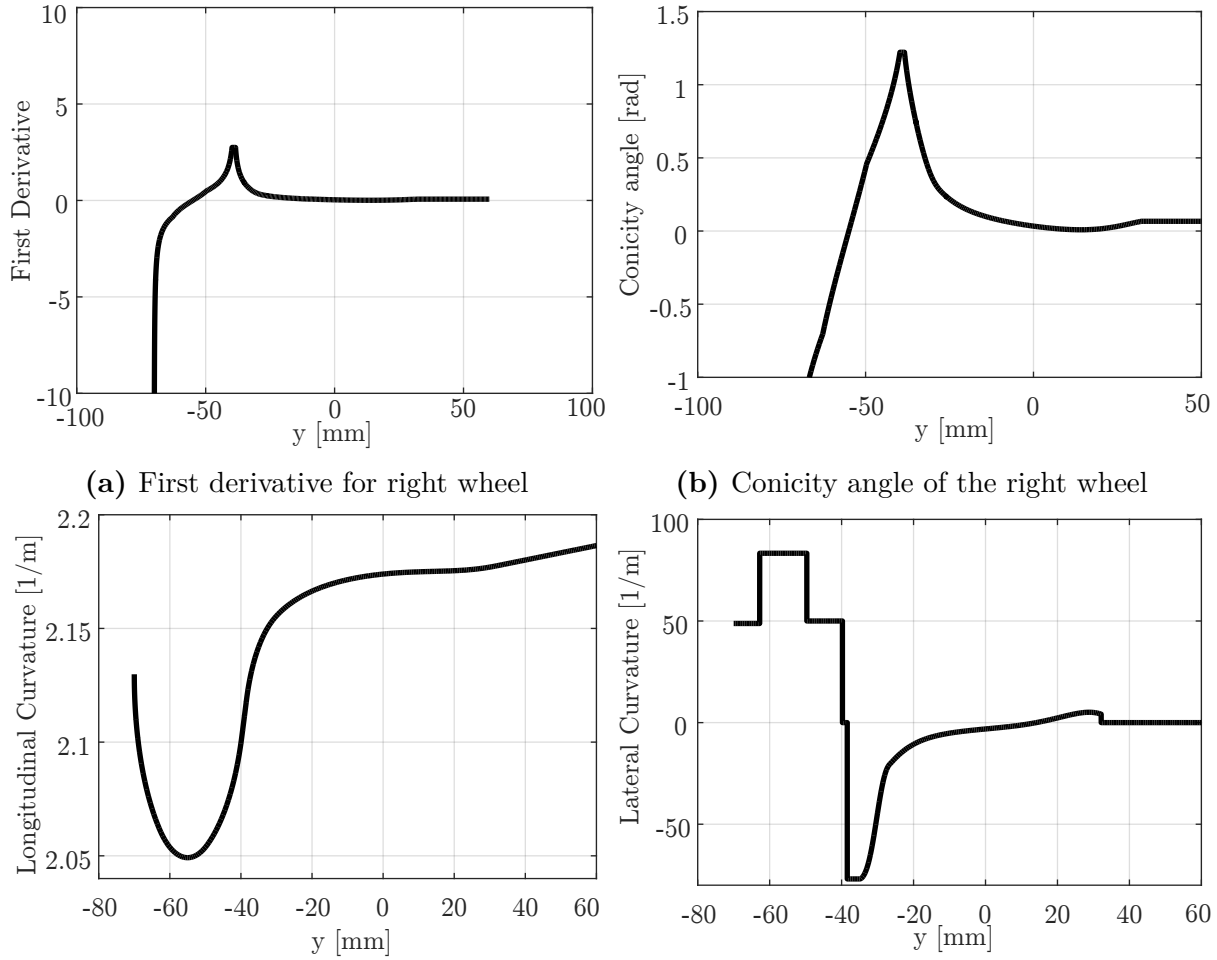

(a) First derivative for right wheel

(b) Conicity angle of the right wheel

(c) Longitudinal curvature of the right wheel

(d) Lateral curvature of the right wheel

Figure 4.2: Geometrical parameters of the right wheel (S1002 type) of a wheelset

In order to validate estimation method on the tram wheel test stand, tram wheel and roller profiles must also be created and analysed. As stated in Section 3.1.1, due to extensive use, the wheel–roller has recently been reprofiled and named as "W169" and "R169". These profiles have been designed particularly for the roller rig and their conicity and curvatures are similar to those of common wheels and rails used in the

tramway network of Prague, Czech Republic. Profiles, which are measured by using a miniprof device and the nominal wheel–roller profiles, are illustrated in Figure 3.2. In order to analyse the contact, rolling radii in longitudinal (roller diameter - 0.9043 m, wheel diameter - 0.6964 m) and lateral directions and the contact angle must be obtained. The longitudinal rolling radii for the wheel–roller become available by using the measurements with a diameter tape. Similar to the wheel–rail case, mathematical tools presented in Equations 3.1 and 3.3 are used to obtain the lateral rolling radii and the contact angle. The results for measured profiles are provided in Figure 4.3 and these results are in good agreement with the results which are found by using nominal profiles. The second order numerical differentiation mentioned previously is used to take derivatives. The results are unsuitable to use in a Hertzian contact analysis due to the sudden changes of curvature values. Therefore, a simple moving average filter with a window length of 5 mm is used.

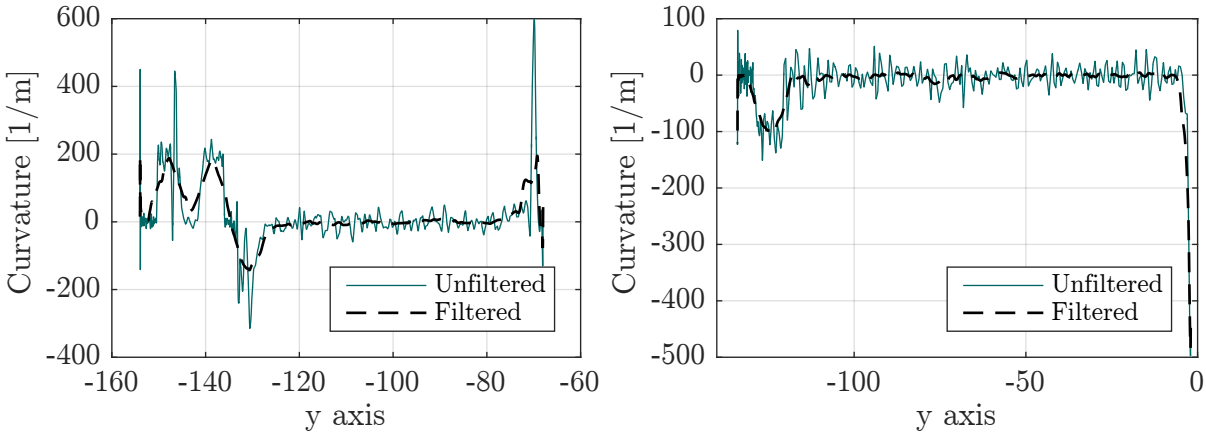

(a) Tram wheel lateral curvature **(b)** Roller lateral curvature

Figure 4.3: Lateral curvatures of wheel–roller of the tram wheel test stand

4.2 Semi–Analytical Method for Contact Locus

In this section, results for the semi–analytical method mentioned in Section 3.1.2 are presented. Two main feature, which are especially important in the investigation of the wheelset dynamics, can be seen in Figure 4.4. These are the roll angle of the wheelset and the rolling radius difference for the wheels of the wheelset. Hereby, a comparison is also provided with the results of MBS tool given by (Gensys, 2016) and they are in perfect

agreement as it can be seen from the Figure.

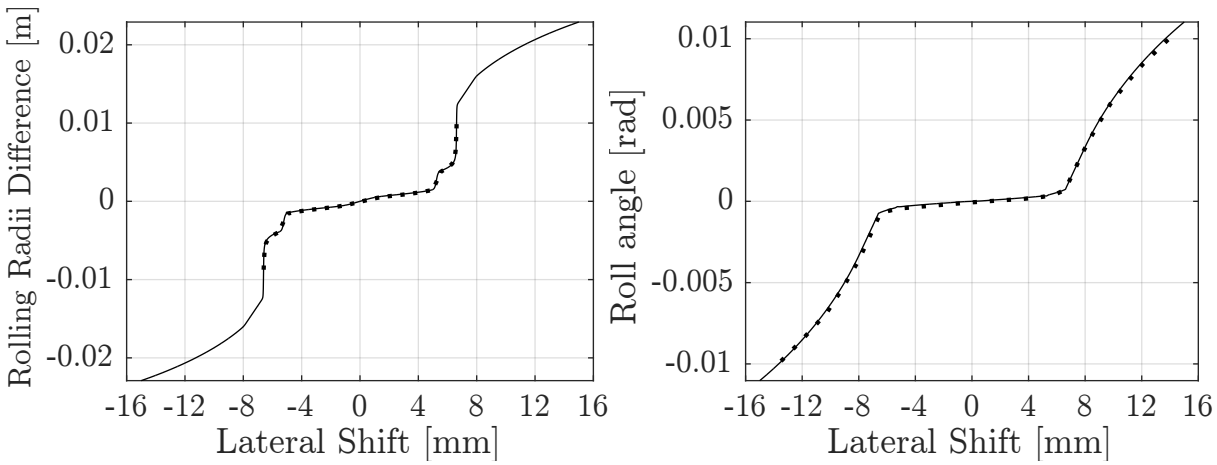

Figure 4.4: Rolling radii difference and roll angle of the wheelset w.r.t. lateral shift, solid lines represent results of this study and dashed lines are adapted from the results by (Gensys, 2016), they represent the results of this MBS tool.

4.3 Quasi–Elastic Contact Search

As stated in Section 3.1.3, quasi–elastic contact search method provides smoothness of the equations of motion and takes the elastic deformation of the wheel–rail interface into account. The difference in the interconnections between wheel–rail w.r.t. lateral shift values is illustrated in Figure 4.5. It is obvious that quasi–elastic search provides smooth distribution of the contact points. Additionally, there are sharp jumps in the distribution of contact points due to the sudden curvature changes in the rigid search, and lateral position of the contact points on the right wheel are found and presented in Figure 4.6. This figure demonstrates how quasi–elastic contact search smooths the characteristic. Figure 4.6 also shows the jumps of contact points and the situation can be noted easily. This method is also applied for tram wheel stand by using mesured profiles and can be seen in Figure 4.7. Since a torsional dynamic model is used for tram wheel test stand, only one point contact is considered. Result in Figure 4.7 presents that use of quasi–elastic method changes the location of the contact point compared to rigid contact point.

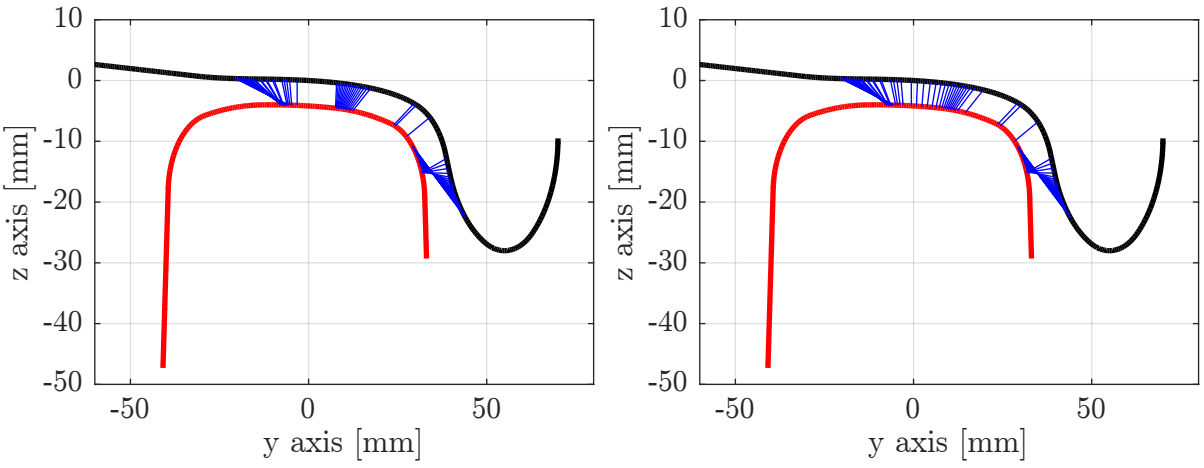

(a) Rigid contact search **(b)** Quasi–elastic contact search

Figure 4.5: A comparison of contact points interconnections between quasi–elastic and rigid contact search

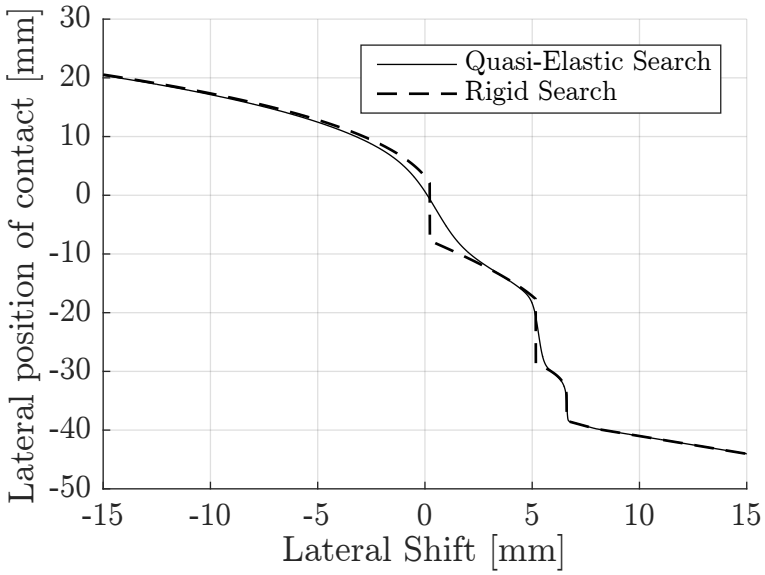

Figure 4.6: Comparison of rigid and quasi–elastic contact search results for lateral position of contact on right wheel

4.4 Solution of the Normal Problem

4.4.1 Results for Theory of Hertz

In order to find an approximate creep force, contact patch dimensions are required. The contact patch length and width obtained w.r.t. lateral shift can be found in Figure 4.8 for a 70 kN normal load. In order to validate the results, again the result for semi–axes

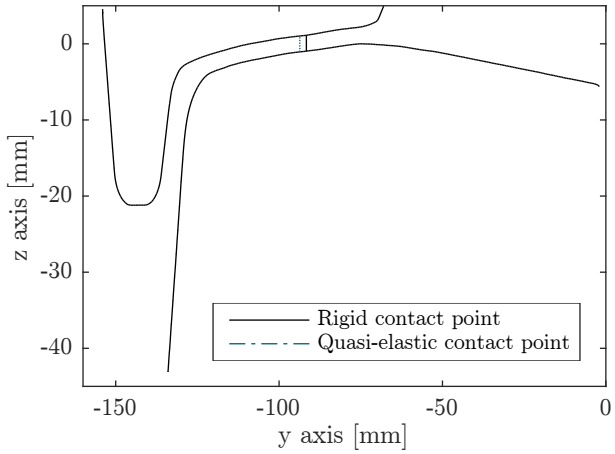

Figure 4.7: Comparison of rigid and quasi–elastic contact search results for tram wheel contact point

ratio of contact patch of the MBS tool, which is provided by (Gensys, 2016), is used. This comparison is presented in Figure 4.9. Firstly, loading of the wheelset and types of wheel–rail profiles are same for both studies. However, there is no information about the methods of contact search and normal solution which are used by (Gensys, 2016). Biggest difference between results in Figure 4.9 is seen in the area of switching from wheel tread to the flange and in the flange contact. Additionally, it is a well–known fact that theory of Hertz does not provide accurate results in case of flange contact where contact angle changes substantially within the same contact patch as stated by (Burgelman et al., 2014). The non–conformal contact assumption of Hertz fails in case of flange contact. Flange contact occurs especially in the arcs of turnouts and in curves. For such cases, different contact models must be used, (Burgelman et al., 2014). In this doctoral work, since the level of track irregularities does not cause a flange contact and straight track is assumed, it is concluded that theory of Hertz is sufficient. Although it is not stated by (Gensys, 2016), a different method might be used in case of flange contact similar to method presented by (Burgelman et al., 2014).

4.4.2 Results for Virtual Penetration Method

In this section, results for the method expressed in Section 3.2.2 are provided and it can be seen in Figure 4.10. Obviously, this method provides especially a change in the

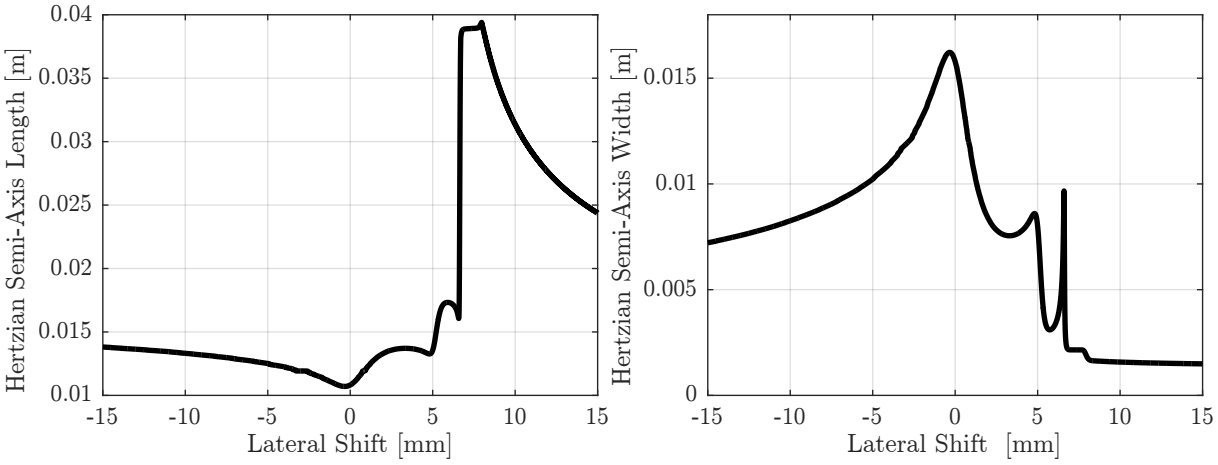

(a) Contact patch length **(b)** Contact patch width

Figure 4.8: Contact patch width and length of the right wheel of a wheelset w.r.t. lateral shift of the wheelset

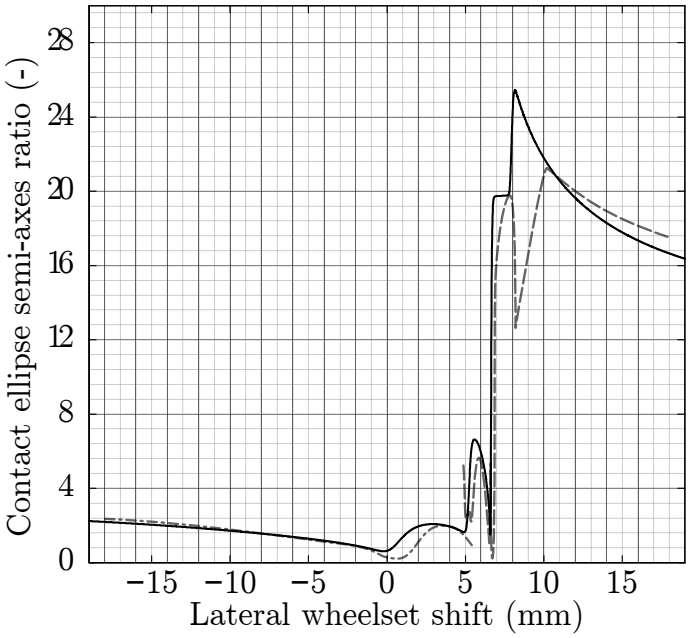

Figure 4.9: Contact patch semi–axes ratio of right wheel for a 70 kN normal load, solid lines represent results of this study and dashed lines are adapted from the study by (Gensys, 2016), they represent the results of this MBS tool.

results for the flange contact. It has been observed that the semi–axes ratio decreases by using this method. Results for virtual penetration method are compared with the results provided in Figure 1 of the study by (Sichani et al., 2014). The notable similarity between results is while the length of contact patch increases width decreases or vice versa. This

method is currently used in a MBS tool, namely Simpack, as stated by (Vollebregt et al., 2011).

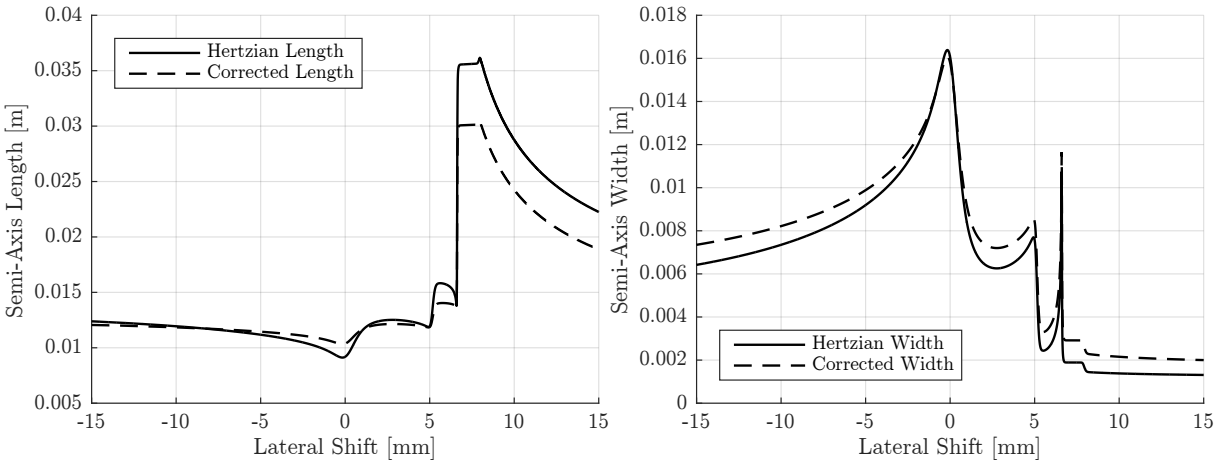

(a) Contact patch length **(b)** Contact patch width

Figure 4.10: Contact patch width and length of the right wheel of a wheelset w.r.t. lateral shift of the wheelset by using the virtual penetration method given in Section 3.2.2

4.5 Results for Tangential Problem Solution and Validation of Dynamic Models

Tangential problem solution with several methods presented in Section 3.3; details of the dynamic models of the wheelset, vehicle and test stand are provided in Section 3.5, and results are given in this section of study. Especially for friction condition estimation, a 2 DOF wheelset dynamic model, which includes lateral and yaw dynamics, is considered. Since dynamic response of the wheelset is determined by the creep forces, results for tangential problem solution and dynamic response are presented together. In order to validate results, a 6 DOF free wheelset model of a MBS tool named Universal Mechanism (i.e. UM) is used. This validation provides a confirmation of all the solution methodology for lateral dynamic response of a free wheelset including contact search, normal and tangential problem solution. Additionally, validation highlights if a 2 DOF simplified dynamic model of a wheelset can represent the motion of 6 DOF MBS tool dynamic model. User interface of (UM, 2016) simulation tool can be seen in Figure 4.11.
The basic differences and similarities between the models are

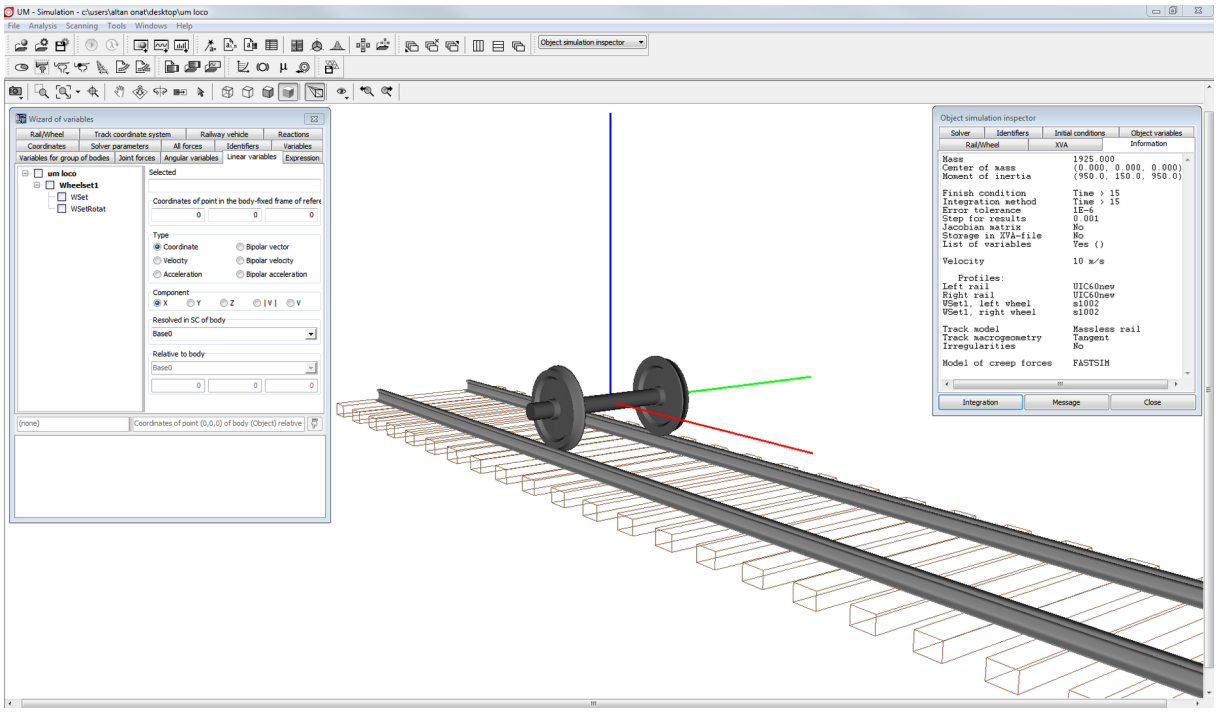

Figure 4.11: User interface of MBS tool Universal Mechanism

- The most significant difference is that the model used in this study is specific to lateral and yaw dynamics of the wheelset and it has just 2 DOF, whereas in UM MBS simulation the wheelset has 6 DOF. Thus, other DOF cause a difference between results.
- Contact search method in UM is different from the one used in this doctoral study. (UM, 2016) finds contact points based on the iterative solution of a nonlinear equation of lateral and vertical shift. Determination of contact points affects the results since different points on the wheel surface have different equivalent conicity values. Equivalent conicity definition is provided in Section 1.4. An example for how different contact search algorithm alters wavelength of the results can be seen in Figure 4.12. In this scenario, a 2 DOF unsuspended (i.e. without bogie and suspension elements) wheelset dynamic model, which has a 10 m/s constant forward velocity, is initiated with a 3 mm lateral shift on a track. In order to calculate creep forces, Fastsim is used. The difference in wavelengths of the lateral motion are observable for rigid and quasi–elastic contact search methods. The scatter of the contact points on wheel surface for same lateral shift values are already presented in

Figure 4.5. The conclusion for different wavelengths in hunting motion is the use of different contact search methods since calculation of different contact points results in different equivalent conicity values.

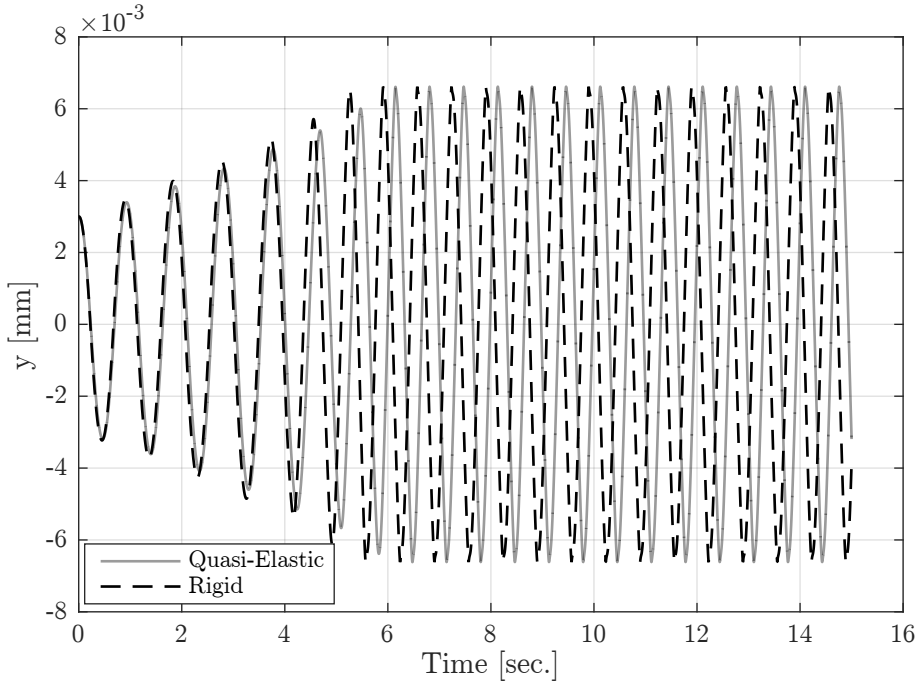

Figure 4.12: Effect of different contact search methods (rigid and quasi–elastic) on hunting motion (15 sec.) of an unsuspended wheelset

- Similarly, Fastsim method and the fourth order Runge–Kutta integration method used in this doctoral work also exists in Universal Mechanism tool. Results for the Fastsim are obtained by using a 20x20 discretization throughout the study.
- There is no information about how contact patch and Kalker's coefficients are calculated in Universal Mechanism.
- UM considers a massless rail element and its deflections in simulations. However, in this doctoral study, rigid rails are assumed.

Firstly, same simulation scenario is defined for each model. It is assumed that an unsuspended wheelset is located initially with a 3 mm lateral shift on the rails with a constant forward velocity (10 m/s). It should be noted that hunting motion of a wheelset is always unstable as stated by (Pombo et al., 2007). However, if the effect of spin on the lateral creep force is neglected, hunting motion can be stable in simulations. In 2 DOF

wheelset dynamic model, Polach's creep force model without spin creepage presented in Section 3.3.5 is used. In UM MBS tool, Polach's creep force model does not exist. However, similar analytical and simplified model, namely Mueller's method (UM, 2016), which also does not consider spin, is implemented. Details about this analytical method can be found in the user manual by (UM, 2016). The comparison of lateral dynamic responses between UM MBS model with Mueller's method and this doctoral study can be seen in Figure 4.13, 4.14, 4.15.

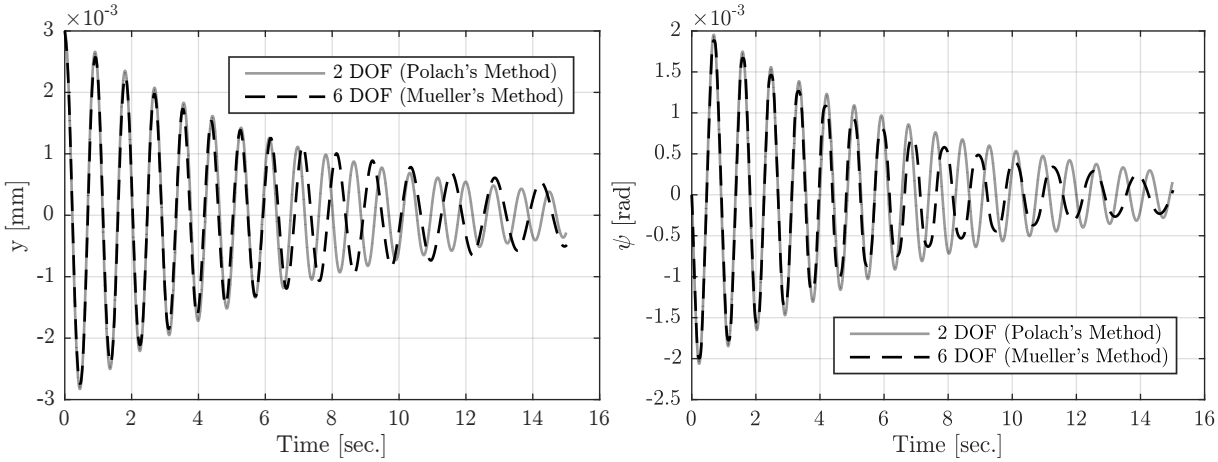

(a) Lateral shift **(b)** Yaw angle

Figure 4.13: Lateral shift and yaw angle - comparison between 2 DOF model of this study and 6 DOF UM model using Mueller's creep force model

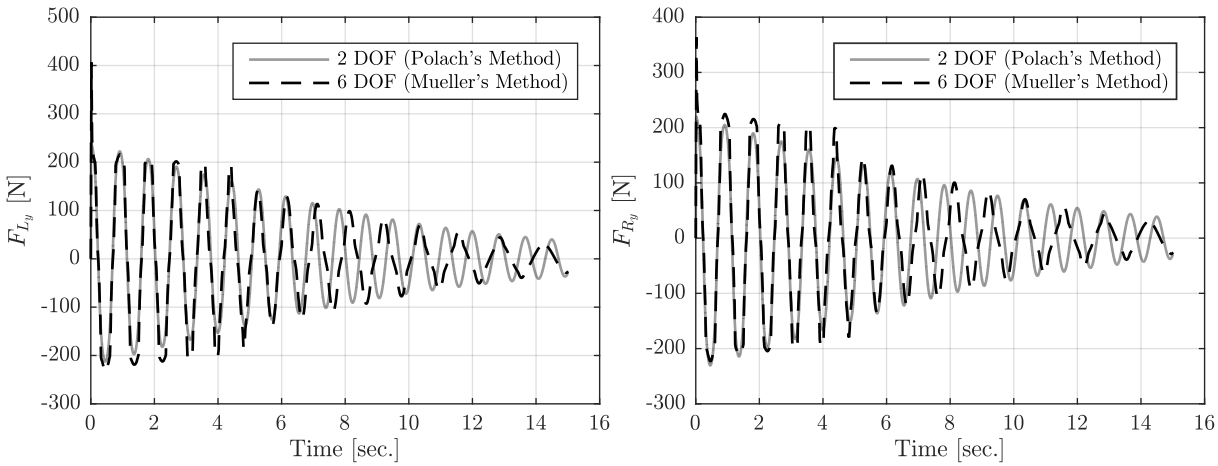

(a) Lateral Creep Force - Left Wheel **(b)** Lateral Creep Force - Right Wheel

Figure 4.14: Lateral creep forces at left and right wheel - comparison between 2 DOF model of this study and 6 DOF UM model using Mueller's creep force model

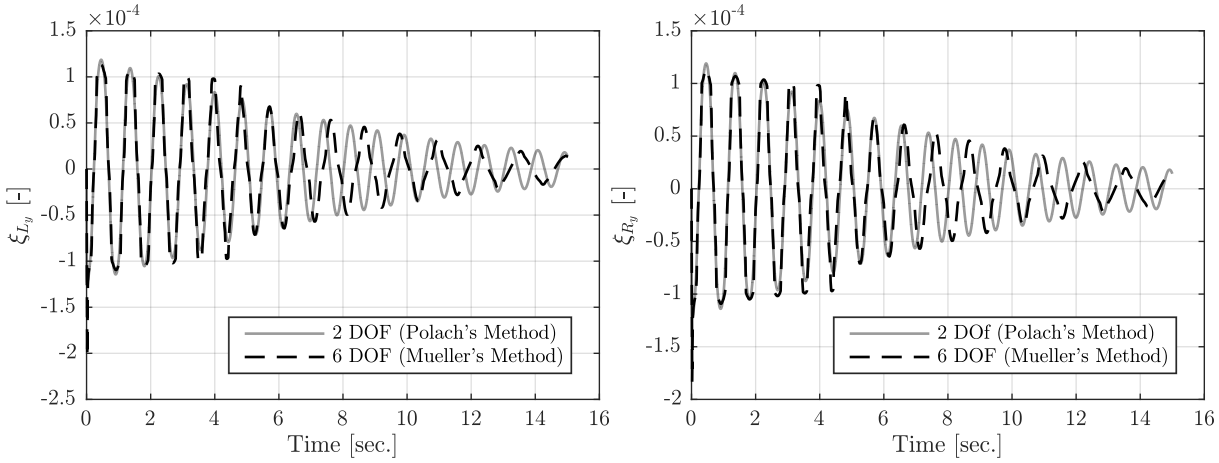

(a) Lateral Creepage - Left Wheel **(b)** Lateral Creepage - Right Wheel

Figure 4.15: Lateral creepages at left and right wheel - comparison between 2 DOF model of this study and 6 DOF UM model using Mueller's creep force model

It is concluded that different contact search methods, other DOF considered by (UM, 2016) and different creep force models cause slightly different lateral dynamic response as seen in Figure 4.13. However, comparison reveals that 2 DOF freedom lateral dynamic model of an unsuspended wheelset is able to catch lateral and yaw dynamics of a 6 DOF wheelset model. The trend in two responses are same and both responses have tendency to decrease. Additionally, this comparison demonstrates that the hunting motion of unsuspended wheelset is stable if creep force models without considering spin are used. In the proceeding case, both models use Fastsim as creep force model with spin. Thus, the hunting motion of the unsuspended wheelset becomes unstable. Results are given in Figure 4.16, 4.17, 4.18. Unlike the previously presented results, there occur a flange contact when Fastsim is considered with spin as creep force model. In the user manual by (UM, 2016), it is indicated that for flange contact UM considers the effect of overswing (i.e. the longitudinal coordinate of the flange contact for nonzero value of the yaw angle), whereas it is not considered in this doctoral study. Previously mentioned reasons are valid for the differences in dynamic response in the second part which Fastsim is used as creep force model. However similarly, it can be concluded from the comparison that 2 DOF lateral dynamic model is sufficient to track response of a 6 DOF MBS model.

In order to validate 7 DOF dynamic model presented in 3.5.2, a 1 mm vertical step

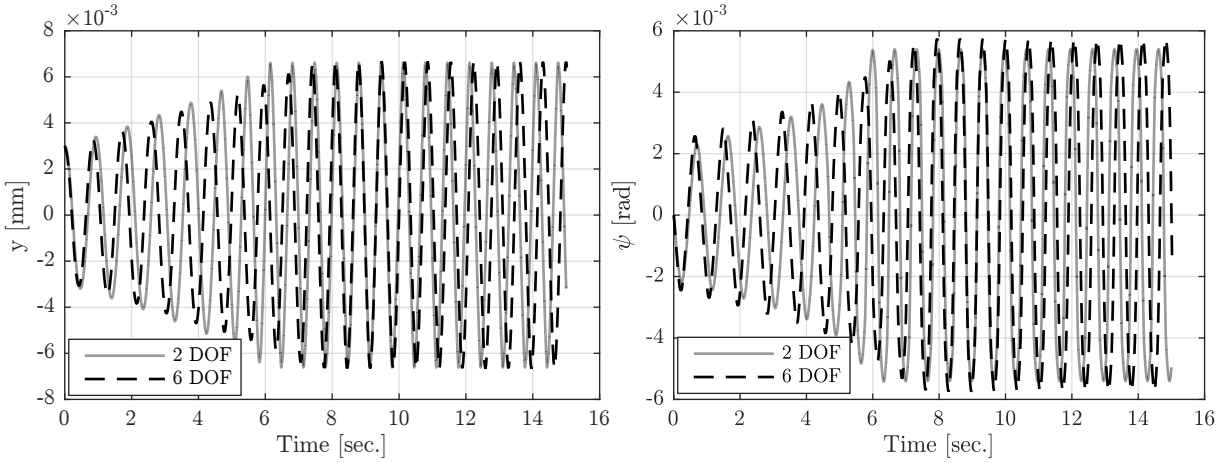

(a) Lateral shift **(b)** Yaw angle

Figure 4.16: Lateral shift and yaw angle - comparison between 2 DOF model of this study and 6 DOF UM model using Fastsim as creep force model

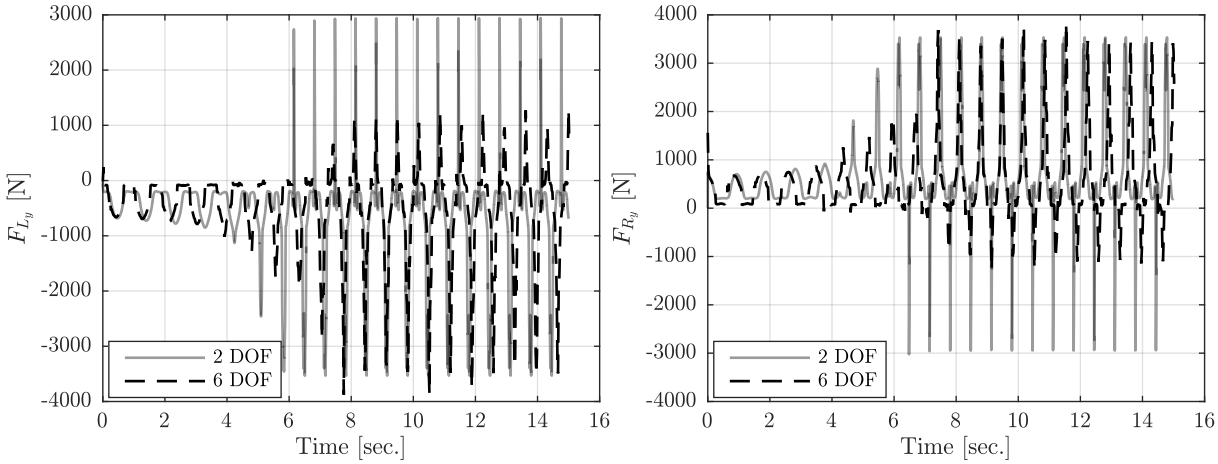

(a) Lateral Creep Force - Left Wheel **(b)** Lateral Creep Force - Right Wheel

Figure 4.17: Lateral creep forces at left and right wheel - comparison between 2 DOF model of this study and 6 DOF UM model using Fastsim as creep force model

track irregularity is applied to both bogies after 1 second. It can be seen in Figure 4.19 that both response of coach and second bogie converge to this step input value.

For the validation of the dynamic model of the tram wheel test stand explained in Section 3.5.3, angular velocity and creep force measurements are considered. Simulation scenarios are based on the calculated translational velocity of the tram wheel. Torque requests from PMSM motor are different in two cases. The torque request for the first case is demonstrated in Figure 4.21. In the second case, torque profile is same, but the

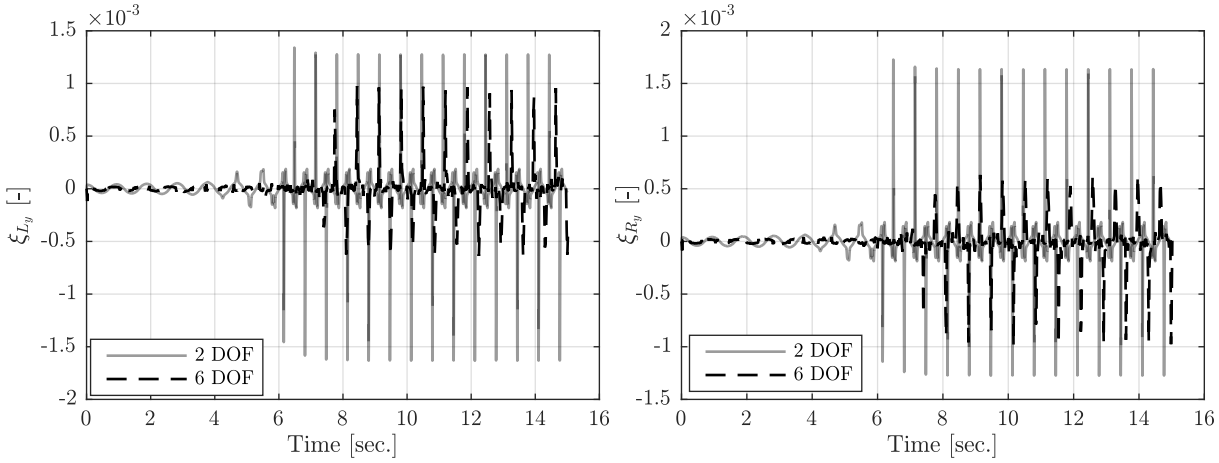

(a) Lateral Creepage - Left Wheel **(b)** Lateral Creepage - Right Wheel

Figure 4.18: Lateral creepages at left and right wheel - comparison between 2 DOF model of this study and 6 DOF UM model using Fastsim as creep force model

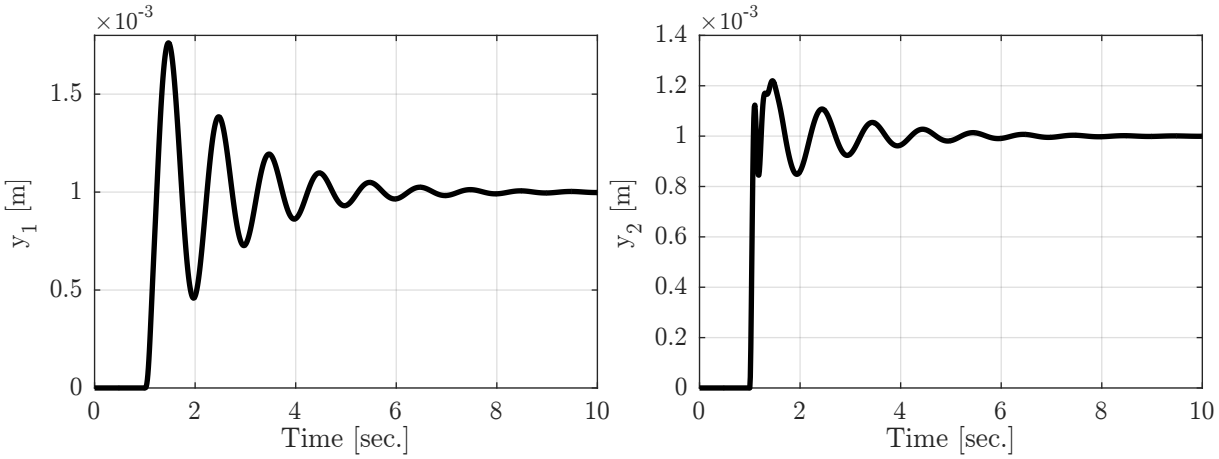

(a) Dynamic response of the coach **(b)** Dynamic response of the bogie

Figure 4.19: Step responses of a bogie and coach in 7 DOF model given in Section 3.5.2

maximum torque transmitted to the wheel is 852 N and this value is the limit for the PMSM torque that can be exerted on wheel. In these scenarios, the system proceeds without traction for first and last 5 seconds. Initially, the asynchronous motor attached to the roller is controlled and adjusted to operate at synchronous frequency of 7.5 Hz for the first simulation scenario and 15 Hz for the second one, which are almost equal to the 15 km/h and 30 km/h translational velocity for the wheel in real case. The asynchronous motor applies a counter torque which is proportional to the slip in the motor and given in Equation 3.110. Initial angular velocities for wheel–roller are calculated as 9.36 rad/s

and 12.16 rad/s for the first case, and 18.73 rad/s and 24.33 rad/s for the second case, respectively.

During taking measurements from tram wheel test stand dry surface conditions are considered. The variable friction model, which is reported by (Polach, 2005), is used in the simulations. In this model, adhesion is dependent on the slip velocity and it is formed by dimensionless creep and the translational velocity of the wheel. The dimensionless creep and the creep due to spin are calculated as

$$\xi_x = \frac{V_r - V_w}{V_r}, \tag{4.1}$$

$$\xi_s = \frac{sin\delta_w}{r_{eq_x}}, \tag{4.2}$$

where V_w and V_r are the translational velocities of the wheel–roller, respectively and δ_w is the contact angle. Unlike the real wheel–rail case, in this scheme roller also rotates. Therefore, in order to calculate the spin creepage, an equivalent radius r_{eq_x} should be considered and can be given as:

$$\frac{1}{r_{eq_x}} = \frac{1}{r_{w_x}} + \frac{1}{r_{r_x}}, \tag{4.3}$$

where r_{w_x} and r_{r_x} are the rolling radii of the wheel and roller, respectively. The slip velocity simply equals to $w = \xi_x \times V_w$ and friction coefficient can be given as:

$$\mu = \mu_0 \left[(1 - A)\, e^{-Bw} + A \right], \tag{4.4}$$

where μ_0 is the maximum friciton coefficient, w is the magnitude of the slip velocity, B is the coefficient of exponential decrease and A is the ratio of limit friction coefficient μ_∞ to μ_0. By using previous knowledge from experimental study for dry conditions, μ_0, A, B is selected as 0.4, 0.4 and 0.6, respectively. Comparison of the model w.r.t. the adhesion measurement can be found in Figure 4.20.

Simulation results and measurements for system states (i.e. angular velocities) are presented in Figure 4.22 and Figure 4.23 for the first and second simulation scenarios,

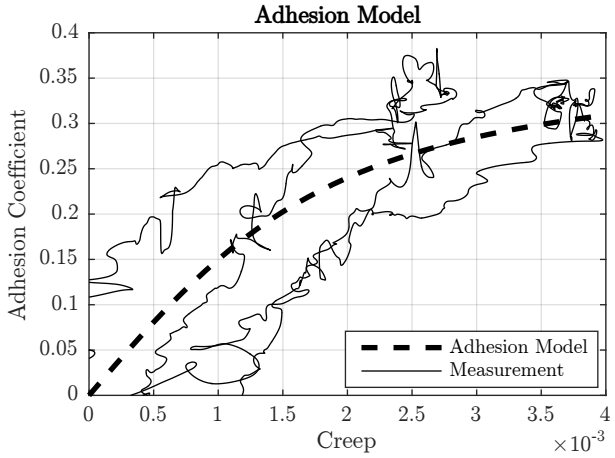

Figure 4.20: Adhesion model for tram wheel test stand

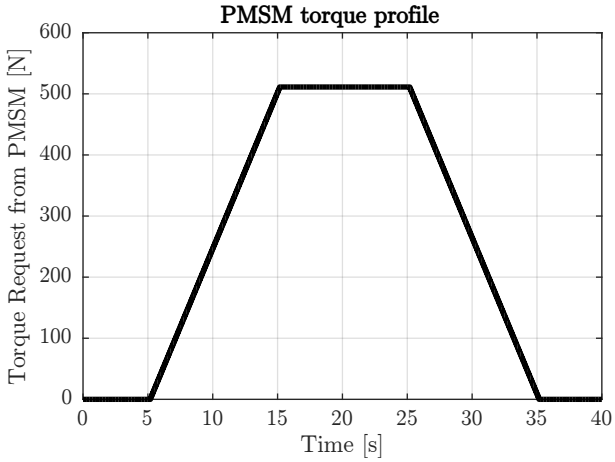

Figure 4.21: Torque request from PMSM

respectively. It is clear that simulation results are in very good agreement with measurements. However, increasing dynamic effects due to the modelling errors at higher speed deteriorates the results. Simulations include error during maximum traction in this case. Nevertheless, It can be seen from the Figure 4.23 that the error is at an acceptable level. For the first and second simulation scenario, the comparison of the results of the Fastsim algorithm w.r.t the measured creep force by using the torque transducer can be found in Figure 4.24.

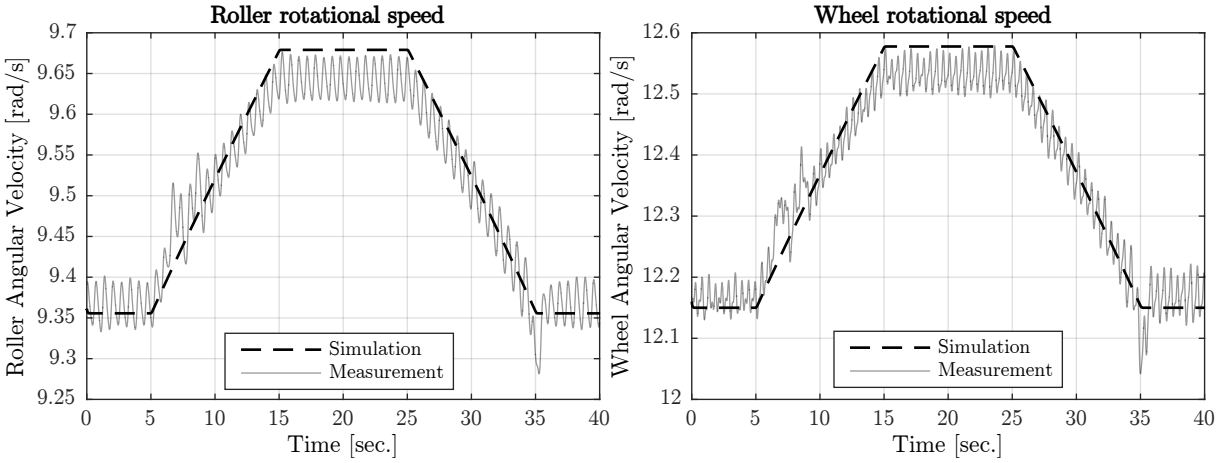

(a) Rotational speed of the roller **(b)** Rotational speed of the wheel

Figure 4.22: Comparison of simulations and measurements for tram wheel test stand at 15 km/h translational velocity

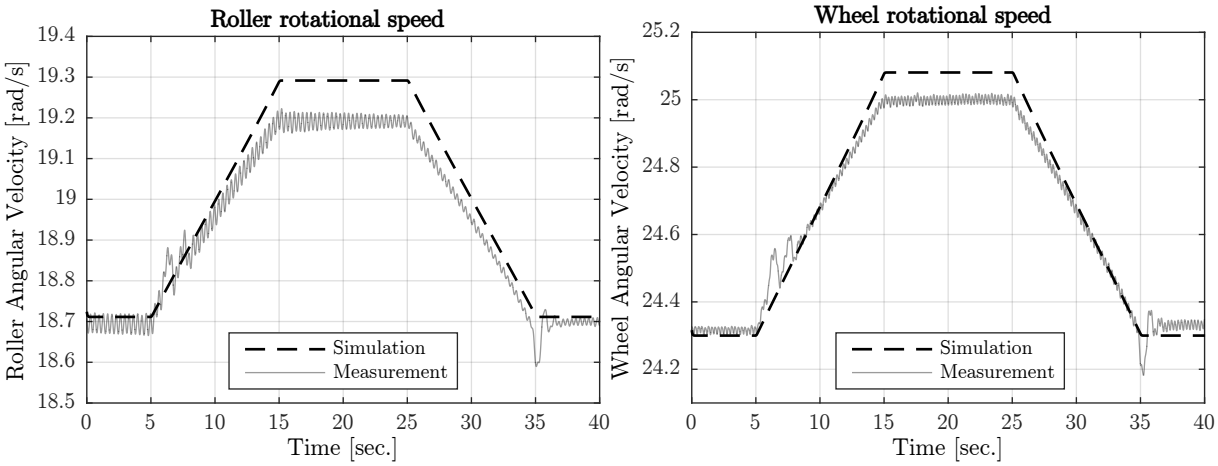

(a) Rotational speed of the roller **(b)** Rotational speed of the wheel

Figure 4.23: Comparison of simulations and measurements for tram wheel test stand at 30 km/h translational velocity

4.6 Results for Parameter Estimation and Filtering Scheme

4.6.1 Friction Condition Estimation Scheme

In order to monitor friction condition in straight track sections, an estimation methodology is proposed. To the author's knowledge, the present work is the first one step estimation scheme proposed in related literature by using a joint unscented Kalman filter for estimation of maximum friction coefficient from the dynamic response of a

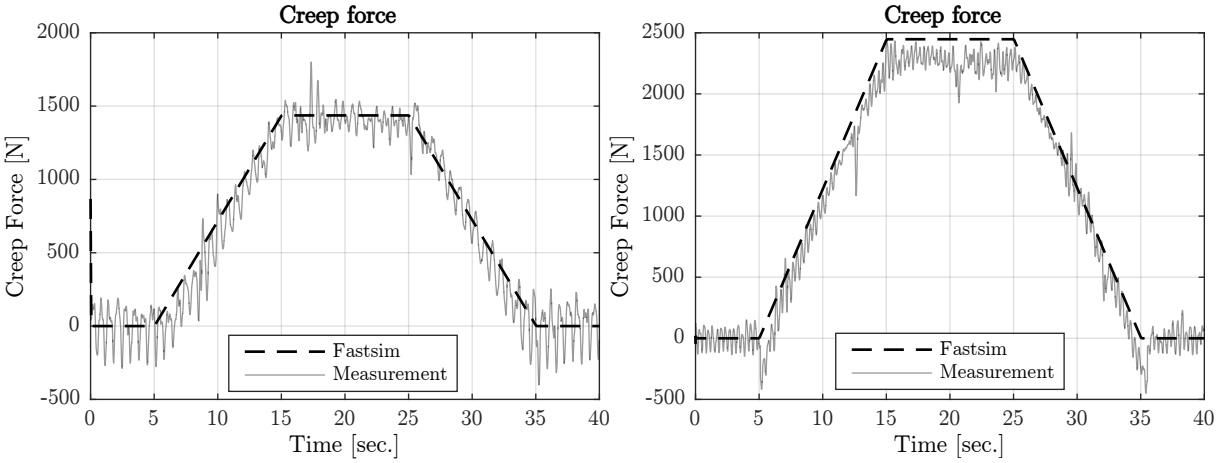

(a) First simulation scenario – 15 km/h **(b)** First simulation scenario – 30 km/h

Figure 4.24: Comparison of simulations using Fastsim creep force model and creep force measurement from tram wheel test stand for first and second simulation scenarios

Table 4.1: Parameters for friction conditions

Parameters	Definitions	Dry	Wet	Low	Very low
μ_0	Maximum friction coefficient at zero slip velocity	0.5	0.2	0.08	0.04
A	Ratio of friction coefficients μ_∞/μ_0	0.4	0.4	0.4	0.4
B	Coefficient of exponential friction decrease (s/m)	0.6	0.2	0.2	0.1
k_A	Reduction factor in the area of adhesion	1	1	0.6	0.3
k_S	Reduction factor in the area of slip	0.4	0.4	0.2	0.1

wheelset. This methodology is based on the interpretation of lateral and yaw dynamic response of a wheelset for different friction conditions. Friction coefficient model given in Equation 4.4 is used for estimation purpose along with the Polach's creep force model. Four friction conditions are defined. These are named as dry, wet, low and very low friction conditions according to the friction level and parameters defining these friction conditions are provided in Table 4.1. Measurements show that initial gradient of creep force–creep curve decreases with decreasing friction condition. Therefore, in order to be consistent with the real situation, different reduction factors k_A and k_s are selected with decreasing friction condition.

In related European standards critical friction condition levels are defined for braking. 0.15 friction coefficient is a limit (generally with some exceptions) in the design

of braking systems across the Europe such that braking must be achieved above 0.15 friction coefficient value as reported in the article 4.2.4.6.1 of European standard (EN, 2014).

In order to reveal how dynamic response of the wheelset changes w.r.t. different friction conditions, lateral and yaw dynamic response of the wheelset are illustrated with respect to a 5 mm step input under different maximum friction coefficient conditions. Step input defines the instantaneous change in the lateral alignment of the track with a magnitude of 5 mm. During simulations, 2 DOF wheelset model explained in previous section is used with connections to a bogie (considered as a suspended mass during simulations and expression is given in Equation 3.104) by suspension elements . Step input is applied after 1 second and in Figure 4.25, dynamic responses of the wheelset w.r.t. the different friction conditions with same lateral alignment irregularity are provided. Since the wheelset has a unique dynamic response for each friction condition, it is concluded that maximum friction coefficient can be estimated at one step by using a model based filtering method based on UKF. (Hubbard et al., 2014) also report similar responses for different friction coefficients and also a decrease in yaw angle w.r.t. decreasing friction coefficient is observable in the study by (Hubbard et al., 2014).

State vector for estimation purpose is given by

$$\hat{x} = \begin{bmatrix} \hat{y} & \hat{\psi} & \dot{\hat{y}} & \dot{\hat{\psi}} & \hat{\mu}_0 \end{bmatrix}. \tag{4.5}$$

It is stated by (Ward et al., 2012) and (Hubbard et al., 2013, 2014) that all states of wheelset dynamics are necessary for estimation. Therefore, wheelset states given in Equation 4.5 are required as measurements. Especially, these data could be derived from accelerometers and yaw gyros, (Hubbard et al., 2013). Such a method is given for estimating rail irregularities by (Kawasaki and Youcef-Toumi, 2002). This method is an alternative that can be used for deriving positions and velocities of a wheelset. Therefore, derivation of positions and velocities from accelerometers and yaw gyros is not investigated in this doctoral work. In addition to the state vector, output vector (i.e. measurements

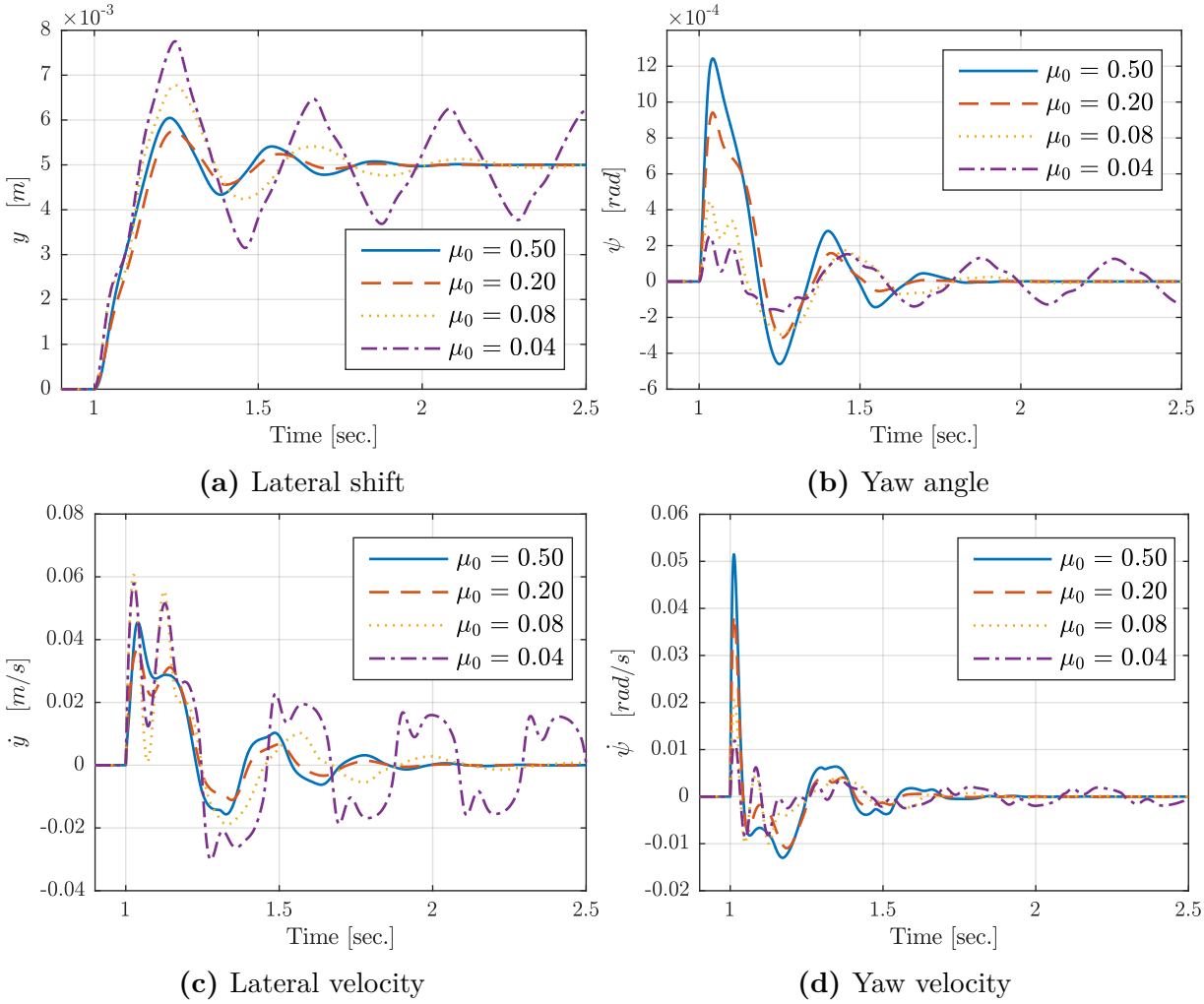

(a) Lateral shift **(b)** Yaw angle

(c) Lateral velocity **(d)** Yaw velocity

Figure 4.25: Dynamic response of the wheelset for different friction conditions

vector) is defined as

$$y_{out} = \begin{bmatrix} y & \psi & \dot{y} & \dot{\psi} \end{bmatrix}. \tag{4.6}$$

Simulation study is carried out by using UKF. Firstly, so called static tests are given. The word static means that no friction change in the wheel–rail interface exists. The friction conditions, which are demonstrated in Table 4.1, are used in simulations. Furthermore, track irregularity data mentioned in Section 3.4 is considered along with the wheelset parameters provided in Table 3.4. For static tests, initial conditions for states are same and equal to zero. Initial parameter estimates $\hat{\mu}_0 = \begin{bmatrix} 0.10 & 0.15 & 0.15 & 0.40 \end{bmatrix}$

are selected w.r.t. the real friction conditions $\mu_0 = \begin{bmatrix} 0.04 & 0.08 & 0.20 & 0.50 \end{bmatrix}$. Furthermore, the filter parameters α which is used to determine distribution of sigma points, κ the secondary scaling parameter, and β a non–negative weight incorporating prior knowledge of state distribution are taken 0.5, 0 and 2, respectively. Initial covariance matrix, process and measurement noise matrices are given by

$$P_0 = \begin{bmatrix} 10^{-3}, & 10^{-3}, & 10^{-3}, & 10^{-3}, & 0.5 \end{bmatrix}, \tag{4.7a}$$

$$Q = \begin{bmatrix} 10^{-3}, 10^{-3}, 8 \times 10^{-4}, 8 \times 10^{-4}, 1.6 \times 10^{-1} \end{bmatrix}, \tag{4.7b}$$

$$R = \begin{bmatrix} 10^{-8}, 10^{-8}, 10^{-8}, 10^{-8} \end{bmatrix}. \tag{4.7c}$$

It has been observed that for dry and low friction conditions, parameter term of the state vector can be unrealistic. This is due to some sigma points either include very high level of maximum friction coefficient estimates at dry conditions or very low level of maximum friction coefficient estimates (even negative values) at low and very low friction conditions. In order to prevent this unrealistic situation, the box constraint mentioned by (Kandepu et al., 2008) is applied to parameter estimate. Parameter estimate is controlled with respect to the box constraint which can be expressed as

$$0.01 \leq \hat{\mu}_0 \leq 0.60. \tag{4.8}$$

These limits for the maximum friction coefficient are the realistic limits which correspond to the operational situation in wheel–rail interface. Results for static tests are revealed in Figure 4.26. It is concluded that the estimator provides good estimation of the friction levels. There is no significant differences between estimates and real values. However, estimator has a difficulty to converge exact values of the parameter due to the similar dynamic responses for close friction coefficients in magnitude (e.g. for 0.45 and 0.5). Such situation is also reported in Figure 10 of previous study by (Hubbard et al., 2014). Furthermore, in order to interpret outputs of static tests clearly, a moving average window can be used to eliminate drifts in the parameter estimate, (Ward et al., 2012).

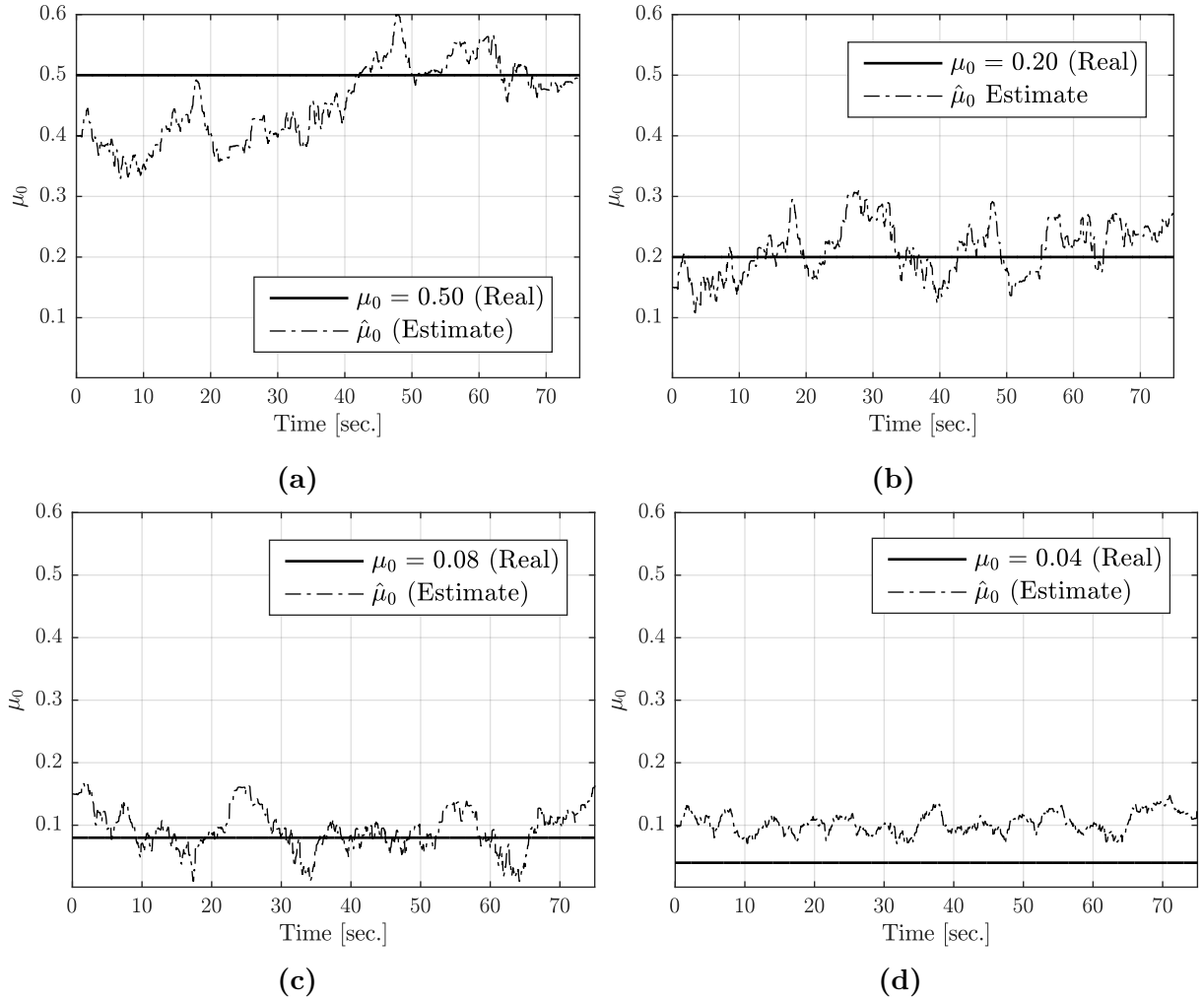

Figure 4.26: Estimation results for different friction conditions in static case

Due to the considered reduction factors k_A and k_S, hunting motion of the wheelset is almost unstable for very low friction condition (i.e. $\mu = 0.04$) and this situation causes a performance deterioration in estimation performance combined with the structure of the joint unscented Kalman filter. Error is equally shared among the states and the parameter because of the structure of joint unscented Kalman filter as stated by (Matzuka et al., 2012). This is observable in Figure 4.26d. Nevertheless, estimator is sufficient to determine the friction condition which is under the critical friction level for braking ($\mu = 0.15$) mentioned previously.

Inspection of results from figures can be deceptive for such estimation schemes. Therefore, a performance measure different from visual inspection should be considered.

The performance measures for family of Kalman filters can be found in textbook by (Haug, 2012). In this doctoral study, root mean squared error is used as the performance measure. Root mean squared error can be given as

$$e_{RMS} = \left[\frac{1}{M} \sum_{i=0}^{M} \left(\theta_i - \hat{\theta}_i \right)^2 \right]^{\frac{1}{2}}, \tag{4.9}$$

where θ represents the parameter (i.e. μ_0) and M represents the total number of sampled points. RMSEs for different friction conditions can be found in Table 4.2. The level of RMSE in each conditions is satisfactory since the detection of very low condition is sufficient w.r.t. the critical friction coefficient value ($\mu = 0.15$) indicated in standards for braking. RMSE levels indicate that estimation scheme based on joint UKF is promising.

Table 4.2: RMSE values for static tests

	Dry	Wet	Low	Very low
Root mean squared errors	0.0781	0.0457	0.0367	0.0654

Estimator must be able to adapt itself to a change in friction conditions. Accordingly, step change tests are carried out and results are presented in Figure 4.27. The word step refers to the instantaneous change in friction conditions in the wheel–rail interface. Initially, all conditions and covariance matrices for the step change in friction tests are same as they are in static tests. The difference is that at $t = 20$ seconds the maximum friction coefficient changes from dry and wet conditions to low and very low friction conditions. Additionally, for the first 20 seconds, the results for dry and wet conditions in step change tests are same as the cases in static tests. It is shown in Figure 4.27 that estimator achieves adaptation from dry and wet conditions to low and very low friction conditions. Most significantly, estimator is robust against the change in other parameters of the creep force and adhesion model. With decreasing friction conditions, ratio of friction coefficients (μ_0/μ_∞) A, coefficient of exponential friction decrease B, reduction factors k_A and k_S decrease as well, but estimator starts with the knowledge of these parameters for dry and wet conditions and the information about these parameters for low and very low friction conditions are not provided. In other words, after 20 seconds these parameters also change, whereas no data about these changes is given to estimator.

Even in such condition, estimator is robust against the change in other creep force and friction model parameters.

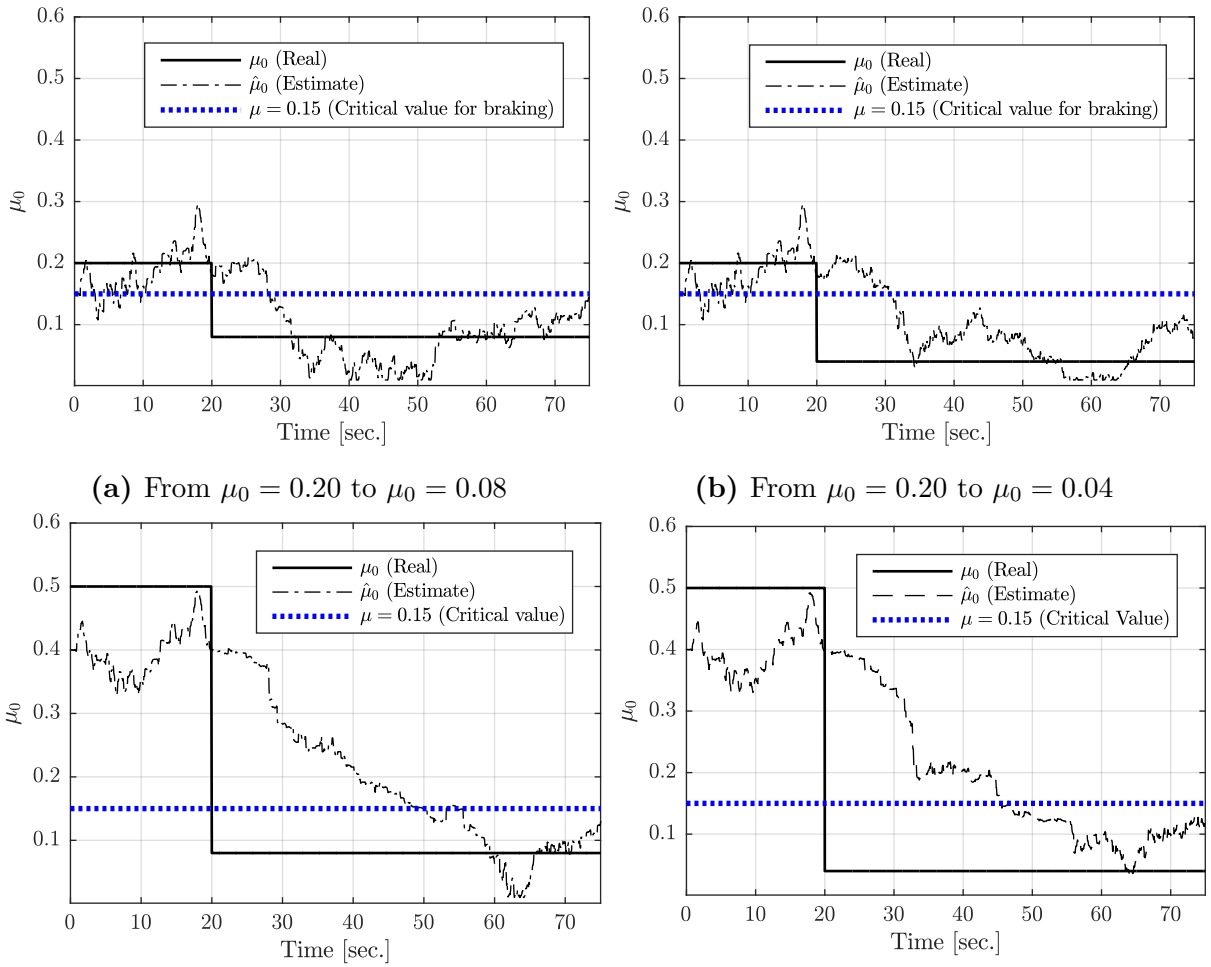

(a) From $\mu_0 = 0.20$ to $\mu_0 = 0.08$

(b) From $\mu_0 = 0.20$ to $\mu_0 = 0.04$

(c) From $\mu_0 = 0.50$ to $\mu_0 = 0.08$

(d) From $\mu_0 = 0.20$ to $\mu_0 = 0.04$

Figure 4.27: Estimation results for different friction conditions in step change case

Response of the estimator in step change tests may be criticized. Degradation in performance is because of the structure of the joint unscented Kalman filter. The joint method is distributing the error equally among the states and the parameter, and can pass it back and forth, (Matzuka et al., 2012). This causes estimator to operate with lag and drifts in parameter estimation. A dual filter can operate better, but dual filter requires estimation of parameter by using another filter, which means post processing of states, and it is not desirable in this study. However, if the critical value of friction coefficient ($\mu = 0.15$) for braking is taken as an indicator, the performance of the estimator

is considered as sufficient. In case of change from dry to low and very low conditions, estimator reaches the critical value of friction coefficient approximately 25 seconds later after the step change. When the translational velocity of the vehicle (40 m/s) is taken into account, the distance for having information about critical level is equal to 1000 meters. It is a well-known fact that in case of high speed trains, braking distances can be up to 3000 meters. Therefore, the response is sufficient enough to alert driver and/or decision makers to take necessary actions within the braking distance of high speed trains in operation.

4.6.2 Estimation of Primary Suspension

Same estimation scheme based on UKF, which is used in previous section, is considered. In this section, the contact model is different from the previous section and the method reported in Section 3.2.2 is used. Additionally, two parameters are different from the ones provided in Table 3.4, which are normal load for each wheel $F_N = 50$ kN and primary lateral spring stiffness $k_y = 3 \times 10^6$ N/m. Output vector in this scenario is same as given in Equation 4.6. State vector for estimation of primary spring coefficient can be expressed as

$$\hat{x} = \begin{bmatrix} \hat{y} & \hat{\psi} & \dot{\hat{y}} & \dot{\hat{\psi}} & \hat{k}_y \end{bmatrix}. \tag{4.10}$$

In order to test estimation scheme, again static and step change estimation scenarios are presented. Firstly, initial guess of the parameter is selected far from the real values. Secondly, it is assumed that a step change occurs in spring constant of primary suspension due to a malfunction. In the static estimation case, initial guess for the total spring constant of lateral suspension is 4×10^6 N/m, whereas the real value is 6×10^6 N/m. For the step change case, real value of the total lateral spring value is assumed to drop from 6×10^6 N/m to 4×10^6 N/m after 20 seconds. It is concluded that estimation scheme works sufficiently to detect dramatic changes in primary suspension which can occur during operation. Results are provided in Figure 4.28.

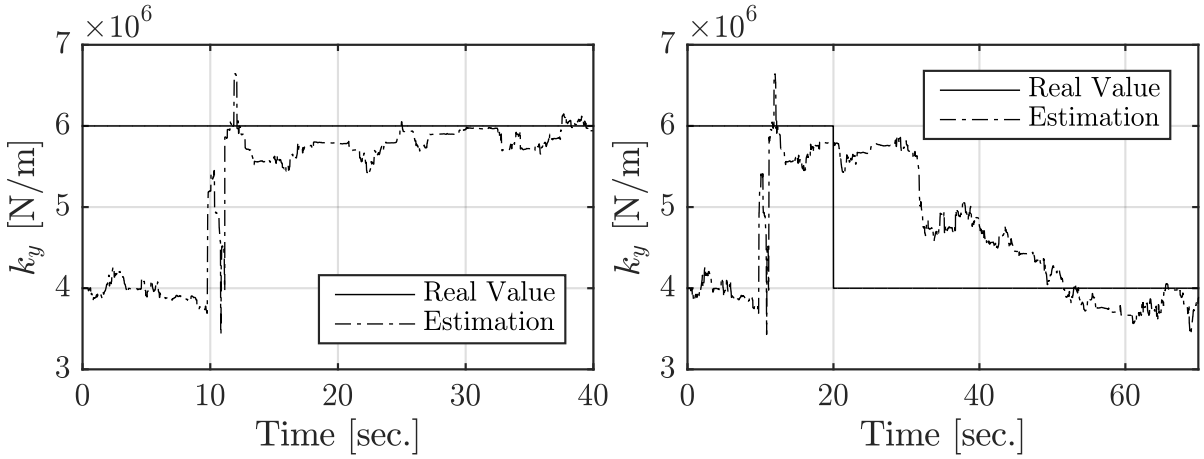

(a) Estimation - static case **(b)** Estimation - step change case

Figure 4.28: Results for primary lateral suspension estimation

4.6.3 Estimation of Secondary Vertical Suspension

The results given in this section are also presented in the study by (Onat et al., 2016a). Unlike the previous sections, the linearised model presented in Section 3.5.2 is used. For estimation purpose, Equation 3.108 can be written in the form

$$\dot{\mathbf{x}}_{red} = -\mathbf{M}_{red}^{-1}\mathbf{K}_{red}\mathbf{x}_{red} + \mathbf{M}_{red}^{-1}\mathbf{T}_b\dot{\mathbf{u}} + \mathbf{M}_{red}^{-1}\mathbf{T}_k\mathbf{u} + \mathbf{q}, \tag{4.11a}$$

$$\mathbf{y}_{out} = \mathbf{C}\mathbf{x}_{red} + \mathbf{r}. \tag{4.11b}$$

Equation 4.11 is in the form of Equation 3.112 and Kalman filter is applied for state estimation in this case. State vector contains the estimates of the terms given in Equation 3.109. Unlike the measurement vector given in a previous similar study by (Xu et al., 2015), which includes the measurements of deformations of suspensions; it is assumed that the measurements are simply taken from low cost inertial sensors (e.g. accelerometers and gyros) and this measurement vector can be given as

$$\mathbf{y}_{out} = \begin{bmatrix} \ddot{y}_1 & \dot{\phi}_{z1} & \dot{\phi}_{x1} & \ddot{y}_2 & \dot{\phi}_{x2} & \ddot{y}_3 & \dot{\phi}_{x3} \end{bmatrix}. \tag{4.12}$$

In this doctoral study, a concurrent state estimation, which time update and

measurement update occur simultaneously, is considered. Thus, only a posteriori covariance estimate, which is expressed in Equation 3.129, is calculated. Discretization step size in this case is 10 milliseconds.

Due to the structure of linear Kalman filter, parameter estimate can not be incorporated into the state vector. Therefore, a parameter estimation scheme for this case is necessary. In parameter estimation, aim is to find optimal parameter which give the best fit between measurements and estimates as emphasized by (Matzuka et al., 2012). A weighted least squares approach is considered in this section as a cost function. Cost function can be given in the form

$$J(\theta) = \sum_{k=1}^{n} \gamma_k \left(\mathbf{y}_{out} - \mathbf{y}_{model} \right), \tag{4.13}$$

where γ_k is the weighting parameter and $(\mathbf{y}_{out} - \mathbf{y}_{model})$ is the so called residuals. Weighting parameter vector is decided by inspection in simulations. Simulations reveal that most influential residuals are the vertical acceleration and roll rate of the body of the coach. Therefore, these two residuals have the 70% of the weight and other residuals have the rest of the weight equally. In simple form, parameter estimation is carried out by the expression

$$\theta_k = \theta_{k-1} + \beta_p J(\theta), \tag{4.14}$$

where β_p is a parameter to interpret sum of residuals and it is equal to 1.5×10^6. This parameter is also determined by inspection of the simulation results.

The choice of initial covariance matrix is intuitive, whereas process and measurement noise covariance matrices depend on the accuracy of the mathematical model and the statistical properties of the noise and accuracy of used sensors, respectively. Initial covariance matrix is determined as a diagonal matrix which has the same size of state vector and each diagonal is equal to 0.01. Process noise covariance matrix is selected similar to initial covariance matrix which has the same size of state vector and each diagonal is equal to 0.001. Measurement noise covariance matrix is selected as a diagonal matrix which has the same size of measurement vector and each diagonal is equal to 1.

Similar to the previous sections, firstly, a static estimation scenario is presented. The value of k_1 is given in Table 3.5. In estimation scenario, it is assumed that initial guess of the parameter estimate $\hat{k}_1$ is equal to 330×10^3 N/m. It can be clearly seen in Figure 4.29 that parameter estimate converges to real value. In the second estimation scenario with same initial condition selection as it is in first scenario, it is assumed that at $t = 20$ seconds a malfunction occurs and real value of the vertical secondary suspension decreases to the 50%. Even under these circumstance, estimation scheme is promising and sufficient to detect a dramatic change in the vertical suspension.

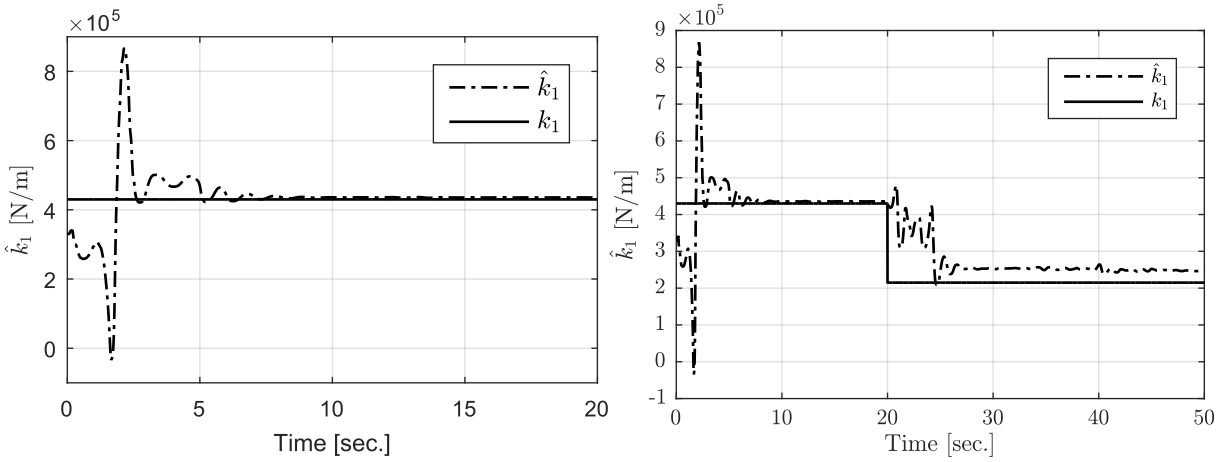

(a) Estimation - static case **(b)** Estimation - step change case

Figure 4.29: Results for secondary vertical suspension estimation

4.6.4 Estimation of Rolling Radius of the Wheel of the Tram Wheel Test Stand

So far, use of family of Kalman filters is investigated by considering simulations and simulated measurements. Hereby, the possibility of using such schemes for a real application is presented.

A fourth order Runge-Kutta numerical integration method with 0.25 ms time step is used. State vector for the tram wheel test stand is given by

$$\hat{x} = \begin{bmatrix} \hat{\omega}_w & \hat{\omega}_r & \hat{r}_{w_x} \end{bmatrix}, \tag{4.15}$$

and output vector (i.e. measurement vector) is defined as

$$y = \begin{bmatrix} \omega_w & \omega_r \end{bmatrix}. \tag{4.16}$$

Two estimation cases for each simulation scenario, which are defined in Section 4.5 for tram wheel test stand model validation, are considered. In the first case, the rolling radius of the wheel is initially assumed (i.e. estimated) as 320 mm, whereas the measured rolling radius is approximately 348.2 mm. This case is the underestimation case. In the second case, the rolling radius of the wheel is initially assumed as 400 mm and this case is the overestimation case. These two cases are realized for the 15 km/h and 30 km/h translational velocities. Initial selection of the states are same as the ones indicated in Section 4.5. However, in the contact model only a circular contact (2.7 mm radius) without shape correction is considered. This situation also increases uncertainty of the system and it is useful to test the robustness of the estimator. Furthermore, the filter parameters α which is used to determine the distribution of sigma points, κ the secondary scaling parameter, and β a non–negative weight incorporating the prior knowledge of the state distribution are taken 1, 0 and 2, respectively. Initial covariance matrix, process and measurement noise matrices are same for all conditions and given by

$$P_0 = \begin{bmatrix} 10^{-1}, & 10^{-1}, & 10^{-3} \end{bmatrix}, \tag{4.17a}$$

$$Q = \begin{bmatrix} 10^{-5}, & 10^{-5}, & 10^{-5} \end{bmatrix}, \tag{4.17b}$$

$$R = \begin{bmatrix} 10^{-5}, & 10^{-5} \end{bmatrix}. \tag{4.17c}$$

Firstly, the effect of UKF on system states are provided and can be found in Figures 4.30 and 4.31. It should be noted that UKF provides better estimates of the angular velocities when they are compared with the results demonstrated in Figure 4.22 and 4.23 when a simulation model is considered only. Especially at 30 km/h, the effect of UKF as a data fusion algorithm is evident. By combining the mathematical model with measurements provides better results for the system.

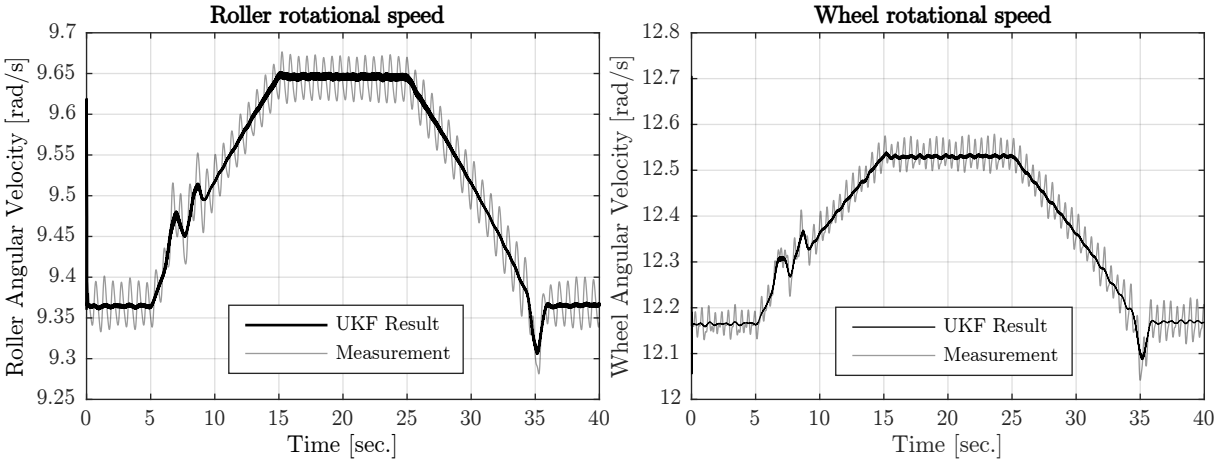

(a) Angular speed of the roller **(b)** Angular speed of the wheel

Figure 4.30: Angular speeds of the wheel–roller of the test stand at 15 km/h

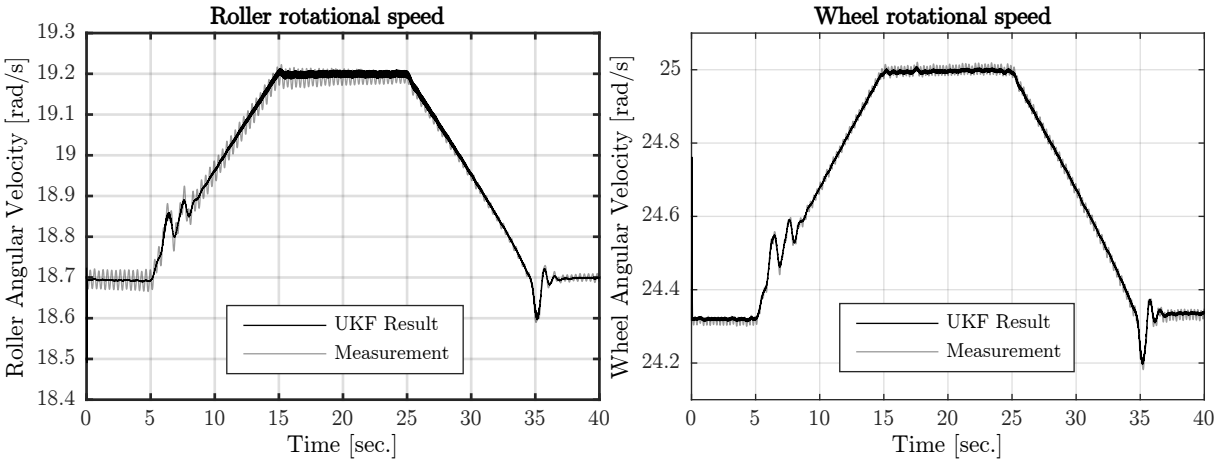

(a) Angular speed of the roller **(b)** Angular speed of the wheel

Figure 4.31: Angular speeds of the wheel–roller of the test stand at 30 km/h

Secondly, estimation results are provided. Estimation results for the first scenario (15 km/h translational velocity) are given in Figures 4.32 and 4.33. It is obvious from these figures that UKF provides very fast convergence for both underestimation and overestimation case.

Estimation results for the second scenario (30 km/h translational velocity) are demonstrated in Figures 4.34 and 4.35. It is evident from these figures that UKF again provides very fast convergence for both underestimation and overestimation case. However, the dynamic effects occured in the contact and sytem at high speed (30 km/h) due to modelling errors cause worse estimation results than the case at low speed.

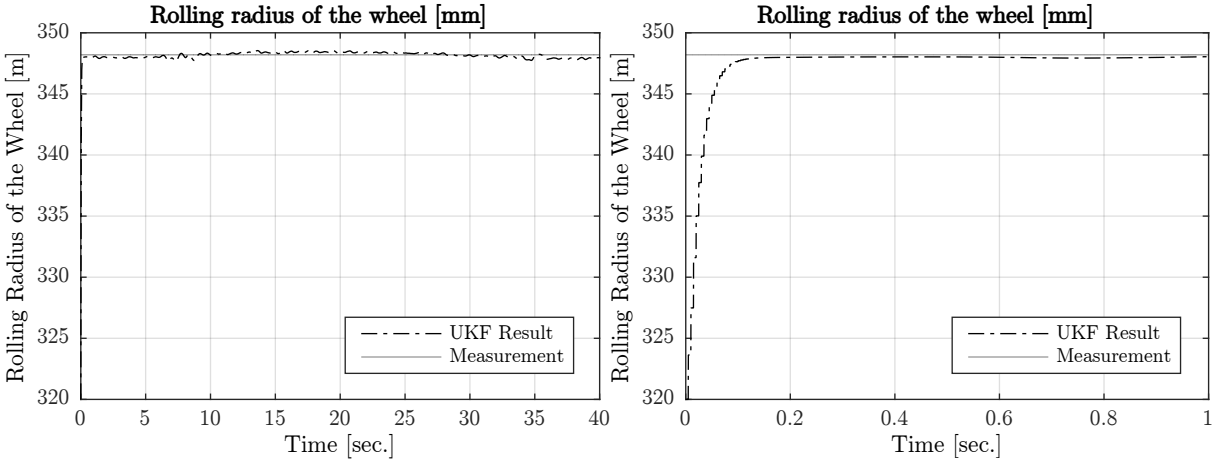

(a) Estimation between 0–40 s. **(b)** Estimation between 0–1 s.

Figure 4.32: Estimation result at 15 km/h for initially underestimated radius

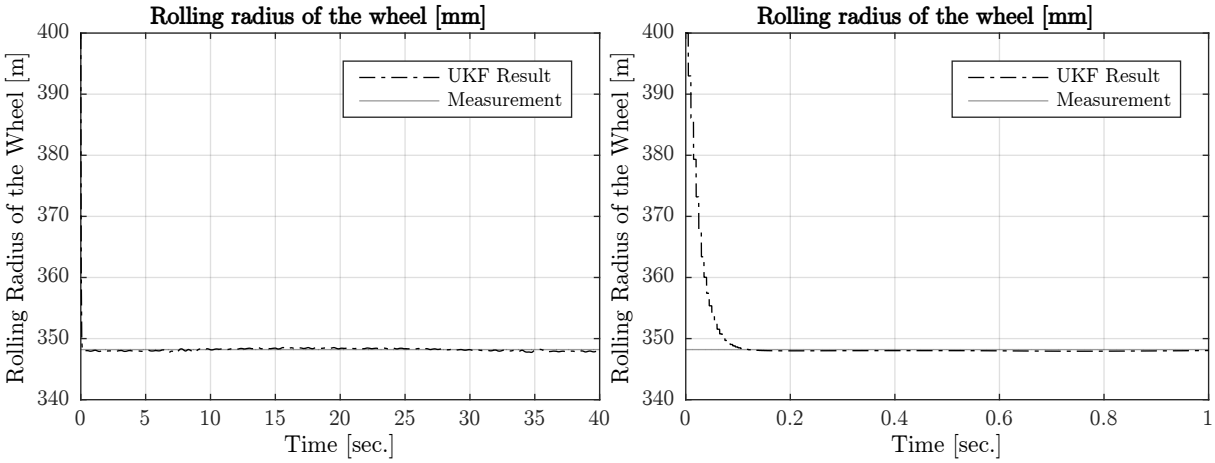

(a) Estimation between 0–40 s. **(b)** Estimation between 0–1 s.

Figure 4.33: Estimation result at 15 km/h for initially overestimated radius

The performance measure, which is defined by Equation 4.9, is considered for the estimation scheme applied on the tram wheel test stand. θ in Equation 4.9 represents the parameter (i.e. r_{w_x}) and M represents the total number of sampled points. In the first simulation scenario presented in Figure 4.32, RMSE is 0.6060 mm for underestimation case, whereas it is 1.0631 mm for overestimation case given in Figure 4.33. In the second simulation scenario provided in Figure 4.34, RMSE is 0.8233 mm for underestimation case, whereas it is 1.0139 mm for overestimation case illustrated in Figure 4.35. From the quantities of the RMSE, it can be concluded that the estimation of the rolling radius is successful by using UKF and the largest amount of the RMSE is due to the improper

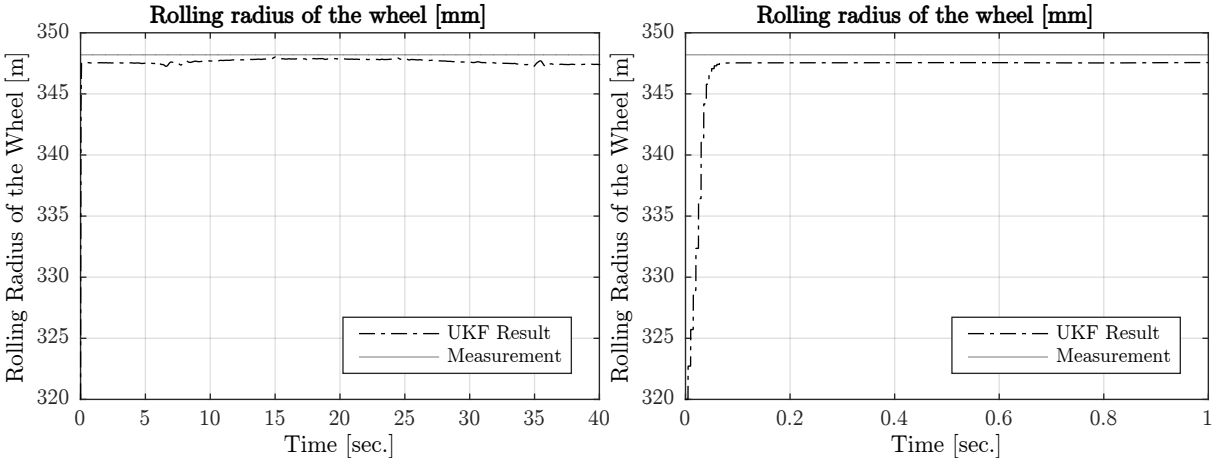

(a) Estimation between 0–40 s. **(b)** Estimation between 0–1 s.

Figure 4.34: Estimation result at 30 km/h for initially underestimated radius

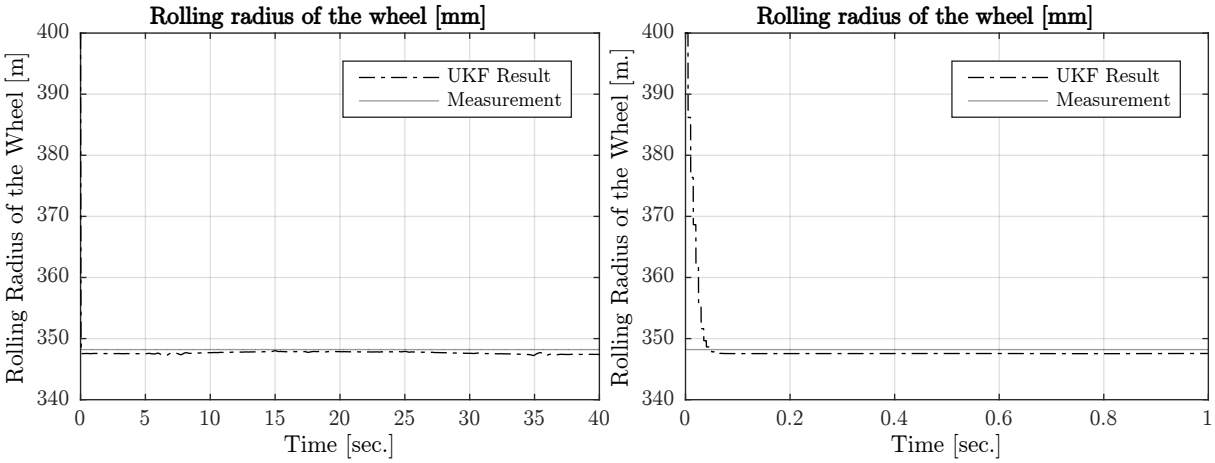

(a) Estimation between 0–40 s. **(b)** Estimation between 0–1 s.

Figure 4.35: Estimation result at 30 km/h for initially overestimated radius

selection of the initial estimates which is about 50 mm over the nominal rolling radius for overestimation case and 30 mm under the nominal rolling radius for underestimation case.

One criticism of the use of UKF for such a system is that Kalman or Extended Kalman filter can be used, instead. However, it can be seen from related equations that dynamic system is highly nonlinear in terms of system states (angular velocities). Due to this nonlinearity, the use of Kalman filter is not considerable. Extended Kalman filter requires the Jacobian matrix of the system. It can be seen in the model that obtaining a Jacobian is impossible due to the complex structure of the contact model. Therefore,

UKF is the viable alternative for this application.

Another criticism of the use of UKF can be that a least squares estimator for parameter estimation might be considered, instead. However, in the real case, as well as parameters, correct estimation of states is also essential. Especially in this case of application, estimation of the parameter along with the states eliminates inaccuracies due to state estimation since the results of the models for asynchronous electric motor and tangential solution are highly dependent on the system states (i.e. angular velocities). A joint UKF is preferred for the state and parameter estimation so that both angular velocities and rolling radius are estimated accurately at one step. Furthermore, the accurate estimation of angular velocities for real vehicles is very important such that it leads to better slip control systems and longitudinal velocity calculation of vehicles, since these systems rely upon the mathematical models and modelling errors degrades the performance of such systems.

The use of such an estimation scheme for real vehicles is not straightforward, since in the real case, there are rails instead of rollers. For locomotives, this scheme can be used just by considering torsional dynamics of the wheelset (along with the traction motor) which includes the contact model presented here. For wagons without traction, this scheme can also be considered by using torsional dynamics of a wheelset (or a torsionally flexible wheelset, (Onat et al., 2015)) and a contact model. Parameter estimation is achieved in steady rolling without traction. Traction does not affect the performance of parameter estimation. Besides, combining this scheme with the approach presented by (Charles et al., 2008b), continuous profile estimation for different lateral shifts of the wheelset can be achieved.

5 *Contributions of the Dissertation*

Contributions of the dissertation are expressed as

- Dynamic analysis of railway vehicle systems includes the solution of several problems at wheel–rail interface such as geometrical, normal, tangential problem. In this dissertation, these solution methodologies are explained in details from bottom to top so that several aspects of the wheelset and vehicle dynamics can be easily analyzed by other researchers.
- In the dynamic analysis of railway vehicle systems, wheelset is the most important part since it is the only part interacted with the rails. A dynamic model is presented so that hunting motion of the wheelset can be investigated. Comparison of the results with MBS tool UM demonstrates that the dynamic model considered here provides similar responses. The procedure, which is explained here, can be a key tool for the researchers who want to create and use their own models instead of MBS tools.
- Especially, UKF based friction condition estimation scheme given in this dissertation eliminates the need for post–processing of the states explained in the previous studies in the related literature. To the author's knowledge this methodology is the first in the related literature which identifies friction conditions without post–processing methods.
- It has shown that the estimation schemes given here are also successful to detect different parameters such as primary lateral suspension and secondary vertical suspension.
- After long operation, wear is a phenomenon occurs in the wheels of wheelsets. Wear directly influences the dynamic response of the wheelset and the vehicle, and even it can cause safety problems. Therefore, it should be continuously monitored. In this dissertation, UKF based estimation methodology is also applied to a tram wheel test stand used for research purposes in DFJP, UPCE. Rolling radius of the wheel is tried to be estimated as a parameter. By using the model and the measurements from the test stand, estimation scheme provides very good estimates in comparison with measurements. This scheme can also be used in conjuction with other systems (e.g.

slip control systems, traction control systems etc.) such that UKF as a data fusion algorithm corrects modelling errors by fusing model output and measurements. To the author's knowledge, such a methodology is new for rolling radius estimation by using just angular velocity measurements since no similar methodology is reported previously in the related literature.

- Rolling radius estimation scheme provides a demonstration that UKF is not only able to detect parameters based on simulated measurements, but also it can detect parameters based on the noisy measurements from a real operating system.

6 *Conclusion*

Condition monitoring and maintenance are important for safe and reliable transportation systems. In this doctoral work, the use of family of Kalman filters for parameter and state estimation is investigated for railway vehicles, espcially for wheelset.

In Chapter 1, a literature review is provided about the topics considered in this doctoral work. Additionally, in Chapter 2, obejectives of the study are expressed.

In Chapter 3, details of the methods and models, which are considered in this doctoral work, are presented. Firstly, the solutions to the geometrical problem of S1002-UIC60E1 wheel–rail pair and the so called W169-R169 tram wheel–roller pair are provided. Secondly, two methods for the solution of the contact search is explained. It is revealed how consideration of wheel elasticity in the contact search algorithm affects the results w.r.t. the rigid method. The theory of Hertz and virtual penetration method are used for the solution of normal problem. Results obtained hereby are compared with the results of a MBS tool, namely Gensys. The results are in good agreement and it is concluded that theory of Hertz can be used in situations which flange contact does not occur. Afterwards, the solution methods for tangential problem are mentioned. Especially, the methods proposed by Kalker are pointed out since the most modern, accurate methods are due to Kalker. Additionally, the analytical creep force model proposed by Polach is explained in details. Proceeding sections provides details of the dynamic model of a wheelset, 7 DOF vertical dynamic model of a railway vehicle and torsional dynamics model of the tram wheel test stand used in DFJP, UPCE for research purposes. Lastly, the linear Kalman filter and unscented Kalman filter are given with details.

In Chapter 4, methods and models, which are given in preceding chapter, are validated. Three validation methods are considered. Firstly, in order to validate the 2 DOF simplified dynamic model of a wheelset considered in this doctoral work, a 6 DOF freedom MBS model of wheelset is used. This MBS model is created in the tool named Universal Mechanism. In terms of lateral dynamic response of the unsuspended wheelset, it is shown that all results are in almost in perfect agreement. However, there are a slight differences because contact search algorithms used in UM and here are completely different. For the 7 DOF vertical dynamic model of a railway vehicle, it is investigated

that whether this model is sufficient to track a step input or not. Simulations reveal that this dynamic model achieve to respond a step input properly. As expected, for the torsional model of the tram wheel test stand, measurements are used for validations. The conclusion for this validation is that for low speed (15 km/h) results are in very good agreement, whereas for higher speed (30 km/h) dynamic effects due to modelling errors become evident. However, even for high speed results are promising.

Proceeding sections of the Chapter 4 illustrates estimation results. Firstly, it should be emphasized that low friction conditions in rail vehicle systems is a problem as they can cause problems in accelerating and braking which are the possible reasons of wear, instability of vehicle and unpredictable delays in schedule. The identification of such conditions is therefore essential. For straight track and constant velocity conditions, a friction condition estimation methodology based on UKF is proposed. The novelty of a joint UKF based estimation is that it eliminates the post-processing methods proposed in the previous studies of the related literature. Simulations carried out here show that this estimation scheme is successful to estimate friction conditions. By using the same methodology and data, it is investigated that if primary lateral suspension condition can be detected. Simulations reveals that estimation scheme achieves to estimate primary suspension condition properly in static and step change tests. Then, by using a linear 7 DOF vehicle model and a linear Kalman filtering scheme with weighted least squares parameter estimation scheme, the possibility of identifying secondary vertical suspension is investigated. Same conclusion is made for this estimation methodology that by using the measurements from accelerometers and yaw gyros, it is possible to obtain situation of the secondary vertical suspension. Lastly, a rolling radius estimation for the tram wheel test stand is presented and by using the angular speed measurements, possibility of estimating rolling radius of the wheel is shown. As well as the good performance of the estimator, it is concluded that UKF as a data fusion algorithm provides better responses by combining the mathematical model and measurements. This estimation methodology can provide better performance of the systems such as anti–slip, traction etc. since performance of these systems highly depend on the mathematical models. Therefore, considering estimation scheme proposed here for such systems can improve

the performance. All in all, the estimation methodology proposed in this doctoral study presents promising results, and proves its value to further use it as condition monitoring tool for railway vehicles.

Appendices

A Calculation of Kalker's Coefficients

The polynomial equations for Kalker's Coefficients are provided. Here k_1, k_2, k_3 and k_4 are auxiliary variables.

$$\begin{aligned}
k_1 &= 2.3464 + 1.5443.\upsilon + 7.9577.\upsilon^2, \\
k_2 &= 0.961669 - 0.043513.\upsilon + 2.402357.\upsilon^2, \\
k_3 &= -0.0160185 + 0.0055475.\upsilon - 0.0741104.\upsilon^2, \\
k_4 &= 0.10563 + 0.61285.\upsilon - 7.26904.\upsilon^2, \\
c_{11} &= k_1 + \frac{k_2}{\left(\frac{b}{a}\right)} + \frac{k_3}{\left(\frac{b}{a}\right)^2} + \sqrt{\frac{k_4}{\left(\frac{b}{a}\right)}}.
\end{aligned} \tag{A1}$$

$$\begin{aligned}
k_1 &= 2.34641 - 0.27993.\upsilon + 0.19763.\upsilon^2, \\
k_2 &= 0.96167 + 0.52684.\upsilon + 1.22642.\upsilon^2, \\
k_3 &= -0.0160185 - 0.0126292.\upsilon - 0.0011272.\upsilon^2, \\
k_4 &= 0.10563 + 0.78197.\upsilon - 1.12348.\upsilon^2, \\
c_{22} &= k_1 + \frac{k_2}{\left(\frac{b}{a}\right)} + \frac{k_3}{\left(\frac{b}{a}\right)^2} + \sqrt{\frac{k_4}{\left(\frac{b}{a}\right)}}.
\end{aligned} \tag{A2}$$

$$\begin{aligned}
k_1 &= 0.29677 + 0.22524.\upsilon + 0.71899.\upsilon^2, \\
k_2 &= 1.01321 + 0.20407.\upsilon - 0.72375.\upsilon^2, \\
k_3 &= 0.0092415 + 0.0854262.\upsilon + 0.319940.\upsilon^2, \\
k_4 &= (8.4835 \times 10^{-4}) - (3.211 \times 10^{-3}).\upsilon \\
&\quad - (1.7484 \times 10^{-2}).\upsilon^2, \\
c_{23} &= k_1 + \frac{k_2}{\left(\frac{b}{a}\right)} + \frac{k_3}{\left(\frac{b}{a}\right)^2} + \frac{k_4}{\left(\frac{b}{a}\right)^3}.
\end{aligned} \tag{A3}$$

$$
\begin{aligned}
k_1 &= 0.72795 - 1.00202.v - 0.32695.v^2, \\
k_2 &= 0.461755 + 1.002340.v + 0.081441.v^2, \\
k_3 &= 0.023739 - 0.110640.v + 0.249008.v^2, \\
k_4 &= -0.0012999 + 0.0063653.v - 0.0129114.v^2, \\
c_{33} &= k_1 + \frac{k_2}{\left(\frac{b}{a}\right)} + \frac{k_3}{\left(\frac{b}{a}\right)^2} + \frac{k_4}{\left(\frac{b}{a}\right)^3}.
\end{aligned} \tag{A4}
$$

B Transformation Matrices between Coordinate Axes

The matrix for the transformation from the wheelset axis to the intermediate axis is defined as

$$\begin{bmatrix} i_{int} \\ j_{int} \\ k_{int} \end{bmatrix} = \begin{bmatrix} 1 & 0 & 0 \\ 0 & cos\phi & -sin\phi \\ 0 & sin\phi & cos\phi \end{bmatrix} \begin{bmatrix} i_w \\ j_w \\ k_w \end{bmatrix}. \tag{B1}$$

The matrix for the transformation from the wheelset axis to the equilibrium axis is defined as

$$\begin{bmatrix} i_{eq} \\ j_{eq} \\ k_{eq} \end{bmatrix} = \begin{bmatrix} cos\psi & -cos\phi sin\psi & sin\phi sin\psi \\ sin\psi & cos\phi cos\psi & -cos\psi sin\psi \\ 0 & sin\phi & cos\phi \end{bmatrix} \begin{bmatrix} i_w \\ j_w \\ k_w \end{bmatrix}. \tag{B2}$$

i_{Lc}, j_{Lc}, k_{Lc} and i_{Rc}, j_{Rc}, k_{Rc} are the unit vectors which are defined for the left and right contact points, respectively. The matrices for the transformation from the left and right contact point axes to the wheelset axis are defined respectively as

$$\begin{bmatrix} i_w \\ j_w \\ k_w \end{bmatrix} = \begin{bmatrix} 1 & 0 & 0 \\ 0 & cos\delta_L & -sin\delta_L \\ 0 & sin\delta_L & cos\delta_L \end{bmatrix} \begin{bmatrix} i_{Lc} \\ j_{Lc} \\ k_{Lc} \end{bmatrix}, \tag{B3}$$

$$\begin{bmatrix} i_w \\ j_w \\ k_w \end{bmatrix} = \begin{bmatrix} 1 & 0 & 0 \\ 0 & cos\delta_R & sin\delta_R \\ 0 & -sin\delta_R & cos\delta_R \end{bmatrix} \begin{bmatrix} i_{Rc} \\ j_{Rc} \\ k_{Rc} \end{bmatrix}, \tag{B4}$$

Other transformations can be obtained by rearranging the equations and matrices provided in this appendix.

Bibliography

A. Anyakwo, C. Pislaru, and A. Ball. A new method for modelling and simulation of the dynamic behaviour of the wheel-rail contact. *International Journal of Automation and Computing*, 9(3):237–247, 2012.

M. Arnold and H. Netter. Wear profiles and the dynamical simulation of wheel-rail systems. In *Progress in Industrial Mathematics at ECMI 96*, pages 77–84. Springer, 1997.

J. Ayasse and H. Chollet. Determination of the wheel rail contact patch in semi-hertzian conditions. *Vehicle System Dynamics*, 43(3):161–172, 2005.

N. Bosso, M. Spiryagin, A. Gugliotta, and A. Somà. *Mechatronic modeling of real-time wheel-rail contact*. Springer, 2013.

N. Bosso, A. Gugliotta, and N. Zampieri. Strategies to simulate wheel–rail adhesion in degraded conditions using a roller-rig. *Vehicle System Dynamics*, 53(5):619–634, 2015.

M. Bozzone. *Dynamic analysis of railway systems using computationally efficient wheel-rail contact models*. PhD thesis, University of Rome Tor Vergata, 2009.

N. Burgelman, Z. Li, and R. Dollevoet. A new rolling contact method applied to conformal contact and the train–turnout interaction. *Wear*, 321:94–105, 2014.

O. Cernỳ, J. Šimánek, R. Dolecek, and J. Novák. Testing of robust control characteristics for traction pmsm. *PIERS2007*, pages 107–111, 2007.

G. Charles, R. Goodall, and R. Dixon. Model-based condition monitoring at the wheel–rail interface. *Vehicle System Dynamics*, 46(S1):415–430, 2008a.

G. Charles, R. M. Goodall, and R. Dixon. A least mean squared approach to wheel-rail profile estimation. In *4th IET International Conference on Railway Condition Monitoring*, 18–20 June 2008b. ISBN: 978-0-86341-927-0.

R. Doleček, J. Novák, and O. Černỳ. Traction permanent magnet synchronous motor torque control with flux weakening. *Radioengineering*, 18(4):601–605, 2009.

R. Elsayed Shaltout. *Multibody approach for railway dynamic analysis*. PhD thesis, Universitat Politécnica de Valéncia, 2013.

EN. 14363: 2005. *Railway applications-Testing for the acceptance of running characteristics of railway vehicles-Testing of running behavior and stationary tests*, pages 6–36, 2007.

EN. 13674-1. *Railway applications-Track & Railpart*, 2011.

EN. 1302/2014/EU. *Locomotives and passenger rolling stock - LOC & PAS TSI*, 1, 2014.

J. Evans and M. Berg. Challenges in simulation of rail vehicle dynamics. *Vehicle System Dynamics*, 47(8):1023–1048, 2009.

R. Faragher et al. Understanding the basis of the kalman filter via a simple and intuitive derivation. *IEEE Signal processing magazine*, 29(5):128–132, 2012.

B. Fornberg. Generation of finite difference formulas on arbitrarily spaced grids. *Mathematics of computation*, 51(184):699–706, 1988.

L. Freibauer. Adheze kola vozidla na dráze (in czech). In *Proc. of VII. vědecká konference VŠDS*, volume 3, 1983.

V. K. Garg and R. V. Dukkipati. *Dynamics of railway vehicle systems, 1984*. Academic Press, New York, 1984.

Gensys. Users manual for program kpf. www.gensys.se/doc_html/kpf.html, 2016. Retrieved: September 7, 2016.

J. Gerlici, T. Lack, et al. *Transport means properties analysis – Vol. I.* EDIS Publishing house of University of Zilina, 2005.

M. S. Grewal and A. P. Andrews. *Kalman filtering - Theory and Practice with MATLAB*. John Wiley & Sons, 2015.

A. J. Haug. *Bayesian Estimation and Tracking: A Practical Guide*. John Wiley & Sons, 2012.

H. Hertz. Über die berührung fester elastischer körper. *Journal für die reine und angewandte Mathematik*, 92:156–171, 1882.

P. Hubbard, C. Ward, R. Goodall, and R. Dixon. Real time detection of low adhesion in the wheel/rail contact. *Proceedings of the Institution of Mechanical Engineers, Part F: Journal of Rail and Rapid Transit*, 227(6):623–634, 2013. doi: 10.1177/0954409713503634.

P. Hubbard, C. Ward, R. Dixon, and R. Goodall. Models for estimation of creep forces in the wheel/rail contact under varying adhesion levels. *Vehicle System Dynamics*, 52 (sup1):370–386, 2014.

I. Hussain, T. Mei, and R. Ritchings. Estimation of wheel–rail contact conditions and adhesion using the multiple model approach. *Vehicle System Dynamics*, 51(1):32–53, 2013.

S. Iwnicki. Manchester benchmarks for rail vehicle simulation. *Vehicle System Dynamics*, 30(3-4):295–313, 1998.

S. Iwnicki. *Handbook of railway vehicle dynamics*. CRC press, 2006.

A. Jaschinski and H. Netter. Non-linear dynamical investigations by using simplified wheelset models. *Vehicle System Dynamics*, 20(sup1):284–298, 1992.

A. Jaschinski, H. Chollet, S. Iwnicki, A. Wickens, and J. Würzen. The application of roller rigs to railway vehicle dynamics. *Vehicle System Dynamics*, 31(5-6):345–392, 1999.

K. Johnson. The effect of spin upon the rolling motion of an elastic sphere on a plane. *Journal of Applied Mechanics*, 25(3):332–338, 1958.

K. L. Johnson. *Contact mechanics*. Cambridge university press, 1985.

S. J. Julier and J. K. Uhlmann. Unscented filtering and nonlinear estimation. *Proceedings of the IEEE*, 92(3):401–422, 2004.

S. J. Julier, J. K. Uhlmann, and H. F. Durrant-Whyte. A new approach for filtering nonlinear systems. In *American Control Conference, Proceedings of the 1995*, volume 3, pages 1628–1632. IEEE, 1995.

J. Kalker. Simplified theory of rolling contact. *Delft Progress Rep.*, 1(1):1–10, 1973.

J. Kalker. Survey of wheel–rail rolling contact theory. *Vehicle System Dynamics*, 8(4): 317–358, 1979.

J. Kalker. A fast algorithm for the simplified theory of rolling contact. *Vehicle system dynamics*, 11(1):1–13, 1982.

J. Kalker. Wheel-rail rolling contact theory. *Wear*, 144(1-2):243–261, 1991.

J. J. Kalker. *On the rolling contact of two elastic bodies in the presence of dry friction*. PhD thesis, TU Delft, Delft University of Technology, 1967.

J. J. Kalker. *Three-dimensional elastic bodies in rolling contact*. Springer Science & Business Media, 1990. ISBN 978-90-481-4066-4.

R. E. Kalman. A new approach to linear filtering and prediction problems. *Journal of Fluids Engineering*, 82(1):35–45, 1960.

R. Kandepu, B. Foss, and L. Imsland. Applying the unscented kalman filter for nonlinear state estimation. *Journal of Process Control*, 18(7):753–768, 2008.

T. Karis. Track irregularities for high-speed trains. *Master of Science Thesis, Stockholm, Sweden*, 2009.

J. Kawasaki and K. Youcef-Toumi. Estimation of rail irregularities. In *American Control Conference, 2002. Proceedings of the 2002*, volume 5, pages 3650–3660. IEEE, 2002.

K. Knothe. History of wheel/rail contact mechanics: from redtenbacher to kalker. *Vehicle System Dynamics*, 46(1-2):9–26, 2008.

K. Knothe and F. Böhm. History of stability of railway and road vehicles. *Vehicle System Dynamics*, 31(5-6):283–323, 1999.

K. Knothe, R. Wille, and B. W. Zastrau. Advanced contact mechanics–road and rail. *Vehicle System Dynamics*, 35(4-5):361–407, 2001.

C. Knudsen, E. Slivsgaard, M. Rose, H. True, and R. Feldberg. Dynamics of a model of a railway wheelset. *Nonlinear Dynamics*, 6(2):215–236, 1994.

Z. Li. *Wheel-rail rolling contact and its application to wear simulation*. PhD thesis, TU Delft, Delft University of Technology, 2002.

B. Liu and S. Bruni. Analysis of wheel-roller contact and comparison with the wheel-rail case. *Urban Rail Transit*, 1(4):215–226, 2015.

M. Liu. A nonlinear dynamic model for single-axle wheelsets with profiled wheels and rails. In *Proceedings of the International Conference of Control, Dynamic Systems, and Robotics*, number 60, Ottawa, Ontario, Canada, May 15–16 2014.

B. Matzuka, M. Aoi, A. Attarian, and H. Tran. Nonlinear filtering methodologies for parameter estimation. *Department of Mathematics, North Carolina State University*, 1, 2012.

S. Meymand and M. Ahmadian. Design, development, and calibration of a force-moment measurement system for wheel–rail contact mechanics in roller rigs. *Measurement*, 81: 113–122, 2016.

S. Z. Meymand. *State of the Art Roller Rig for Precise Evaluation of Wheel-Rail Contact Mechanics and Dynamics*. PhD thesis, Virginia Tech, 2016.

MEZ. Trojfázové asynchronní motory nakrátko. http://www.elmotory.cz/download/K_08.pdf, 2016. Retrieved: November 22, 2016.

T. Michálek. Namáhání v kontaktní ploše mezi kolem a kolejnicí [loading in the contact area of wheel and rail]. Student Work, 2008. University of Pardubice.

T. Michálek and J. Zelenka. Reduction of lateral forces between the railway vehicle and the track in small-radius curves by means of active elements. *Applied and Computational Mechanics*, 5(2), 2011.

Y. Nath, K. Athre, and K. Jayadev. Non–linear dynamics of railway wheelset. In *National Conference on Nonlinear Systems & Dynamics, NC NSD-2003*, pages 233–236, Indian Institute of Technology, Kharagpur 721302, December 28-30 2003.

H. Netter, G. Schupp, W. Rulka, and K. Schroeder. New aspects of contact modelling and validation within multibody system simulation of railway vehicles. *Vehicle System Dynamics*, 29(S1):246–269, 1998.

J. Piotrowski and H. Chollet. Wheel–rail contact models for vehicle system dynamics including multi-point contact. *Vehicle System Dynamics*, 43(6-7):455–483, 2005.

J. Piotrowski and W. Kik. A simplified model of wheel/rail contact mechanics for non-hertzian problems and its application in rail vehicle dynamic simulations. *Vehicle System Dynamics*, 46(1-2):27–48, 2008.

O. Polach. A fast wheel-rail forces calculation computer code. *Vehicle System Dynamics*, 33:728–739, 2000.

O. Polach. Creep forces in simulations of traction vehicles running on adhesion limit. *Wear*, 258(7):992–1000, 2005.

O. Polach. Comparability of the non-linear and linearized stability assessment during railway vehicle design. *Vehicle System Dynamics*, 44(sup1):129–138, 2006.

O. Polach. Characteristic parameters of nonlinear wheel/rail contact geometry. *Vehicle System Dynamics*, 48(S1):19–36, 2010.

J. Pombo, J. Ambrósio, and M. Silva. A new wheel–rail contact model for railway dynamics. *Vehicle System Dynamics*, 45(2):165–189, 2007.

F. d. C. Santos, A. dos Santos Jr, F. Bruni, and L. Santos. Evaluation of subsurface contact stresses in railroad wheels using an elastic half-space model. *Journal of the Brazilian Society of Mechanical Sciences and Engineering*, 26(4):420–429, 2004.

G. Schupp, C. Weidemann, and L. Mauer. Modelling the contact between wheel and rail within multibody system simulation. *Vehicle System Dynamics*, 41(5):349–364, 2004.

I. Sebeşan and Y. Zakaria. Determination of wheel-rail contact characteristics by creating a special program for calculation. *Mathematical Modelling in Civil Engineering*, 10(3): 48–59, 2014.

P. C. Sen. *Principles of electric machines and power electronics*. John Wiley & Sons, 2007.

A. A. Shabana, K. E. Zaazaa, and H. Sugiyama. *Railroad vehicle dynamics: a computational approach*. CRC press, 2007.

Z. Shen, J. Hedrick, and J. Elkins. A comparison of alternative creep force models for rail vehicle dynamic analysis. *Vehicle System Dynamics*, 12(1-3):79–83, 1983.

I. Y. Shevtsov. *Wheel/rail interface optimisation*. PhD thesis, TU Delft, Delft University of Technology, 2008.

M. S. Sichani, R. Enblom, and M. Berg. Comparison of non-elliptic contact models: towards fast and accurate modelling of wheel–rail contact. *Wear*, 314(1):111–117, 2014.

D. Simon. *Optimal state estimation: Kalman, H infinity, and nonlinear approaches*. John Wiley & Sons, 2006.

M. Spiryagin, C. Cole, Y. Q. Sun, M. McClanachan, V. Spiryagin, and T. McSweeney. *Design and simulation of rail vehicles*. CRC Press, 2014.

J. P. Srivastava, P. Sarkar, and V. Ranjan. An approximate analysis for hertzian elliptical wheel-rail contact problem. In *IT Roorkee, India: National Conference on Machines and Mechanisms (iNaCoMM2013)*. IIT Roorkee, India: National Conference on Machines and Mechanisms (iNaCoMM2013), 2013.

UIC. 510-2. *Trailing stock: wheels and wheelsets. Conditions concern*, 2004.

UM. Simulation of kinematics and dynamics of planar and spatial mechanical systems. www.universalmechanism.com/en/, 2016. Retrieved: November 30, 2016.

R. Van Der Merwe. *Sigma-point Kalman filters for probabilistic inference in dynamic state-space models*. PhD thesis, Oregon Health & Science University, 2004.

A. R. Vatankhah. Approximate solutions to complete elliptic integrals for practical use in water engineering. *Journal of Hydrologic Engineering*, 16(11):942–945, 2011.

P. Vermeulen and K. Johnson. Contact of nonspherical elastic bodies transmitting tangential forces. *Journal of Applied Mechanics*, 31(2):338–340, 1964.

E. Vollebregt and P. Wilders. Fastsim2: a second-order accurate frictional rolling contact algorithm. *Computational Mechanics*, 47(1):105–116, 2011.

E. Vollebregt, C. Weidemann, and A. Kienberger. Use of "contact" in multi-body vehicle dynamics and profile wear simulation: Initial results. In *Proceedings of the 22nd International Symposium on Dynamics of Vehicles on Roads and Tracks*, 2011.

P. Voltr. Simulation of wheel–rail contact conditions on experimental equipment. *Railway Transport and Logistics*, XI:77–82, 2015.

P. Voltr and M. Lata. Transient wheel–rail adhesion characteristics under the cleaning effect of sliding. *Vehicle System Dynamics*, 53(5):605–618, 2015.

P. Voltr, J. Čáp, and M. Lata. New practical results about adhesion limites obtained from experimental stand testing. *Scientific papers of the University of Pardubice. Series B, Jan Perner Transport Faculty. 15 (2009)*, 2009.

P. Voltr, M. Lata, and O. Černỳ. Measuring of wheel–rail adhesion characteristics at a test stand. *Engineering Mechanics*, page 181, 2012.

E. Wan and R. Van Der Merwe. Chapter 7: The unscented kalman filter. *Kalman Filtering and Neural Networks*, pages 221–280, 2001.

W. Wang, H. Zhang, H. Wang, Q. Liu, and M. Zhu. Study on the adhesion behavior of wheel/rail under oil, water and sanding conditions. *Wear*, 271(9):2693–2698, 2011.

C. P. Ward, P. Weston, E. Stewart, H. Li, R. M. Goodall, C. Roberts, T. Mei, G. Charles, and R. Dixon. Condition monitoring opportunities using vehicle-based sensors. *Proceedings of the Institution of Mechanical Engineers, Part F: Journal of Rail and Rapid Transit*, 225(2):202–218, 2011.

C. P. Ward, R. M. Goodall, R. Dixon, and G. Charles. Adhesion estimation at the wheel–rail interface using advanced model-based filtering. *Vehicle System Dynamics*, 50(12):1797–1816, 2012.

A. Wickens. *Fundamentals of rail vehicle dynamics*. CRC Press, 2005.

B. Xu, J. Zhang, and X. Guan. Estimation of the parameters of a railway vehicle suspension using model-based filters with uncertainties. *Proceedings of the Institution of Mechanical Engineers, Part F: Journal of Rail and Rapid Transit*, 229(7):785–797, 2015.

G. Yang. *Dynamic analysis of railway wheelsets and complete vehicle systems*. PhD thesis, TU Delft, Delft University of Technology, 1993.

M. Zheng, K. Ikeda, and T. Shimomura. Estimation of continuous-time nonlinear systems by using the unscented kalman filter. In *SICE Annual Conference 2010, Proceedings of*, pages 2192–2195. IEEE, 2010.

Z. Zhongshun, X. Bowen, M. Lei, and G. Shaoyang. Parameter estimation of a railway vehicle running bogie using extended kalman filter. In *Control Conference (CCC), 2014 33rd Chinese*, pages 3393–3398. IEEE, 2014.

Publications of the PhD Student

O. Kılınç and A. Onat. Simple test procedure of strain gage measurement: An introductory implementation towards railway vehicle testing. In *1st International Workshop on Construction and Electricity Applications on Vocational Education*, pages 395–407, 30 November–1 December 2015. ISBN 975-06-1861-1.

A. Onat, P. Voltr, and M. Lata. Nonlinear wheel/rail contact geometry characteristics & determination of hertzian contact. *Scientific papers of the University of Pardubice (Series B)*, 19:145–152, 2014. ISBN: 978-80-7395-902-9.

A. Onat, P. Voltr, and M. Lata. Analysis of lateral dynamical response of a wheelset during traction. In *22nd International Conference "Current Problems in Rail Vehicles - PRORAIL"*, volume 2, pages 75–84, September 16–18 2015. ISBN: 978-80-89276-49-3.

A. Onat, O. Kılınç, and M. Lata. A linear kalman filtering scheme for estimation of secondary vertical suspension of railway vehicles. In *21st International Conference on VIBROENGINEERING*, volume 7, pages 124–128. Vibroengineering PROCEDIA, 31 August–1 September 2016a. ISSN 2345-0533.

A. Onat, P. Voltr, and M. Lata. A new friction condition identification approach for wheel–rail interface. *International Journal of Rail Transportation*, pages 1–18, 2016b. doi: 10.1080/23248378.2016.1253511. Taylor & Francis.

A. Onat, P. Voltr, and M. Lata. Estimation of primary suspension parameters from lateral dynamic response of a wheelset. In *22nd International Conference ENGINEERING MECHANICS*, pages 434–437, May 9–12 2016c. ISBN: 978-80-87012-59-8.

A. Onat, P. Voltr, and M. Lata. An unscented kalman filter based estimation scheme for a tram wheel test stand. -, 2017. (Under Preparation).